Visible and Ultraviolet Light Side-Emitting Optical Fibers Enable Water Purification

by

Mariana Lanzarini-Lopes

A Dissertation Presented in Partial Fulfillment
of the Requirements for the Degree
Doctor of Philosophy

Approved February 2020 by the
Graduate Supervisory Committee:

Paul Westerhoff, Chair
Pedro Alvarez
Sergi Garcia-Segura

ARIZONA STATE UNIVERSITY

May 2020

ABSTRACT

Light driven reactions can replace chemical and material consumption of advanced water treatment technologies. A barrier to light-driven water treatment is optical obstructions in aquafers (i.e. granular media) or built infrastructures (i.e. tubing) that limits light propagation from a single source such as the sun, or lamps. Side emitting optical fibers (SEOFs) can increase light distribution by > 1000 X from one-point source, but absorbance of UV light by conventional optical fibers limit their application to visible light only.

This dissertation assessed how SEOFs can enable visible through ultraviolet light driven processes to purify water. I first used an existing visible light polymer SEOF and phototrophic organisms to increase the dissolved oxygen level of a granular sand reactor to > 15 mg DO/L. The results indicated that SEOFs successfully guide light past optical obstructions for environmental remediation which encouraged the fabrication of UV-C SEOFs for microbial inactivation.

I was the first to obtain consecutive UV-C side emission from optical fibers by placing nanoparticles on the surface of a UV transmitting glass core. The nanoparticles induced side-emission via Mie scattering and interactions with the evanescent wave. The side emission intensity was modulated by tuning the separation distance between the nanoparticle and fiber surface. Coating the fiber with a UV-C transparent polymer offered the optical fiber flexibility and prevented nanoparticle release into solution. One SEOF coupled to a 265 nm LED achieved 3-log inactivation of *E. coli*. Finally, a method was developed to quantify the zone of inhibition obtained by a low flux output source. By placing a SEOF connected to a UV-C LED over a nutrient rich LB agar plate, I illustrated that one SEOF inhibited the growth of *P. aeruginosa* and *E. coli* within 2.8 cm along the fiber’s length. Ultimately this research informed that side emitting optical fibers can enable light driven water purification by guiding and distributing specific wavelengths of light directly to the microbial communities of interest.

ACKNOWLEDGEMENTS

I first want to acknowledge and thank my committee members. Paul Westerhoff's creativity and honest curiosity continue to inspire me to take on challenging and impactful research. I am extremely thankful for all the opportunities (i.e. NEWT, internships, international conferences, collaborations ect.) he provides us, allowing us to develop a wide range of skills and networks during our PhDs. I sincerely appreciate Pedro Alvarez for successfully leading NEWT while making time for and valuing our work as graduate students. Finally, Sergi Garcia-Segura served as a mentor since his first day working at Arizona State University. I have learned a great deal from him from laboratory technique to writing skills. His patience and dedication to my development as a researcher will always be remembered. I also want to recognize and acknowledge the optical fiber team at Lawrence Livermore National Laboratories, specially Michael Messerly and AJ Simons. They were the foundation for my interest and knowledge of optical fibers. Through their guidance, trust and support I began to develop the UV-C side emitting optical fiber presented in this work.

The research herein could not have been completed without my funding sources including: NSF Interdisciplinary Graduate Education and Research Traineeship, the NSF Nanotechnology enabled water treatment center, Arizona State University Ira A. Fulton School of Engineering Dean's Fellowship, Academic Rewards for College Scientists, and American Water Works Association CDM smith scholarship. A special thanks to the NSF IGERT program and NSF NEWT, who also provided training in leadership, diversity, business and policy.

My lab mates and classmates supported me through this phase and helped to develop integral skills. Thank you for creating an inclusive, enjoyable and productive work environment. An additional thanks to all who mentored me through my graduate degree and before coming to Arizona. A special thanks to those I have mentored: Brandon Cruz, Zhe Zhao, Michelle Landreville and Jose Carlos Ortiz Beltranena. Their interest and dedication along with academic growth has been the most rewarding part of my graduate experience. Mentoring and guiding them through research has inspired me to pursue an academic career.

I want to thank my ultimate frisbee community, including my numerous roommates, teammates and friends. The relationships I formed through this sport contributed significantly to my sanity in the past five years. I have spent most of my free time in their presence. They have been both an outlet and a support, and it is because of these friendships that I have fallen in love with the state of Arizona.

I would especially like to say thank you to my parents, who have instilled in me the intellectual curiosity and sense of adventure that allowed me to not only succeed but truly enjoy the past five years. Thank you also to my impressive siblings, Gabriela, Ligia, Jose, and Joao who inspire me to make the world a better place. Finally, I wish to show my deepest gratitude to my partner and fiancé, Michael Ising for his encouragement and patience. He has been with me through this entire adventure, continuously pushing me to be the best engineer, scientist and person I can be.

TABLE OF CONTENTS

LIST OF TABLES

LIST OF FIGURES

Figure Page

Figure Page

Figure Page

CHAPTER 1

INTRODUCTION

Assuring access to clean water continues to be a leading challenge around the world. The lack of appropriate disinfection results in an estimated 502,000 diarrheal deaths each year (“Drinking-Water,” 2018). Use of chlorine has eradicated fecal contaminations in the United States, but opportunistic pathogens in piping biofilms leads to 7,500 reported cases of Legionnaires disease each year (Garner et al., 2018; Jemba et al., 2014). Additionally, anthropological activities continue to increase groundwater contamination of organic and synthetic compounds. There is a need to remediate groundwater pollution and provide microbial protection without production of by-products. Exploiting light to drive reactions can avoid the adverse environmental impacts associated with chemical addition.

Electromagnetic spectra from UV through visible light provides opportunities to enhance water treatment. Figure 1-1 illustrates water purification processes enabled by wavelengths in the UV-C to visible light spectrum. Visible light can support phototrophic oxygen production to enhance biological remediation (Jørgensen et al., 1979). Visible and ultraviolet-AB (UV-AB) light enables photocatalytic oxidation or reduction reactions (Tugaoen et al., 2018). Germicidal ultraviolet-C (UV-C) light ($250 \text{ nm} < \lambda < 280 \text{ nm}$) damages the DNA and protein of microorganism, preventing further replication and infection (Chatterley & Linden, 2010; Beck et al., 2017). Light in the visible through UV-C wavelengths are produced both naturally by the sun and by artificial lamp sources. The challenge is distributing this light through large volumes and unique geometries.

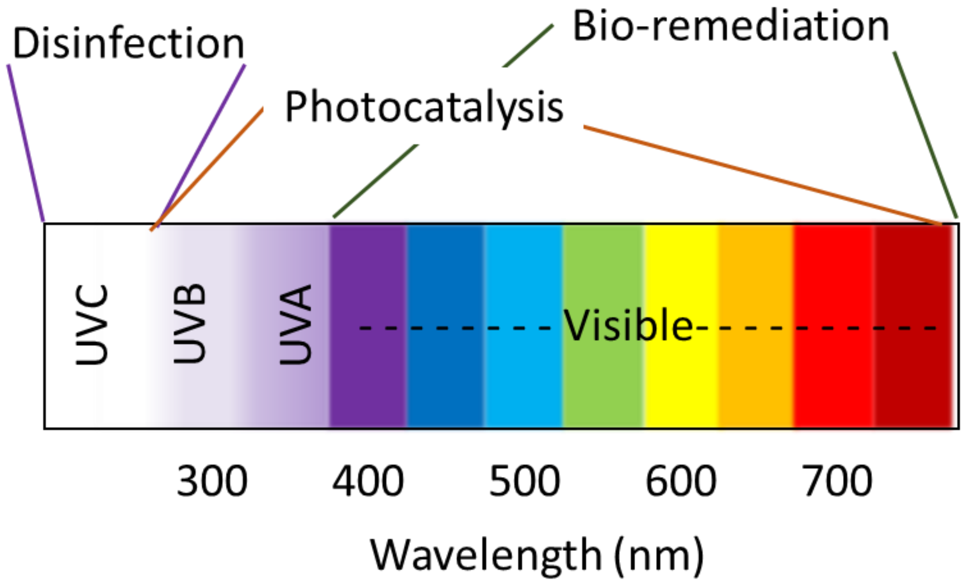

Figure 1-1 Schematic of UV and visible light spectrum and opportunities for light driven water treatment.

Solar radiation is a widely available “free” source of light ranging from UV-C to visible light. However, there are barriers to using sunlight for water purification. The available UV-C light is mostly absorbed by ozone within the earth’s atmosphere. The remaining visible to UV-AB light is diffuse and does not penetrate soil beyond ~10 mm (Tester & Morris, 1987). Applications of sunlight to groundwater remediation would require the concentration of sunlight by parabolic mirrors and guidance of that light below the soil.

Technological advancements of light emitting diodes (LEDs) has exponentially increased the opportunity for light driven water treatment due to its compact nature, tunability of wavelength and intensity, and global availability (Autin et al., 2013; Beck et al., 2017; Chen et al., 2017; Matafonova & Batoev, 2018). Furthermore, there is rising global pressure to replace mercury-based UV lights (Linden et al., 2019). A crucial technology barrier of LEDs is their small surface area of irradiation (< 1 cm^2). Creating arrays of LEDs can increase the surface area for water treatment reactors but is costly due to added cooling loads (Chen et al., 2017; Martín-Sómer et al., 2017; Oguma et al., 2013; Song et al., 2016). Additionally, there are certain geometries where the use of any existing light sources will be ineffective. The optical obstructions in aquafers (i.e. granular media) or built infrastructures (i.e. tubing) limit light propagation from a single point source. A need exists for a means to distribute light across large volumes within these untraditional spaces.

Optical fibers can be used to increase light distribution from one LED for the purpose of water purification. Optical fibers are long, thin and flexible glass and polymeric tubes used to transport light axially for the purpose of telecommunication in long range transmission. They contain (i) a light guiding core, surrounded by (ii) a lower index of refraction cladding to allow for complete internal reflection. In order to optimize light distribution in water treatment, light must be scattered away from the core, along the length of the optical fiber simulating a glow. These flexible optical fibers can follow the bends of the reactor; therefore, the photon path is not limited by its geometry. This concept can significantly increase the surface area and distance of irradiation from one light source.

This dissertation develops and applies side emitting optical fibers (SEOF) technology to enable photo-assisted water treatment from visible to UV-C wavelengths of light. Benefits of this work includes improved delivery of (i) visible light for bioremediation and (ii) UV-C for disinfection and biofilm prevention. The knowledge obtained through this work can be translated to photocatalytic reactions, optics and biofilm prevention in medical equipament.

Dissertation Organization

This dissertation is organized into chapters that are guided by research questions to answer the overarching research question: **How can side emitting optical fibers enable visible through ultraviolet light driven processes to purify water?** Chapter 2 introduces optical fibers, existing side emitting applications, and light assisted water treatment processes. The body of the dissertation (Chapters 3-6) address the five research questions (RQ) listed in Table 1-1 that guided this work.

Table 1-1 Dissertation research questions and organization

Chapter	Research Question
3	1. What levels of dissolved oxygen can side emitting optical fibers enable in subsurface environments?
4	2. How can cladding modification increase side emission of UV light from silica core optical fibers? 3. Which material properties of optical fibers prevent side emission of UV-C light?
5	4. How can UV-C side emission from optical fibers be achieved to disinfect water?
6	5. What is the effectiveness of UV-C SEOF in preventing microbial surface growth?

Chapters 3, 4, and 5 have been published in peer-reviewed journals and Chapter 6 has been submitted for review. Chapter 7 synthesizes the research chapters and outlines approaches for large scale fabrication and implementation of UV-C side emitting optical fibers for environmental remediation.

CHAPTER 2

BACKGROUND

The aim of this dissertation is to enhance distribution of visible to ultraviolet wavelengths of light for water treatment by use of side emitting optical fibers (SEOF). Light can be used for water treatment processes including bioremediation, photocatalysis and disinfection. This chapter introduces the mechanism involving light in these treatment processes and how ineffective light distribution has limited their progress into conventional water treatment. Additionally, the structure and history of both end-emitting and side emitting optical fibers are reviewed. Finally, barriers are identified for (i) light assisted water treatment and (ii) the development of side emitting optical fibers (SEOF).

Light in biological remediation

Visible light drives phototrophic processes that enable chemotrophic aerobic bioremediation (Chandra & Sobti, 2019). The energy from visible light wavelengths enable plants, algae and cyanobacteria to synthesize organic substrates from inorganic carbon and water:

$$6CO_2 + 6H_2O + Light\ energy \rightarrow C_6H_{12}O_6 + 6O_2 \qquad \text{Eq. 2.1}$$

The products of this reaction is new biomass and the oxygen. Heterotrophic organisms then metabolize organic carbon sources and oxygen to produce energy suitable to enable biodegradation of environmental pollutants:

$$C_6H_{12}O_6 + 6O_2 \rightarrow 6CO_2 + 6H_2O + ATP \qquad \text{Eq. 2.2}$$

Environmental engineers take advantage of these natural process for both decreased greenhouse effect (i.e. carbon sequestration) or bioremediation. In biological waste treatment, phototrophs and chemotrophs convert organic carbons (i.e. sludge/waste) to carbon dioxide or co-substrates.

Microalgae and chemotrophic bacteria are used for a range of applications, including nitrogen fixation and breaking down of both pharmaceutical compounds and solid wastes (El-Bestawy et a., 2007; McEvoy et al., 2004).They have been studied in the catabolism of dyes, pesticides, insecticides and crude oil (Cerniglia et al., 1981) for active wastewater treatment and passive treatment of contaminated soils (Borde et al., 2003). Plantar algae have been used in tertiary wastewater treatment and filamentous cyanobacteria have been recommended for both secondary and tertiary treatment (Pinto et al., 2002; Valderrama et al., 2002). These micro bacterium are extremely beneficial as pollution control agents in wildtype, mutant and genetically engineered forms for economic and low maintenance technologies (El-Bestawy et al., 2007).

Oxygen is essential in heterotrophic remediation. However, oxygen is limited in aquafers where phototrophic activity cannot be sustained by sunlight. Current mechanical and chemical aeration techniques include air sparging, liquid oxygen injection, and hydrogen peroxide injection, which all demand high energy inputs (Chapelle, 1999; Austin et al., 2003). Contaminated groundwater sites can require decades of remedial activity and may not be located near the power grids (i.e., developing countries or remote locations). Enabling visible light (i.e. sun or artificial) to be delivered and distributed through subsurface aquafers can significantly decrease capital and operational costs of biological remediation. There is a need to develop sustainable long-term technologies to deliver light into the subsurface to aid in groundwater remediation.

Light in photocatalytic water treatment

Both visible and UV-AB wavelengths are used to drive photocatalytic reactions for water treatment. Photocatalysis is the acceleration of chemical reactions by light. In this process, light excites the electrons of a semiconductor past its bandgap forming an exited high- energy state (Eq. 2.3). An electron is then trapped in the conductive (e_{CB^-}) band and a hole in the valance band (h_{VB^+}). Figure 2-1 illustrates these mechanisms with TIO_2 as the photocatalyst.

$$Photocatalyst + hv \rightarrow\ h_{VB^+} +\ e_{CB^-} \qquad \text{Eq. 2.3}$$

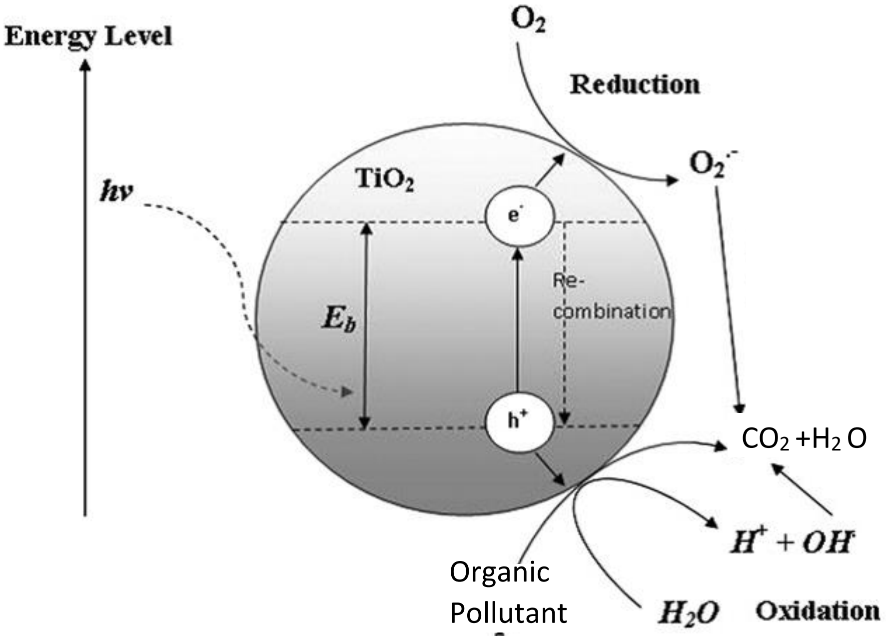

Figure 2-1 Mechanism of photocatalytic degradation of contaminants for water treatment. This figure was adapted from Chong et al. 2010(Chong, Jin, Chow, & Saint, 2010).

Charge separation results in an oxidizing and reducing potential both of which can be used for contaminant degradation in water (Umar & Abdul, 2013). h_{VB^+} oxidizes organic compounds by (i) direct charge transfer with the compound (Eq. 2.4) or (ii) reacting with water to generate hydroxyl radicals ($^{\bullet}$OH) (Eq. 2.5). Hydroxyl radicals non selectively oxidize any electron rich organic molecule into CO_2 and water (Górska et al., 2008) (Eq. 2.6). Hydroxyl radical generation is often the leading mechanisms of oxidation due to its high oxidation potential (2.80 eV) and higher occurrence of water molecules when compared to the contaminant.

$$Organic\ Compound + h_{VB^+} \rightarrow CO_2 + Water \qquad \text{Eq. 2.4}$$

$$Water + h_{VB^+} \rightarrow H^+ + {}^{\bullet}\mathrm{OH} \qquad \text{Eq. 2.5}$$

$$Organic\ Compound + {}^{\bullet}\mathrm{OH} \rightarrow CO_2 + Water \qquad \text{Eq. 2.6}$$

The conductive band, e_{CB^-}, can also lead to oxidation of organic compounds. Here, oxygen reacts with the high energy electron forming an anion superoxide ($O_2^{\bullet -}$) (Eq. 2.7). A superoxide is then formed that either directly reacts with the organic contaminant or leads to the formation of $^{\bullet}$OH.

$$O_2 + e_{CB^-} \rightarrow O_2^{\bullet -} \qquad \text{Eq. 2.7}$$

Lastly, photocatalytic reductive reactions can also be exploited in water treatment. For example, photocatalytic nitrate reduction is one of the only technologies capable of yielding N_2 as a preferred by-product (O’Neal et al., 2017). Reduction reactions will occur because of direct charge transfer from the e_{CB^-} to the reactant. Because e_{CB^-} and h_{VB^+} are highly reductive and oxidizing species, both species must be engaged in redox processes. This means a hole scavenger (i.e. oxalic acid, formic acid, methanol) must be present.

The promise of photocatalysis as a chemical free method of contaminant degradation led to rapid development in the field of advance oxidation processes (AOPs). The most promising and researched photocatalyst is titanium dioxide (TiO_2). This material absorbs photons with energy higher than 3.2 eV (wavelength< 390 nm). Doping TiO_2 with other materials (Nitrogen, Silver) can decrease the band gap enabling visible light photocatalysis (Górska et al., 2008). These works have been extensively studied, however photo-physical and photo-chemical inefficiencies limit these processes. Both slurry and fixed bed photocatalytic reactors are limited in geometry because of short optical pathways and low contaminant interaction respectively. Additionally, electron hole pair recombination's results in low quantum yields of reaction. Ling et al. 2017 placed photocatalysts on an optical fiber to directly deliver light to the material throughout the volume of the rector. This concept maximized both light and contaminant interaction with the photocatalyst and is furthered discussed in section 2.4.

Light for microbial inactivation

When bacteria is directly exposed to ultraviolet radiation below 280 nm the DNA and proteins are damaged, preventing cell replication and therefore possible infection. Figure 2-2 shows the spectral absorbance of both DNA and protein molecules. DNA strongly absorbs UV-C light between 200 and 280 nm with a relative peak at 260, while protein molecules have a peak absorbance at 280 nm. The absorbed light is indicative of molecular vibrations and cleavages at those wavelengths.

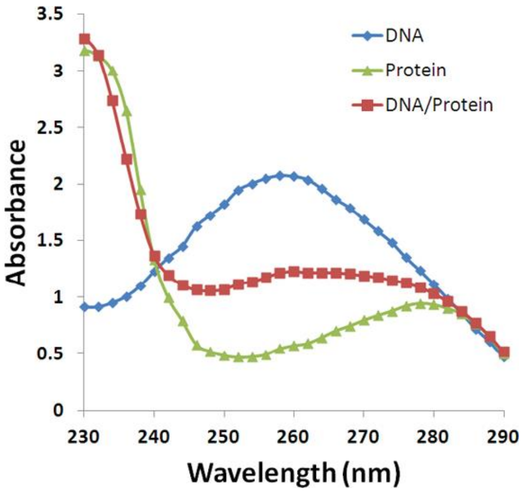

Figure 2-2 Spectral absorbance of DNA and proteins. Figure was adapted form Brescia 2002 (Brescia, 2012).

Photons absorbed by the DNA causes two consecutive bases on one nucleotide chain to bind together, destroying the normal base-pairing double strand structure. Figure 2-3 illustrates the localized transformation in DNA. Two types of lesion forms between nucleobases. A quarter (25%) of UV induced lesions are 6-4 photoproducts (Sinha & Häder, 2002). These are characterized by the interaction of one carbon on each base. The remainder majority (75%) are cyclobutene pyridine dimers (CPDs). CPDs are four membered ring structures formed between the C5 and C6 atom on each pyrimidine base (Douki, 2013; Eischeid & Linden, 2007; Rastogi et al., 2010). These lesions inhibit cellular processes such as transcription and replication (Moné et al., 2001; Rodríguez, Bounty, & Linden, 2013; Sinha & Häder, 2002). Uncorrected lesions (i.e. photoreactivation and excision repair) are the primary cause of melanomas in humans. However, the same concept is used as a germicide in water treatment to inhibit growth of pathogenic microorganisms from infecting people (Poepping et al., 2014).

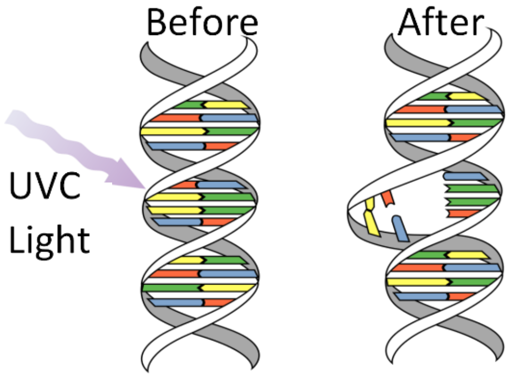

Figure 2-3 Schematic of DNA lesion and same strand recombination after UV exposure. This figure was adapted from an illustration in Wikipedia (Mouagip).

Ultraviolet light also causes damage to the functional structure of viral proteins that are responsible for the rebuilding previously damaged DNA. Because Protein damage occurs with 280 nm wavelengths, broadband lamps can increase the effectiveness of disinfection reactors. For example, adenovirus is up to four times more sensitive to medium pressure, polychromatic mercury lamps, than low pressure monochromatic mercury lamps (Beck et al., 2018; Linden et al., 2009).

The sensitivity of microorganisms is reported in dose (mj/cm^2) per logarithmic decay. Sensitivities between organisms vary significantly. The outer structure and repair mechanisms of organisms enable variable protection to UV damage. For example, the highest UV dose reported for 4 log inactivation of a bacteria is 30 mj/cm^2. However, virus and bacterial spore have reported 4-log UV dose of > 200 mj/cm^2 and > 500 mj/cm^2 respectively (Chevrefils et al., 2006).

Significant variances are reported UV dose values for the same organisms cause by both the physiological state of the microorganism and the fluence assessment.

Physiological state of an organism results from growth patterns and stored environment and can significantly vary replication and survival rates. Additionally, fluence distribution and hydraulic profile of experimental reactor effects the light transfer efficiency from the lamp to the organisms of interest. Chevrefils et al. compiled the doses reported for 1- 6 log inactivation of various bacteria, protozoa, viruses and algae before 2006 (Chevrefils et al., 2006). The table was recently updated and expanded with values reported up to 2016. The 4-log inactivation of *E. coli, P. aeruginosa and L. pneumophilia* are included in table 2.1 along with the respective lamps used in the study. These include low pressure mercury lamp (LP), medium pressure mercury lamp (MP) and 265 nm light emitting diodes (LED). Only single lamp experiments are reported here.

Table 2-1 Dose (mj/cm^2) for 4 Log inactivation of *E. coli, P. aeruginosa and L. pneumophila*. All values are obtained from the updated table of Chevrefils et al. 2006(Chevrefils et al., 2006).

Organism identification	**Lamp type**	**Dose (mj/cm^2)**	**Reference**
Escherichia coli			
ATCC11229	LP	8.4	(Chang et al., 1985)
ATCC11229	LP	5.0	(Harris et al., 1987)
ATCC11229	LP	11.0	(Hoyer, 1998)
ATCC11229	LP	8.3	(Sommer et al., 1998)
ATCC11229	LP	6.5	(Sommer et al., 2000)
ATCC11229	LP	4.5	(Sommer et al., 2001)
ATCC11229	LP	8.2	(Zimmer & Slawson, 2002)
ATCC11229	LP	8.3	(Quek & Hu, 2008)
ATCC11229	LP	6.6	(Clauß et al., 2005)
ATCC11229	MP	5.3	(Quek & Hu, 2008)
ATCC 11303	LP	10.0	(Wu et al., 2005)
ATCC11775	LP	3.4	(Quek & Hu, 2008)
ATCC11775	MP	3.0	(Quek & Hu, 2008)
ATCC 15597	LP	12.0	(Quek & Hu, 2008)
ATCC 15597	MP	9.4	(Quek & Hu, 2008)
ATCC 25922	LP	8.0	(Sommer et al., 1998)
ATCC 29425	LED 265 nm	20.0	(Chatterley & Linden, 2010)

ATCC 700891	LP	13.0	(Quek & Hu, 2008)
ATCC 700891	MP	9.0	(Quek & Hu, 2008)
B	LP	6.0	(Shin et al., 2008)
B	MP	6.0	(Shin et al., 2008)
B ATTCC 13033	LP	6.5	(Sholtes et al., 2016)
B ATTCC 13033	LED 260 nm	6.5	(Sholtes et al., 2016)
C	LP	5.6	(Otaki et al., 2003)
CGMCC 1.3373	LP	13.0	(Guo et al., 2009)
CGMCC 1.3373	MP	13.0	(Guo et al., 2009)
K12	LP	7.0	(Qiu et al., 2004)
K12 IFO 3301	LP	4.2	(Otaki et al., 2003)
K12 IFO 3301	LP	8.0	(Rattanakul et al.,2014)
K12 IFO 3301	LED 265 nm	9.0	(Oguma et al., 2013)
K12 IFO 3301	LED 280 nm	14.0	(Oguma et al., 2013)
K12 IFO 3301	LED 285 nm	23.0	(Oguma et al., 2001)
NBIM 9481	LP	10.5	(Quek & Hu, 2008)
NBIM 9481	MP	8.6	(Quek & Hu, 2008)
NBIMB 10083	LP	6.6	(Quek & Hu, 2008)
NBIMB 10083	MP	6.0	(Quek & Hu, 2008)
OP50	LP	9.1	(Bichai et al., 2009)
O157:H7	LP	6.0	(Tosa & Hirata, 1999)
O157:H7	LP	4.0	(Yaun et al., 2003)
O157:H7 ATCC 43894	LP	5.5	(Wilson et al., 1992)
O157:H7 CCUG 29193	LP	7.0	(Sommer et al., 2000)
O157:H7 CCUG 29197	LP	5.0	(Sommer et al., 2000)
O157:H7 CCUG 29199	LP	1.1	(Sommer et al., 2000)
O25: K98: NM	LP	10.0	(Sommer et al., 2000)
O26	LP	12.8	(Tosa & Hirata, 1999)
O50:H7	LP	4.5	(Sommer et al., 2000)
O78: H11	LP	6.0	(Sommer et al., 2000)
145 Ampicilin resistant	LP	4.7	(Templeton et al., 2009)
018 Trimethoprim resistant	LP	4.9	(Templeton et al., 2009)
SMS-3-5	LP	7.6	(McKinney & Pruden, 2012)
wild type	LP	6.6	(Butler et al., 1987)
wild type	LP	8.1	(Sommer et al., 2000)
Legionella pneumophila			
Philadelphia 2	LP	3.7	(Antopol & Ellner, 1979)
ATTCC 33152	LP	6.4	(Oguma et al., 2004)
ATTCC 33152	LP	5.7	(Cervero-Aragó et al., 2014)
ATTCC 33152	MP	7.7	(Oguma et al., 2004)
ATTCC 33823	LP	5.8	(Cervero-Aragó et al., 2014)

ATCC 43660	LP	9.3	(B. R. Wilson et al., 1992)
Sero group 1	LP	5.4	(Cervero-Aragó et al., 2014)
Sero group 8	LP	6.1	(Cervero-Aragó et al., 2014)
Pseudomonas Aeruginosa			
ATCC 9027	LP	17.0	(Abshire & Dunton, 1981b)
ATCC 27853	LP	3.1	(Clauß, 2006)
1	LP	6.3	(McKinney & Pruden, 2012)
NCTC 10662	LP	5.0	(Blatchley et al., 2016)

Lower pressure mercury lamps where mostly used prior to 2016. Values for medium pressure lamps and LEDs where reported as early as 2004 and 2010 respectively. There is a high variation in 4-log inactivation dose reported by every lamp source. *E. coli, P. aeruginosa* and *L. pneumophila* have overlapping ranges at 1.1 – 23 mj/cm^2, 3.7 – 9.3 mj/cm^2 and 3.1 – 17 mj/cm^2 respectively. These values indicate the organisms have similar sensitivity to UV light. Additionally, the highest *E. coli* dose was reported for a 285 nm wavelength LED, which in not considered DNA absorbing.

An increased occurrence of pathogenic infections by *P. aeruginosa* and *L. Pneumophila* increased publications of UV inactivation of these organisms. Rattanakul et al. 2018 reported 6.0 mj/cm^2 for *E. coli* and *P. aeruginosa* and 4.5 mj/cm^2 for *L. pneumophila* when using UV LED 265 nm (Rattanakul & Oguma, 2018). These value fall within the rage reported in Table 2.1 but illustrate that *L. pneumophila* may be slightly more sensitive to UV then previously reported.

It is difficult to make conclusions on the comparative sensitivity of organisms in different studies because of the variation in optical set ups. It is important for studies to report essential data such as UV transmissivity (UVT), spectrophotoradiometer calibration, and chemical actinometry procedure for measuring dose response.

Corrections for water absorbance and reflectivity can change UV dose values by 4-fold. Finally, using a standard set of guidelines and procedures (i.e. columnated beam apparatus, distance of lamp to sample) enables different studies to be compared more accurately.

Integrating UV-C disinfection in water treatment.

Water treatment using UV-C disinfection ranges from industrial to point of use applications. Water treatment plants use primarily polychromatic medium pressure mercury lamps. Multiple quartz tubes are installed in pipes or basins to disinfect water with less than one minute of contact time. Instalments often happen after an upgrade or as a result of stricter inactivation requirements of *Cryptosporidium parvum* and other microbial pathogens. The benefit to installing germicidal lamps over adding more halogens (chlorine) to water is that (unlike chlorine) UV does not form disinfection by-products such as trihalomethanes and haloacetic acids. However, UV also does not produce a disinfection residual, and treatment plants must still add a sequence of disinfectants after primary UV disinfection (Dotson et al., 2012).

Light emitting diodes (LEDs) are becoming a competitive and lower cost alternative with promising characteristics for water treatment including lack of warm up time, tunable radiation, no degradation from on/off cycles and longer life of use (Autin et al., 2013a; Beck et al., 2017; Chen et al., 2017a; Matafonova et al., 2018). The small footprint of UV LEDs allows engineers to explore new designs for single customer UV disinfection. These LEDs can be place in sinks, storage units, water bottles and point of use water treatment. Point of use applications are already commercially available and can serve remote communities since they are commercially available around the world (Chatterley & Linden, 2010; Lui et al., 2016).

UV LEDs are also gaining traction in disinfection of shower heads and distribution systems. Ezra and Torkzadeh (2020) considers a showerhead design with LEDs to prevent opportunistic respirator pathogens from infecting immunocompromised individuals. These LEDs would serve as a last barrier, inactivating microbial pathogens that come lose form pipes during distribution of treated water. Linden et al. (2019) proposed a model for secondary disinfection by installing UV LEDs throughout the entire water distribution system. Ultraviolet radiation can serve as the "residual disinfectant" instead of chlorine. This vision would prevent (i) operational problems and (ii) health hazards associated with the growth of pathogenic organisms in piping. Additionally, the flux output required by each LED would be minimal due to "infinite" contact time. The main barrier for the success of these UV designs are shading that result from suspended particles or reactor geometries. Better delivery and distribution of light from LEDs will expedite the adaption of UV-C disinfection.

Optical fibers to deliver light for water treatment applications

Since the 1900s physicists have illustrated the ability to guide signal through high purity glass. This discovery lead to the creation of the optical fiber which quickly revolutionized the telecommunication (i.e. the internet) and laser industry. Here, a signal that is inserted in one end of the optical fiber, travels through it, and emits at the opposite end.

Optical fibers usually have a circular core made of glass or polymer that is encased by one or more coatings termed cladding and secondary coating as illustrated in

Figure 2-4. Traditional optical fibers propagate light axially (transmission) due to complete internal reflection from the lower refractive index cladding surrounding the higher refractive index core (Agrawal, 2010; Mitschke, 2009). These thin glass fibers are remarkably flexible, but scratches or other damage can initiate mechanical failure. The external secondary polymeric coatings protect the glass from breaking when bent. In some applications, only one polymer layer is applied, serving as both the cladding and coating. Commercial-scale optical fiber production is conducted in multi-story drop towers, where the core material is melted, molded and coated through a series of in-line rollers, polymer paths and heating or curing chambers. This produces optical fibers up to kilometers of length.

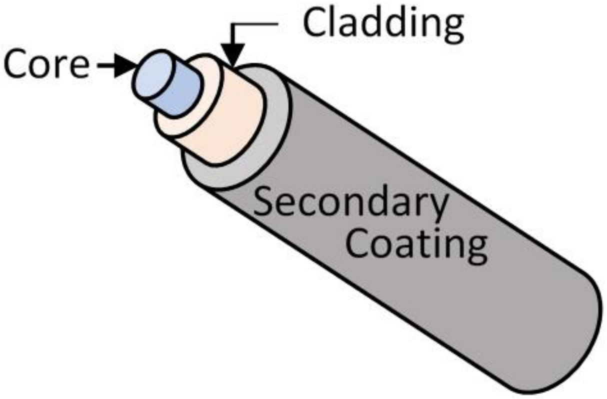

Figure 2-4 Schematic of basic optical fiber configuration including the light guiding core, cladding, and protective coating**.**

Silica core optical fibers are used for long range transmission to transport light in the 1550 nm range but require high working temperatures (1200 ^{o}C) and care. In 1968 the first commercial polymer optical fiber was developed by DuPont from polymethyl methacrylate (PMMA) (Zubia & Arrue, 2001). Benefits of using polymer includes (i) lower working temperatures of about 115 ^{o}C, (ii) high resilience, and (iii) high numerical aperture which guides how much light can be inserted into the fiber. Today, polymeric materials of fabrication also include polystyrene, polycarbonate, and more recently (1995) Cytop®, a fluorinated Teflon-like material (Gries et al., 2017). The higher attenuation through polymer optical fibers limits their consumer use to short range transmission and > 400 nm wavelength applications (Beckers et al., 2015). Today both polymer and silica end emitting optical fibers are used in telecommunication, sensing, medicine and illumination. Table 2.3 lists definitions of terminology used in optical fiber design and research.

Table 2-2 Definitions of terminology used in optical fiber design and research.

Terminology	Definition
Total internal reflection	Continuous propagation of light through a surface.
Index of refraction	A fraction of the speed of light traveling in vacuum to that traveling through the material.
Critical angle	The angle which the light passing through a material will be internally reflected.
Numerical aperture	Range of angles which an optical material can accept or emit light.
Reflection	The return of a light beam into a medium rather than exiting that medium.
Refraction	The exiting of a light beam at an altered angle than its incidence.
Attenuation	The total loss of light both to scattering and absorption.
Absorption	The conversion of light energy into another form (i.e. chemical, heat).
Scattering	The dispersion of a light beam.
Extinction coefficient	Attenuation normalized by the geometric cross-sectional area of the particle.
Absorption coefficient	Absorption normalized by the geometric cross-sectional area of the particle.
Scattering coefficient	Scattering normalized by the geometric cross-sectional area of the particle.
Intrinsic loses	Loss of light from internal properties of the material.
Extrinsic loses	Loss of light as from external impurities or forces to that of the material.
Evanescent waves	An optical field of energy that penetrates through a medium during total internal reflection.

Optical fiber loss and attenuation

Light launched into an optical fiber $\left(I_0(\frac{\mathrm{W}}{\mathrm{cm}^2})\right)$ can be transmitted $\left(I_T(\frac{\mathrm{W}}{\mathrm{cm}^2})\right)$, absorbed$\left(I_A(\frac{\mathrm{W}}{\mathrm{cm}^2})\right)$, or scattered $\left(I_S(\frac{\mathrm{W}}{\mathrm{cm}^2})\right)$ as it travels its length (L (m)), such that:

$$I_0 = I_T + I_A + I_S. \tag{1}$$

In end emitting optical fibers, any light that is absorbed or scattered contributes to the logarithmic decay of light through the length of the fiber, defined as attenuation $(\alpha(\frac{dB_T}{m}))$. The attenuation of light through the optical fiber is described by the Beer-Lamber law (Eq. 2).

$$\alpha = \frac{-10 \cdot log_{10}(\frac{I_T}{I_0})}{L}. \tag{2}$$

Attenuation is due to imperfections inherent to the material properties (intrinsic) or added to the fiber during the fabrication process (extrinsic) (Buck, 2004). In end emitting optical fibers research seeks to minimize both absorptive and scattering attenuation (Agrawal, 2010).

Intrinsic losses are due to the optical fibers core composition and are categorized as either resonance absorption (UV and IR) or Rayleigh scattering. As illustrated in Figure 2.5, intrinsic losses are wavelength dependent. As such, they can be managed through appropriate choice of material composition for the specific wavelength of interest.

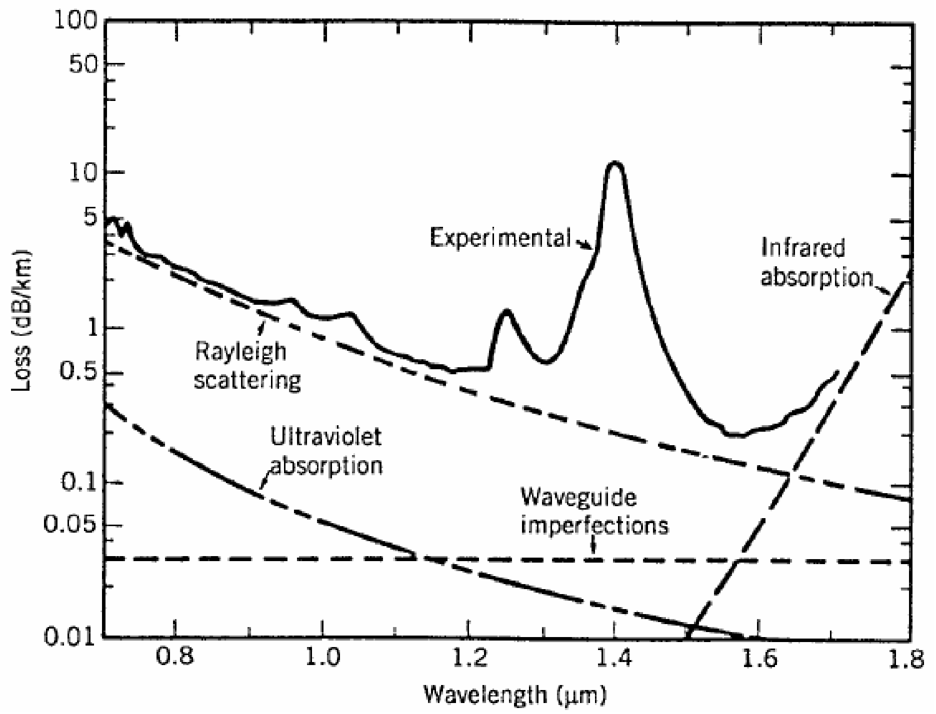

Figure 0-5 Absorption spectrum of optical fibers. Experimental peaks are due to OH vibrational absorption losses. Figure was taken from *Fundamentals of optical fibers* by John A. Buck, Second Edition (Buck, 2004).

Intrinsic resonance absorption occurs when a photon interacts with a structural component of the glass (electrons/metal ions) and transfers its energy to heat due to molecular resonance (Satoh et al., 1999). Absorption due to silica lattice vibrational resonances occurs predominant in the Infrared region of the spectrum (Collins & Fan, 1954). The UV tail of absorption, or Urbach edge is due to electronic resonances from unbound electrons (Fujino, 2005; Jeanmonod et al., 2011). High hydroxyl content in the silica reduces the UV absorption by binding to free electrons.

Intrinsic scattering, or Rayleigh scattering, is due to the elastic excitation and reradiation of light by particles with a diameter of about one tenth the size of the incident wavelength. Rayleigh scattering increase as $1/\lambda^4$, where λ is the wavelength of the propagated light (Zhi et al., 2003). Pure silica glass is amorphous in nature which results in irregularities in the material structure. During manufacture, the glass is rapidly cooled, freezing in the high-temperature microscopic variation. These create variation of refractive index within the optically fiber that act as Rayleigh scattering centers (Lines, 1984).

Extrinsic loses are a result of the optical fiber fabrication and is not associated with the fundamental material property of the glass. The main absorptive extrinsic losses are due to vibrational resonance of the hydroxyl (OH) functional group at 950 nm and 1380 nm and 1240 nm. Any reaction with the outside atmosphere introduces water vapors into the optical fiber that results in increased OH in the optical fiber. One method of significantly reducing OH content in the preform is adding chlorine gas into the preform fabrication chamber to react with any water vapor and exit the system as HCl and O_2. Reducing OH content in the fiber reduces extrinsic absorptive losses in the infrared region but increases intrinsic absorptive losses in the ultraviolet region (see 2.2.1). Therefore, the core material changes depending on the intended application.

Extrinsic scattering losses include bend loss, fiber optic splicing, and macroscopic irregularities to the optical fiber core, cladding or interface. The scattering caused by these irregularities are considered Mie scattering since they are generally of equal (within 1 order of magnitude) or greater size than the incident wavelength (Bunge et al., 2006). Extrinsic scattering is negligible in end emitting optical fibers as great care is taken to remove unintended impurities during fabrication. However, purposeful deposition of macroscopic irregularities is used to fabricate side emitting optical fibers.

Side-Emitting Optical Fibers

Side emitting optical fibers represent a deviation from traditional light guides. Unlike end emitting optical fibers, “leaking” of light into the environment is desirable. To achieve side emission, extrinsic scattering mechanisms are fabricated into the optical fiber. These mechanisms include: (i) micro bending of the fiber axis, (ii) promoting asymmetries in the fibers core or cladding (Chu), (iii) applying cladding material with higher refractive index than the core (Rawson, 1972; Spigulis et al., 1997), and (iv) adding scattering additives into the core or cladding material (Biyarin et al., 2017; Xu et al., 2008a). The result is a “glow-stick” like, or radial emission of light along the length of the optical fiber. Both polymer and quartz cores are used in SEOF. Polymer is more resilient and allows direct etching on to the core or cladding of the fiber. However, silica core is used for longer length and ultraviolet applications to minimize absorptive losses.

Visible light side emitting optical fibers are used in illumination, medicine, and sensor. They can improve aesthetic illumination in appliances, architecture, and electronics. They have been used in fabrics, textiles, costumes and light shows and are made of both polymer and quartz cores. These optical fibers are commercially available for visible applications in length of 1 to 10 m (e.g., Corning) (Patent No. WO2014121172A2, 2017). Zhao et al. illustrated that by coiling the optical fiber and inserting it partially into a liquid, they can serve as liquid-level sensor. Because the liquid has higher index of refraction then air, as the liquid level decreases, the total scattering of light will also decrease (Zhao et al., 2013; Zhao et al., 2012). Increase in transmitted signal is then correlated to lower liquid levels. Klubben et al. proposed the use of visible SEOF for medical applications. SEOFs can deliver controlled light to photosensitizers to produce singlet oxygen that attacks cancer cells. The thin optical fiber can be inserted into the body for vascular, gastrointestinal, neurological and urethral illumination (Klubben et al., 2016). Lastly, Xue et al. arranged SEOF inside a photobioreactor to create layered light and dark regions to simulate light/dark effects for algae growth (2013).

Ultraviolet A (UV-A) SEOFs have also been reported for photocatalytic applications. The first attempts to use optical fiber in water treatment, explored titanium dioxide (TiO_2) nanomaterial as the UV absorption media at the radial surface of the fiber (Peill & Hoffmann, 1997). In this application, the coating and cladding of the optical fiber is removed and TiO_2 is attached directly to the silica core. The UV light refracts out of the fiber due to the higher index of refraction of TiO_2. The light is then absorbed by the TiO_2 generating an electron-electron hole pair for oxidation or reduction of water contaminants (Chong et al., 2010; Esquivel et al., 2009; Hoffmann, et al., 1995; Matthews, 1990; O'Neal et al., 2017; Wu et al., 2014; Yang et al., 2014). Peill and Hoffmann illustrated that for a 1 mm diameter fiber most of the light was emitted through the sides within 15 cm length (Peill & Hoffmann, 1997; Peill & Hoffmann, 1995). Xu et al., increased the length to 5 m by attaching titanium dioxide to the cladding instead of the core, and controlling the side emission by scattering centers (Hu, 2005; Xu et al., 2008b). More recently, UV light emitting diodes (LEDs) have been used in combination with TiO_2 coated optical fibers to maximize light efficiency of flow through reactors (Ling et al., 2017; O'Neal Tugaoen et al., 2018).

Achieving uniformity in side-emitting optical fibers

One of the main barriers of scaling up side-emitting optical fibers is the logarithmic decay of light through its length (see Eq. 1). Various works have tried to achieve uniformity of side emission. Spiguls compares (i) coupling one light source at each end of the optical fiber (Xu et al., 2008b) and (ii) adding a reflector to the distal end of the optical fiber (Figure 2-6). Both options significantly increased the uniformity of side emission throughout the fiber's length, but the second proved to be more cost effective (Spigulis, 2005; Spigulis et al., 1997).

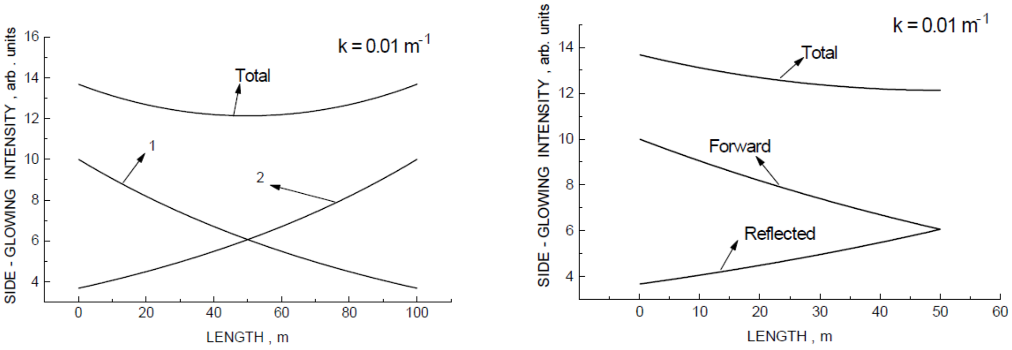

Figure 2-6 Theoretical light emission through the length of an optical fiber with one light source at each end (left) and one light source and one reflector (right). Figure illustrates the emission resulting from the source at each end of the fiber as well as the total sum(Spigulis, 2005).

Biyarin et al. demonstrated theoretical uniformity can be achieved by exponentially increasing the scattering coefficient along the length of the optical fiber (Figure 2-7) (Patent No. WO2014121172A2, 2017). This resulted in fully uniform side emission with a corresponding linear decay in total power remaining in the optical fiber.

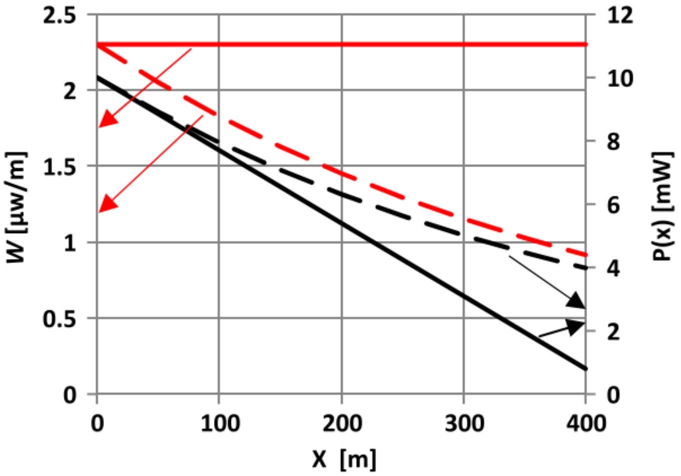

Figure 2-7 Theoretical side emission (red line: uW/m) and total power (black line: mW) through an optical fiber with constant scattering coefficient (dotted line) and exponential increase in scattering coefficient (solid line)(Biyarin et al., 2017).

Both works assume negligible absorption of light for application in visible wavelengths. These assumptions will have to be revisited for ultraviolet side emitting optical fibers since absorption is a significant portion of the attenuation. Nerveless, these results serve as building blocks to the scale up of SEOFs.

Barriers to light assisted water purification

Light can drive and array of water treatment processes. Visible light enables photocatalytic biological remediation and sustains chemotrophic aerobic remediation. Visible and ultraviolet light can be used in both oxidative and reductive photocatalysis and ultraviolet-C radiation can effectively inactivate microorganisms.

These processes allow for water purification without addition of chemicals (i.e. chlorine) or production of disinfection biproducts. However, two key barriers prevent the large-scale integration of light-driven processes into existing water treatment systems. The optical obstructions in aquafers (i.e. granular media) or built infrastructures (i.e. tubing) limit light propagation from a single point source. Side-emitting optical fibers could be used to guide and increase light distribution (>1000 X) in environmental systems and reactors. The second barrier is that high absorbance of UV light by traditional optical fibers has deterred scientists from further exploring side emitting optical fibers in water purification. This dissertation tackles both barriers by first exploring optical fibers for visible light bioremediation and second, systematically modifying optical fibers to side emit from visible to UV-C radiation.

CHAPTER 3

OPTICAL FIBER-MEDIATED PHOTOSYNTHESIS FOR ENHANCED SUBSURFACE OXYGEN DELIVERY

Text from: Lanzarini-Lopes, M., Delgado, A.G., Guo, Y., Dahlen, P., Westerhoff, P. Optical Fiber-Mediated Photosynthesis for Enhanced Subsurface Oxygen Delivery, *Chemosphere*, 2018. 195:742-748. Figures included at the end of the chapter.

Abstract

Remediation of polluted groundwater often requires oxygen delivery into subsurface to sustain aerobic bacteria. Air sparging or injection of oxygen containing solutions (e.g., hydrogen peroxide) into the subsurface are common. In this study visible light was delivered into the subsurface using radially emitting optical fibers. Phototrophic organisms grew near the optical fiber in a saturated sand column. When applying light in on-off cycles, dissolved oxygen (DO) varied from super saturation levels of >15 mg DO/L in presence of light to under-saturation (<5 mg DO/L) in absence of light. Non-photosynthetic bacteria dominated at longer radial distances from the fiber, presumably supported by soluble microbial products produced by the photosynthetic microorganisms. The dissolved oxygen variations alter redox condition changes in response to light demonstrate the potential to biologically deliver oxygen into the subsurface and support a diverse microbial community. The ability to deliver oxygen and modulate redox conditions on diurnal cycles using solar light may provide a sustainable, long term strategy for increasing dissolved oxygen levels in subsurface environments and maintaining diverse biological communities.

Keywords: solar, biodegradation, contamination, groundwater, soil

Introduction

Subsurface microbial communities depend on adequate oxygen supply to maintain an aerobically-active environment (Nivala et al., 2013). Aerobic biodegradation of many organic pollutants in groundwater require artificial oxygen addition to support microbial communities (i.e., oxygen serves as the electron acceptor or the initial reactant in the activation of certain organic pollutants) (Chapelle, 1999; Hess et al., 1996; Khan et al., 2004; Korda et al., 1997). Artificial water level fluctuation is used to enhance oxygen transfer at the biofilm surface (Austin et al., 2003). Other conventional artificial aeration techniques include both mechanical and chemical technologies such as air sparging, liquid oxygen injection, and hydrogen peroxide injection, which all demand high energy inputs (Chapelle, 1999). Many contaminated groundwater sites may require decades of remedial activity, and may not be located near the power grids (i.e., developing countries or remote locations). While solar panels could be used to power pumps, most photovoltaic panels achieve ~20% efficiency in converting solar light to usable electricity. Thus, there is a need to develop more sustainable long-term technologies to deliver light into the subsurface to aid in groundwater remediation.

Natural oxygen transfer in an environment occurs via three primary mechanisms: 1) atmospheric diffusion, 2) plant-mediated oxygen transfer, and 3) oxygen transfer at the biofilm interface (Nivala et al., 2013). Atmospheric diffusion occurs predominantly only at the water surfaces or water-soil interfaces, and penetrates slowly through soils. Although atmospheric diffusion can assist subsurface convection in diffusion of dissolved oxygen, it is unlikely to have an impact on oxygen availability for microbial communities because oxygen diffusion is limited to only ~0.11 g/m^2-d in the subsurface (Tanner &

Kadlec, 2003). Plant-mediated oxygen transfer is related to the root release of oxygen through passive diffusion and varies based on oxygen demand of the surrounding environment and the season. The rate of transfer is highly debated as it is difficult to measure oxygen concentration at the root surface. Oxygen release concentration ranges from 0.005 to 12 g/m^2-d (Armstrong, & Beckett, 1990; Bezbaruah & Zhang, 2005).This rate of release does not meet demand exerted by highly active aerobic subsurface microbial communities, but does directly and indirectly affect, among other components, the structure, diversity and function of that community (Faulwetter et al., 2009; Gagnon et al., 2007; Wu et al., 2011; Zhu & Sikora, 1995). Oxygen transfer to biofilm surface also occurs through natural cycle of filling and draining of the environment. As a subsurface bed is drained, exposed biofilms are oxygenated, improving microbial respiration and biological activity compared to static beds (Green et al., 1997; Tanner et a., 1999).

Photosynthesis produces oxygen. However, sunlight does not penetrate soil beyond ~10 mm (Tester & Morris, 1987). The technological barrier to using photosynthetic microorganisms beyond the surface (e.g., for soil or groundwater bioremediation) is discovery of new light delivery technologies. Optical fibers could be used to overcome this barrier. Optical fibers have been used to transfer light/solar energy axially (telecommunication application), and a number of laboratory studies using algae have demonstrated their effectiveness in promoting photosynthetic growth in water (Mori et al., 1987; Peill & Hoffmann, 1997; Tekelioglu & Wood, 2009; Xue et al., 2013). Studies using optical fibers coated with photocatalysts (e.g., TiO_2) showed that natural sunlight is absorbed radially and pollutant chemical oxidation occurs via $OH^{\bullet}$ radical production (Peill & Hoffmann, 1997). Unlike chemical oxidation, through this work we aimed to produce oxygen biologically to subsequently promote microbial growth.

Here we explore a sustainable, direct solar input technology approach to obtain an oxygen-rich subsurface environment. The concept is to stimulate oxygen surplus by growing photosynthetic microorganisms in soils by delivering natural sunlight to the subsurface in a passive biological treatment wall-like system (Khan et al., 2004). This allows for oxygen transfer directly into the biofilm without the need for high energy mechanical aeration or addition of dissolved gases or chemical oxidants (Behrends et a., 2001). With sufficient light, photosynthetic microorganisms convert carbon dioxide into cellular material and generate oxygen. Oxygen can subsequently serve as an electron acceptor and metabolic co-reactant for a wide-range of microorganisms and increase biodiversity. Furthermore, phototrophic cellular and extracellular organic material can provide substrate for a diverse group of microbes to aid in pollutant degradation (Filip et al., 1979). Thus, carbon present in water and soils can be cycled between inorganic and organic forms in a sustainable strategy, rather than through continuous addition of conventional electron donors (e.g., methanol).

In this study, we connected a white light source to a polymer coated optical fiber that radially emitted light along its length, and then inserted the optical fiber into a column photobioreactor packed with sand. The polymer layer allowed the fiber to diffuse light radially along the sand column. Changes in dissolved oxygen (DO) were closely monitored when the light was provided continuously and in on-off cycles. Microbiological analyses were performed to understand the effect of light delivery on microbial community structure and function within the sand photobioreactor. These results provide insights on subsurface microbial photosynthesis and bring proof-of-concept evidence towards the development of novel, sustainable soil and groundwater oxygen delivery technologies. Ultimately, this technology would use concentrated solar light rather than, or in addition to, artificial light.

Materials and Methods

Photobioreactor Design and Operation

The photobioreactor used to demonstrate our concept consisted of a 70 cm long by 50.8 mm diameter air tight and opaque PVC single column packed with 61 cm Quikrete play sand (2.50 kg sand dry weight) pre-washed with deionized water (Figure 3-1). A sponge scouring pad and a layer of granite were placed above and below the playground sand to prevent uneven water flow. Before packing into the reactor, the playground sand was inoculated with a 350 mL of a photosynthetic enrichment culture derived from lake water (Tempe Town Lake, AZ, USA). The enrichment inoculum culture was grown in BG-11 medium with the composition per liter as follows: 2.86 mg boric acid; 1.81 mg manganese chloride tetrahydrate; 0.22 mg zinc sulfate heptahydrate; 0.079 mg copper(II) sulfate pentahydrate; 0.05 mg colbalt(II) chloride hexahydrate; 0.4 mg sodium modybdate; 30.5 mg dipotassium phosphate; 73.5 mg magnesium sulfate heptahydrate; 36.0 mg sodium chloride; 6.0 mg ferric ammonium citrate; 750.0 mg sodium nitrate; 20.0 mg sodium carbonate(Rippka, Deruelles, Waterbury, Herdman, & Stanier, 1979). A 5 mm diameter plastic optical fiber coated in white polymer to emit light radially was positioned through the center of the column and connected to an artificial visible light source (Encore Fiber Optic Illuminator model AR150CM-4-120M-D-CW with a 150W M type Lamp). Light intensity was measured by Avantes spectrometer (AvaSpec-2048L-USB2). The intensity was measured at every inch through the radiated fiber before placing it in the reactor.

The photobioreactor was operated in semi-batch mode at room temperature (22℃). The inlet medium flow through the column was 100 mL/day, pumped from reactor bottom to top using a Cole Parmer Masterflex Peristaltic Pump (Vernon Hills, IL). An average light intensity of 20 µmol/s-m^2 in the visible spectrum (400–700 nm) was emitted through the column continuously for the first 7 days. Light was then emitted in a 24 hour on-light off-light cycle for 7 days. Each cycle was completed at 9 am every morning, at which time, a sample was taken, the DO level was taken at each port and the lamp was turned to the opposite setting from the night before. A control reactor was setup to monitor the dissolved oxygen (DO) consumption in the absence of light using the same design parameters, column flow rate, and BG-11 medium composition. The oxygen, nitrate and phosphate concentration were measured at the influent and effluent for a period of four days.

Chemical and Microbiological Analyses

Influent and effluent DO were measured using dissolved oxygen meter (YSI 550A, Yellow Springs, Ohio) through air-tight flow paths. The instrument was calibrated in 3 conditions. First with a 100% saturated air environment where the probe is stored. Second, in oxygen saturated water by flowing oxygen through water continuously until it reaches saturation. Finally in an oxygen-less environment by purging water of oxygen with a nitrogen gas flow. Phosphate and nitrate were measured in the influent and effluent via ion chromatography (Standard bore separator, Dionex^{tm} IonPac^{tm} AS18 column) with 30mM KOH eluent following EPA Standard Method 300 according to published methodology (Doudrick et al., 2013; Yang et al., 2013).

The relative abundance of phototrophic microorganism and the microbial community structure were determined at the end of the experiment. The column was cut into 8 cross sections (as shown in Figure 3-1) and these sections were used for microbial analyses. Phototrophic colony forming units were quantified in sections 2, 4, and 6 to determine their radial and vertical distribution. For this analysis, 1 g of homogenously mixed sand from each cross-sectional area was diluted in 10 mL of 1X PBS and vortexed for ~1 min using a tabletop vortex. The sand/PBS slurry was serially diluted and plated onto BG-11 agar plates containing 1.5% agar. Duplicate plates were setup for each dilution. The plates were incubated at room temperature with the same light intensity as the SPOFR. Green (phototrophic) colonies were counted after 5 days incubation when colonies became visible for reliable counting. Non-green colonies (e.g., heterotrophic bacteria growing on phototrophic soluble products and/or organic carbon from BG-11 medium) were also counted.

Genomic DNA was extracted from sections 1, 3, and 5 from 0.25 g of wet sand using a MoBio PowerSoil® DNA Isolation Kit according to the manufacturer's instructions. Duplicate extractions were performed from each section. An average of 60,000 taxonomy reads were found per sample in the SPOFR. Microbial community amplicon sequencing using primers 515F and 806R for the V4 hyper-variable region of the 16S rRNA gene was performed using the Illumina MiSeq platform at the Microbiome Analysis Laboratory in the Biodesign Swette Center for Environmental Biotechnology at Arizona State University ("Microbiome analysis laboratory,"). Details on library preparation, instrument chemistry, and data analysis were previously published (Chen et al., 2016; Delgado et al., 2017). Briefly, raw sequences were paired using QIIME 1.8.0 pipeline. Sequences shorter than 250 bps, with a quality score ≤25, with 1 or more primer mismatches, or with more than 6 homopolymers were excluded from the analysis. Operational taxonomy units (OTUs) were picked based on 97% sequence similarity from the remaining sequences using the UCLUST algorithm(Edgar, 2010). The most abundant sequence of each cluster was chosen as the representative sequence of the OTU and then aligned to the Greengenes database using PyNAST (Caporaso et al., 2010). Chimeric sequences were identified via Chimera Slayer(Haas et al., 2011) and were then removed. UCLUST was used to assign taxonomy to Greengenes database in order to construct a BIOM formatted OTU table (DeSantis et al., 2006). Singletons were removed from the OTU table and the OTU table was rarefied at the lowest number of sequences using Qime’s default pseudo-random number generator (52241). Alpha and beta diversity profiles where analyzed to indicate samples inter and intra microbial diversity respectively.

Results and Discussion

Dynamic Oxygen Production and Consumption Patterns Under Different Light Regimens

The ability of optical fibers to deliver visible light capable of increasing photosynthetic activity and, therefore, increasing oxygen levels in a subsurface environment was experimentally investigated. Figure 3-2 illustrates the effectiveness of using fiber optics to increase oxygen in a subsurface environment. During days 1-7, continuous light and medium containing DO, below the temperature dependent saturation level (7.6 mg/L) was provided to the reactor. The oxygen concentration at the outlet nearly doubled, reaching a super-saturated level of 15 mg/L (DO saturation at 22 °C is 8.7 mg/L) (Water Quality Factors Reference Unit). During light on/off cycles, the DO fluctuated from over saturation to under saturation. Average DO levels for light on and off cycles were 12.3 mg/L and 7.9 mg/L, respectively. The increase in DO upon light application was indicative of a photosynthetically-active microbial community. Decreasing DO concentrations during off cycles were indicative of aerobic respiration by a high activity of microorganisms (Jørgensen et al., 1979).

In the absence of light (Control column in Figure 3-3), DO decreased to 1.75–2.6 mg/L. On day 7, the column had a DO level of 12.5mg/L. At an HRT of 36 hours, dilution of oxygen by diffusion contributes to the decrease in DO, lowering the level to 9mg/L. In all cases, the oxygen increase in the soil column corresponded to the light availability. During light application, photons presumably promoted photosynthesis, which increased oxygen at a faster rate than the microbial communities consume. During light-off days (i.e., no light periods), microbial respiration consumes the available oxygen(Jørgensen et al., 1979). In the absence of light in the control reactor (Figure 3-3) DO decreased by 79% over a 4 day period. This 5.0 mg/L of oxygen consumption would decrease the overall oxygen level in the bioreactor. Phototrophs are also responsible for decrease in oxygen through aerobic respiration when no light was provided (Dixon & Kahn, 2004).

Some phototrophs fix nitrogen from the atmosphere, while others utilize dissolved nitrogen; all organisms also require phosphorous. Both nitrogen and phosphorous are required for biomass growth, and the average consumption in these nutrients occurred at a ratio 18.6 mg-N/mg-P, which is close to the Redfield ratios in soil and soil bacteria (Anderson & Sarmiento, 1994; Cleveland & Liptzin, 2007). Figure 3-2 shows the nitrate and phosphate levels in the photobioreactor. The column influent water contained high levels of nitrate (526 mg/L) and phosphate (12 mg/L), as is typical in initial algae growth culturing experiments. Nutrients consumption is an indicator of microbiological activity within our subsurface reactor. Nitrate decreased by an average of 50% in the initial 5 days of testing then stabilized at a 10% decrease. Phosphate decreased by an average of 92% consistently throughout the experiment in both the light-on and light-off cycles. An independent-samples t-test was conducted to compare the nitrate and phosphate concentration during the initial 4 days of light-on and the 4 days of light-off (control) conditions (Table SI1). There was a significant difference in the concentration of both phosphate (p = 9.0 E-07) and nitrate (p = 1.1 E-03). These results suggest that there is a significant correlation (> 95%) between light treatment and concentration of phosphate and nitrate. Nitrate can be removed by microorganisms through both assimilatory and dissimilatory nitrate reduction (e.g. denitrification or respiratory ammonification) (Dixon & Kahn, 2004),(Ghiorse & Wilson, 1988). Future work should explore the nutrient requirements to initiate and maintain active phototrophic productivity. It is possible that nutrient salts could simply be coated onto the optical fiber and delivered only during the initial installation to initiate rapid microbial growth.

As the oxygen level in the reactor increased, the nitrate consumption decreased. In the deficiency of oxygen, the respiratory electron transport chain can use sulfate or nitrate, among other compounds, as the electron acceptors (Paul & Clark, 1989b). These molecules have lower reduction potential than oxygen, therefore as oxygen becomes available it becomes preferential in respiration, and nitrate consumption is lowered. Figure 3-3 shows the decrease in nitrate and phosphate in the absence of light. Phosphate can adsorb to the sand particles containing iron, manganese or other elements, but is also lowered by both heterotrophic and phototrophic growth (Paul & Clark, 1989a). In the control column inlet nitrate and phosphate decreased by 1.5% and 15%, respectively indicating that the majority of the nutrient reduction was microbial induced and not adsorption to sand and/or dilution by continuously feeding the medium. Collectively, the photo bioreactor provided a proof of concept that DO could be produced in-situ using a mixed culture of photosynthetic microorganisms with continuous flow through a simulated subsurface environment. These high nutrient levels favor biological growth, but would not necessarily be crucial in native groundwater sources. In field settings, initial development of biofilms may require longer initiation times or short term addition of nutrients. These nutrients could be pretreated solids on the optical fibers.

Abundance and Diversity of Phototrophic Microorganisms in the Photobioreactor

The relative abundance and microbial community structure were determined by plating and high throughput sequencing to understand the distribution of phototrophic and heterotrophic organisms spatially throughout the packed soil column. Green colony forming units in the different sections of the reactor are shown in Figure 3-4. The concentration of green colonies was stable throughout the column at $1.36 \times 10^5 \pm 2.28 \times 10^3$ CFU/g-sand. Radial samples (Figure 3-1) revealed 3.02×10^5 CFU/g-sand of green colonies in the inner radius closest to the light source (Section A) and a consistent 7.42×10^4 CFU/g-sand beyond 7.62 mm radial distance from the fiber (Sections B and C)

(Figure 3-4). The average density of the non-green microorganisms was $1.19 \times 10^5 \pm 2.34 \times 10^3$ CFU/g-sand for all the samples.

The relative abundance of the microorganisms as determined by plating illustrates that the majority of the photosynthetic growth occurred within the first 7.62 mm of the radial profile (Figure 3-4). The photosynthetic microorganisms beyond 7.62 mm from the fiber are most likely due to mixing from the water flow. No green colonies were detected on BG-11 plates from reactor effluent within 5 days of incubation, suggesting that the photosynthetic microorganisms were tightly bound to the sand inside the bioreactor. The light delivered through the reactor dropped exponentially along the fiber length from inlet to outlet, from 20 μmol/s-m^2 at 0 m to 10 μmol/s-m^2 at 1.52 m. The higher microorganism count in the influent and effluent of the reactor is due to higher light exposure and higher nutrient availability, respectively.

The microbial community structure was determined through high throughput sequencing of the chromosomal DNA. An average of 60,000 sequences were produced per sample. Alpha diversity analysis (Table SI2) showed the lowest microbial diversity near the light source (inner radius) with ideal phototrophic conditions. Beta diversity (Figure SI 3-1) analysis illustrate similar diversity profiles for the center and outer radius (samples 3B and 3C) which are distinctly different from the inner radius (sample 3A). As illustrated in Figure 3-5, sequences most similar to photosynthetic algae and bacteria were highly enriched in the bioreactor. Sequences of algae (e.g., *Acutodesmus obliquus* and *Chlorotetraedron incuss*) and cyanobacteria (S*ynechococcus spp.*) accounted for 35-50% of the microbial community along the length of the bioreactor (Figure 3-5, column sections 1, 3, and 5). The highest relative abundance of photosynthetic microorganisms was observed in the section most closely to the fiber (60% in Figure 3-5, column section 3A). Overall, Miseq sequencing data are in good agreement with the results from plating showing the highest concentration of green colonies where the light was at most intense (Figure 3-4).

Non-photosynthetic microbes detected included phylotypes mostly related to *Bacteroidetes*, *Verrocomicrobia* and *Proteobacteria*. These microbial groups could have been involved in nitrogen removal in the optical fiber column(Biology & Sciences, 2007; Paul & Clark, 1989c); however, their direct role was not investigated experimentally. The non-photosynthetic microorganisms found in our bioreactor are commonly associated with biologically active soil/sediment environments where O_2 respiration is occurring (Fierer & Jackson, 2005; Paul & Clark, 1989a, 1989b). The microbial community structure and relative abundance highlights the establishment of a light-driven, dynamic environment that allowed for growth and mutually benefiting relationships of photosynthetic and non-photosynthetic microorganisms.

Conclusion

Experimental evidence demonstrated the feasibility of using radial emitting optical fibers to deliver light into the subsurface and increase DO due to a microbiological response to light stimulation. Microbial community sequencing and plating indicated that mutually beneficial relationships were established between photosynthetic and non-photosynthetic microorganisms. These research findings support making further investments in sustainable oxygen delivery to subsurface environments. Ultimately, solar light alone or augmented by artificial light, could be used. Artificial light in “red” wavelengths are efficiently utilized by plants, green algae, and cyanobacteria. White or colored light cold be used to initiate phototrophs through 24 hour illumination, or tailored with different wavelengths to favor certain microbial communities (Kuo et al., 2012).

Acknowledgements

This work was partially funded by NSF IGERT-SUN program at Arizona State University and through the Nano-Enabled Water Treatment Technologies Nanosystems Engineering Research Center by the National Science Foundation (EEC-1449500). Initial discussions with Kyle Doudrick and Chevron were helpful in initiating this research. Technical editing was provided by Laurel Passantino.

Figures

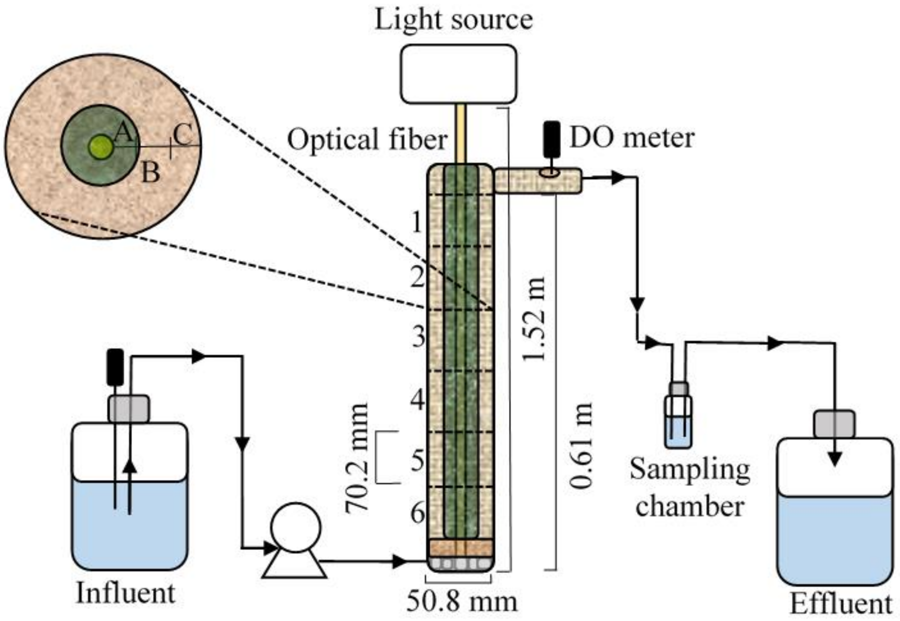

Figure 3-1. Sand Packed Optical Fiber Reactor (SPOFR) design and process schematic illustrating sample ports, analysis segments (1-6) and cross sections (A, B, C). The arrows denote the flow of medium.

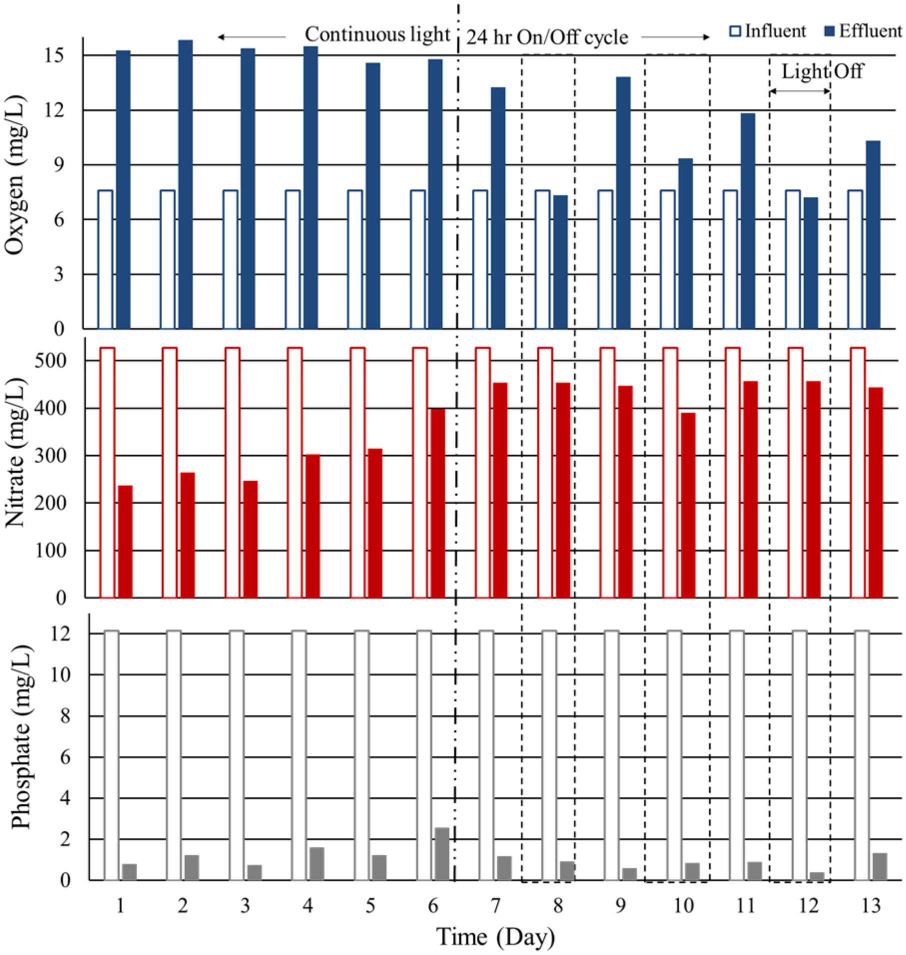

Figure 3-2 Dissolved oxygen , nitrate and phosphate at the influent (white bars) and effluent (dark bars) during bioreactor operation.

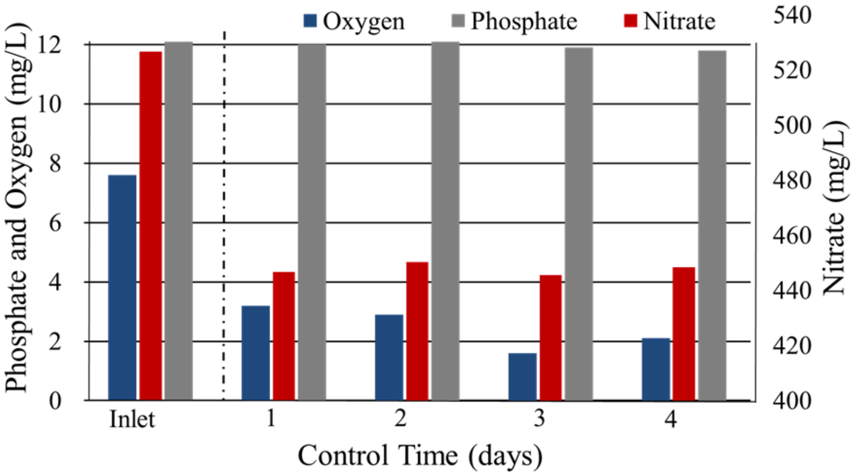

Figure 3-3 Concentration of phosphate, oxygen and nitrate in the control column inlet and outlet for four control days with no light.

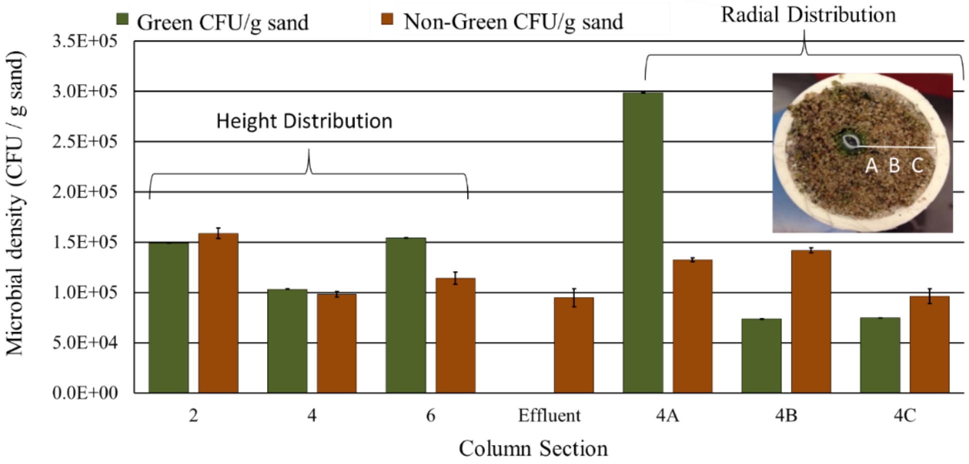

Figure 3-4 Concentrations of green colony forming units through the photobioreactor.

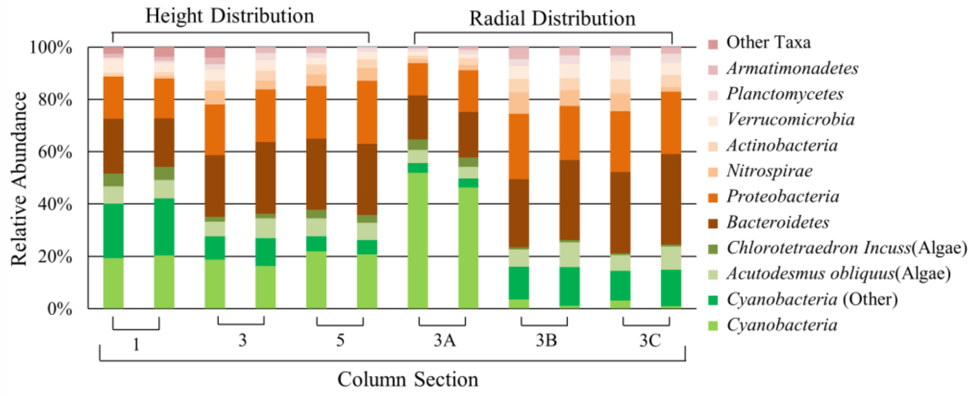

Figure 3-5 Radial and axial relative abundance of microbial groups within the photobioreactor.

Supplemental Information

Table S.I. 3- 1 Independent-samples t-test data and results for statistical analysis of light treatment correlation with phosphate and nitrate concentration.

	Phosphate		**Nitrate**	
	light-on	light-off	light-on	light-off
1	0.8 mg/L	12.0 mg/L	236.9 mg/L	446.7 mg/L
2	1.2 mg/L	12.1 mg/L	263.8 mg/L	450.2 mg/L
3	0.7 mg/L	11.9 mg/L	246.5 mg/L	445.6 mg/L
4	1.6 mg/L	11.8 mg/L	302.8 mg/L	448.3 mg/L
Standard Deviation	0.4	0.1	29.1	2.0
Mean	1.1	12.0	262.5	447.7
P(T<=t) two-tail	**9.0E-07**		**1.1E-03**	

Table S.I. 3- 2 PD whole tree and Observed OTUs alpha diversity distribution.

Sample	**PD whole tree**	**Observed OTUs**
Inlet (1)	77.7	1873.1
Outlet (5)	76.4	1810.9
Inner radius (3A)	66.0	1492.2
Center radius (3B)	77.5	1879.4
Outer radius (3C)	78.5	1944.3

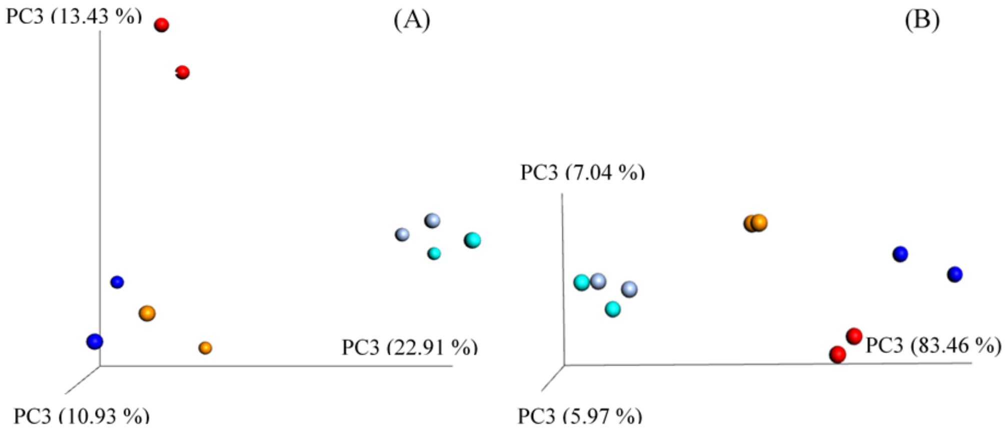

Figure S.I. 3-1 Unweighted (A) and weighted (B) beta diversity for samples 1(●), 5(●), 3A (●), 3B (●), 3C (●) from Figure 1.

CHAPTER 4

PARTICLE-MODIFIED POLYMERIC CLADDING ON GLASS OPTICAL FIBERS ENHANCES RADIAL LIGHT SCATTERING

Text from: Lanzarini-Lopes, M., Garcia-Segura, S., Hristovski, Simons, A. J., Messerly, M., K., Westerhoff, P. Particle-modified polymeric cladding on glass optical fibers enhances radial light scattering. *Journal of Optical Society of America B: Optical Physics*, 36(6), pp. 1623-1628. Figures included at the end of the chapter.

Abstract

Radially light-emitting optical fibers are of increasing interest for applications in medicine, visible aesthetics, and environmental remediation. Optical fibers contain a light guiding core coated by protective polymer layers (cladding and coating), which assure both the strength and flexibility of the optical fiber. This paper examines the feasibility of scattering light radially from fibers by loading the fiber cladding with particle scattering centers during the optical fiber fabrication process. This work uses an in-line full-scale scalable facility to coat the fibers and control the polymer cladding and silica sphere. Loadings up to 2.0 % wt. of 500-nm silica particles on the cladding of the optical fiber led to an average of 95 times higher scattering for visible light and up to 10 times higher in the UV-A wavelength range compared against cladding without particle modifications. This study illustrated feasibility of fabricating broad-band light scattering optical fibers for use with modified polymeric cladding.

Introduction

The ability to radially scatter light out of optical fibers is of interest for many applications. Visually, diffusive optical fibers can improve aesthetic illumination in appliances, architecture, and electronics. Medically, tissue illumination, phototherapy, and sterilization require well-distributed light in tight instrumentation (Klubben et al., 2016). Environmentally, visible light enhance growth of phototrophic organisms in dark or untraditional geometries (Lanzarini-Lopes et al., 2008), and ultraviolet light is used in disinfection and oxidation of organic micropollutants (Lui et al., 2016; Xu et al., 2008). There is a need to fabricate tunable light scattering optical fibers in the UV and visible wavelengths to be used in the above applications.

Various methods are reported to obtain external fiber light scattering from within optical fibers including: (i) micro bending of the fiber axis, (ii) fabricating or manufacturing asymmetries in the fibers core or cladding, (iii) applying cladding material with higher refractive index than the core (Rawson, 1972; Spigulis et al., 1997), and (iv) adding scattering or fluorescent additives into the core or cladding material (Biyarin et al., 2017; Xu et al., 2008). Coating optical fibers with additives can optimize the emission from Rayleigh and small angle scattering (Biyarin et al., 2017). Most research has focused on enabling radial light emission from optical fibers using single light wavelengths and linear laser light sources. Barrier remain in understanding how loading of scattering centers affects light emission and in how to use optical fiber with broader wavelength and lower intensity light sources (e.g., solar spectrum and LED arrays). The goals of this study are to (i) understand how adding different scattering center materials and loadings affects the Mie-scattering-induced light emission of the optical fiber at wavelengths from 350 nm (UV-A) to 570 nm (visible), and (ii) demonstrate the feasibility and accuracy of in-line cladding modification.

To address these goals, three scattering center types were selected to span a range of commonly available particles: barium sulfate, a white crystalline polytetrafluorethylene powder (Zonyl™), and silica microspheres (500-nm). Barium sulfate (powder) and zonyl (powder) have been used in integrating spheres due to the high reflectance and near Lambertian characteristics (Roos & Ribbing, 1988; *Zonyl ™ MP 1200*, 2015). Preliminary experiments (See S.I. Figure 4-1) with barium sulfate and Zonyl showed minimum increase in radial scattering compared to that of the unmodified optical fiber (UV = 1.3 X and visible = 7.0 X for barium sulfate and UV = 0.4 X and visible = 6.0 X for Zonyl). Attachment of 500-nm SiO_2 particles illustrated increases of UV = 9.7 X and visible = 95.2 X. Therefore, the majority of this study focuses on SiO_2 particles as scattering centers within external polymeric cladding on optical fibers. Our work differs from prior work by observing the impact of the scattering centers on a broad spectrum (UV-A to visible light) instead of a single wavelength illuminated by laser. This allows us to visualize the limitations of fabricating UV scattering optical fibers. Additionally, our method of inducing scattering can be adapted to any existing optical fiber draw towers.

Methodology

1.1.1 Custom Fiber Fabrication

Custom optical fibers were manufactured at Lawrence Livermore National Laboratory in an 8.2 m tall draw tower. As illustrated in Figure 4-1, fused silica glass rods F300 (Haraeus Gmbh) with 26 mm outer diameter were used as the raw material (preform) to draw 250-μm optical fibers. Briefly, the preform was placed in a 1,900 °C drawing furnace and dropped three stories through two sets of polymer dies (primary coating (cladding) and secondary coating) at 1.2- and 3.0-meters distance from the drawing furnace before being wound into 0.2 m diameter drums.

Polymer solutions were degassed in a low vacuum before connecting them to the die to avoid the formation of gas bubbles in the polymer. The nominal thickness of the applied polymer on the optical fiber the difference between the die size and the fiber diameter divided by two. A 330 μm die was used to apply the 40 μm thick polymer cladding (DeSolite DF-0016, DSM Desotech Inc.) followed by a 480 μm die to apply the 75 μm thick fiber secondary polymer coating (DeSolite DS-2015, DSM Desotech Inc). Each polymer was UV cured at 387 nm after its application, causing the material to shrink slightly.

To induce scattering of light from the optical fiber core, functionalization of the cladding was tuned by loading silica microspheres (500-nm, Sigma-Aldrich: 805890) in the polymer at 0.5 % wt., 1.0 % wt., and 2.0 % wt. The 500 nm particle diameter was chosen to induce equal scattering along all wavelengths (Mie scattering) as explained later. The microspheres were added to the DeSolite DF-0016 (cladding polymer) and rapidly hand mixed for 20 minutes. The mixture was sonicated in a water bath for 4 hours and hand stirred for 10 additional minutes. The solution was again degassed in a low vacuum before connecting it to the primary coating die. An unmodified external polymer coating was applied to all of the optical fibers for additional protection.

A reference optical fiber with no modifications to the cladding (neat-clad) was fabricated and analyzed for comparison. Physical characterization of the optical fiber was obtained through 40X magnification microscope images through reflection mode (Leica DM6 B).

1.1.2 Optical Characterization and Apparatus

Light launched into an optical fiber $\left(I_0(\frac{\mathrm{W}}{\mathrm{cm}^2})\right)$ can be transmitted $\left(I_T(\frac{\mathrm{W}}{\mathrm{cm}^2})\right)$, absorbed $\left(I_A(\frac{\mathrm{W}}{\mathrm{cm}^2})\right)$, or scattered $\left(I_S(\frac{\mathrm{W}}{\mathrm{cm}^2})\right)$ as it travels its length (L (m)) such that summation of terms accounts for all the light:

$$I_0 = I_T + I_A + I_S \tag{1}$$

Attenuation ($\alpha(\frac{dB_T}{m})$) through the optical fiber, described by the Beer-Lambert law Eq. (2), relates I_T to the properties of the material that it is traveling through.

$$\alpha = \frac{-10 \cdot log_{10}(\frac{I_T}{I_0})}{L} \tag{2}$$

As illustrated in Figure 4-2, adding silica to cladding directly influences the attenuation through the optical fiber by scattering light away from the guiding core (See (A) in Figure 4-2). Scattering centers cause light to either exit the fiber ((B) in Figure 4-2) and be measured as I_S or be absorbed by the polymer cladding/coating ((C) in Figure 4-2). Attenuation is quantified by the cutback method, where the fiber is cut back 3.0 m from 5.0 m long to 2.0 m long. Equation 2 is then used to calculate α by measuring the transmittance at both 5.0 m (I_T) and 2.0 m (I_0). The scattered flux at a specific length ($I_{S,L}$) is also normalized by I_0 and reported as the fractional scattered flux ($\frac{I_{S,L}}{I_0}$).

Figure 4-3 illustrates the optical analysis setup used for both measurements. Light from a deuterium lamp (Newport, Q Series 30W) was directed though a spectrometer

(HORIBA Jobin Yvon microHR) allowing monochromatic light analysis of selected wavelengths between 350 and 570 nm. Two planar-convex lenses (Thorlabs LA4148) were used to further couple the light into the optical fiber. An optical chopper (Thorlabs MC2000B controller and MC1F15 blade) reduced the signal noise by communicating a frequency signal to the photon counter detector (Model SR830 DSp Lock-in Amplifier Stanford Research Systems). The sensor was a bialkali photocathode coupled to a silica glass window photomultiplier tube (PMT) (Hamamatsu R760). $I_{S,L}$ was measured by guiding the optical fiber through a 50.8 mm diameter integrating sphere (Thorlabs IS200-4). The integrating sphere is a hollow spherical cavity covered with a diffuse white reflective coating that allows all of the light scattered from the optical fiber to be captured and quantified.

Results and Discussion

Optical Fiber Characterization

Figure 4-4 shows the core, cladding, and coating of the optical fiber circular faces and shows scattering centers (i.e., silica spheres) in the cladding for silica loadings up to 2.0 % wt. The particles were not only present at the cladding-core interface but appeared well distributed throughout the thickness of the cladding. The thickness of the polymer cladding and coating after the curing process are 31.3 μm (± 5.3 %) and 62.8 μm (± 4.8 %), respectively. The polymer cladding and coating protects and strengthens the optical fiber, allowing it to bend without breaking (higher flexibility). To increase the scattered flux, a higher density of homogenously-dispersed particles is desired to increase photon–particle interaction that results in scattering (Ballato et al., 2008). However, loadings >2.0

% wt. resulted in brittle coated fibers. Therefore, only loadings up to 2.0 % wt. are presented in this paper.

Functionalization Effect on Scattering Flux

Scattering flux through optical fibers can be increased by (i) increasing the scattering opportunities and (ii) decreasing absorption of light. Both the cladding and coating are highly absorbing in the UV region (S.I. Figure 4-2). The presence of silica on the interface between the optical fiber core and cladding both increases the scattering opportunities and partially replaces the highly absorbing cladding polymer.

There are two main types of linear light scattering in optical fibers: Mie and Raleigh scattering. Rayleigh scattering refers to the elastic scattering of light from a particle with a diameter (*D*) of about one-tenth the size of the incident wavelength ($\frac{\pi D}{\lambda} \ll 1$). Rayleigh scattering is defined by Eq. (3) where R is the distance of the scattering object from the detector, n is the number of scattering objects, λ is the wavelength of the propagated light, and θ is the scattering angle. Rayleigh scattering is mostly due to inherent uniformities within the optical fiber's core molecular structure and increases as $1/\lambda^4$ (Zhi et al., 2003).

$$I_S = I_0 \, \frac{1+ cos^2\theta}{2R^2} (\frac{2\pi}{\lambda})^4 (\frac{n^2-1}{n^2+1})^2 (\frac{D}{2})^6 \qquad (3)$$

Mie scattering occurs when the deformity is of equal (within 1 order of magnitude) or greater size than the incident wavelength. Mie scattering is identified by the ability of particles to scatter all wavelengths of white light equally (Bunge et al., 2006). We used these principles to understand our measured values of fractional scattered flux. The constant scattering in the visible range with a decrease in scattering in the UV region (where polymer illustrates high absorption) is therefore likely due to the absorption of light by the material.

Figure 4-5 shows the effect of incorporating silica spheres within the cladding on the fractional scattered flux. Scattering increased for all wavelengths as silica particles loading on the fiber increased from 0.5 % wt. to 2.0 % wt. Rayleigh scattering was illustrated in the 0 % wt. optical fiber where scattering increased as wavelength decreased. The equal increase of visible light scattering upon the addition of 500-nm silica spheres indicates that Mie scattering is the primary mechanism of increased scattering flux (see Figure 4-5) for the modified optical fiber.

The scattering flux tripled when the SiO_2 loading increased from 1.0 % wt. to the 2.0 % wt. As illustrated Figure 4-5, the 2.0 % wt. SiO_2-clad increased the scattered flux ratio by 9.7 X to 30.3 X in the UV-A range and 95.2 X for visible light when compared to the neat-clad fiber. This increase in scattering was due to a much higher photon to particle interaction and to the replacement of the polymer cladding, which decreased absorption by the polymer.

To investigate how attenuation through the fiber affects scattering distribution for both UV-A and visible light, the scattered flux was measured at different positions along the fiber (0.0 m, 0.5 m, 1.0 m, 1.5 m, 2.0 m, and 2.5 m). Figure 4-6 shows the relationship between fractional scattered flux (from 315 nm to 570 nm) and position along the fiber for the 2.0 % wt. SiO_2-clad optical fiber. The graphic illustrates a logarithmic decay in scattered light along the optical fiber. This observation is consistent with the Beer-Lambert law represented in Eq. (2) for every wavelength with a total decrease in scattering intensity of 46 % ± 4.3 % from optical fiber position 0.0 m to 2.5

m. This even decrease throughout the UV-A and visible ranges indicates that the silica core did not significantly absorb more UV-A than visible light when compared to the polymer cladding and coating. Most of the photons in the UV-A region are absorbed by the polymer cladding and coating before they are measured as I_S.

Functionalization Effect on Attenuation

To investigate the total loss through each optical fiber, the attenuation through the optical fiber was measured by the cutback method. Figure 4-7 illustrates the effect of scattering center functionalization on the total attenuation. Light attenuation through the fiber is due to (i) absorption by the glass fiber or polymer cladding/coating, (ii) inherent scattering losses (Raleigh), and (iii) introduced Mie scattering due to silica loading onto the optical fibers' cladding. Increased attenuation also decreases the useful length of optical fiber, where I_T/I_0 > 90%. The left axis of Figure 4-7 represents the respective length for which 90% of the inlet light would be lost either due to scattering or absorbance of photons.

The neat-clad fiber shows attenuation below the limit of detection ($\frac{I_T}{I_0} > 0.99$) for the 3 m cutback length of the fiber. Addition of 0.5 % wt. or 1.0 % wt. SiO_2-clad optical fibers increased the total attenuation by 0.3 and 0.7 dB/m, respectively, in the visible range. The silica spheres likely disturbed the photon path along the fiber increasing loses due to Mie scattering. Addition of 2.0 % wt. silica did not further increase attenuation as the photon disturbance at the core/cladding interface reached a maximum.

Absorption of UV Scattered Light

Whereas visible light scattering uniformly increased with silica sphere addition, a different pattern was observed for UV-A wavelengths (i.e., < 400 nm). The neat-clad fiber fractional scattered flux increased with decreasing wavelength (Figure 4-5) for $\lambda >$ 385 nm following Rayleigh scattering trend (previously described). For $\lambda <$ 385 nm, a decreased trend of fractional scattered flux is illustrated for decreasing wavelength. This trend is a result of increased UV absorption by the polymer cladding and coating. Figure 4-5 and Figure 4-7 show exponential decrease in scattering and increase in attenuation, respectively, for $\lambda <$ 400 nm light with and without addition of silica spheres. These results are due to absorbance by both the silica core and polymer cladding/coating. Therefore, to fabricate optical fibers that scatter light < 400 nm, UV-light transparent polymers would be needed.

Conclusion

There is growing interest in obtaining tunable light scattering in optical fibers. This work illustrated that loading optical fiber cladding with scattering centers was an effective method to increase the scattered flux ratio in optical fibers by 9.7 to 30.3 X in the UV-A range and > 95.2 X in the visible range. This allows light to exit the fibers for a wide variety of potential applications. Existing optical fiber fabrication infrastructure can be used to produce evenly-distributed scattering centers within the optical fiber polymer cladding. In contrast to prior research that used dip-coating methodologies, this work used an in-line full-scale scalable facility to coat the fibers with a blend of tunable loading of spherical silica scattering centers with polymer cladding. Higher concentrations of these silica particles led to higher scattering flux ratio due to increased photon-particle interaction. The scattering flux was dominated by Rayleigh scattering for the bare optical fiber and Mie scattering for the optical fibers modified with silica spheres.

The increased absorption by the polymer cladding and coating with shorter wavelengths limits the scattering emission of UV-A light from these optical fibers. Replacing the materials with UV-transparent polymers and silica core would allow for higher scattering then what was obtained in this study by decreasing loss (absorption) within the fiber. Further developments to scatter UVB and UV-C wavelength ranges (254–365 nm) will allow these fibers to be used in water treatment applications where there is a clear need for new methods of light distribution (Santoro et a., 2017). We are conducting additional research to fabricate UV-scattering optical fibers and couple them with UV-LEDs to increase energy efficiency in applications such as UV disinfection (UV-C range) and oxidation of organics (UV-A range).

Acknowledgements

This work was performed under the auspices of the U.S. Department of Energy by Lawrence Livermore National Laboratory under Contract DE-AC52-07NA27344 and was supported by the LLNL-LDRD Program under Project No. 17-FS-02. Additional support was provided by the National Science Foundation (NSF) through the Nanotechnology-Enabled Water Treatment Nanosystems Engineering Research Center (EEC-1449500) and the Interdisciplinary Graduate Educational Research Traineeship: Solar Utilization Network fellowship (DGE-1144616).

Figures

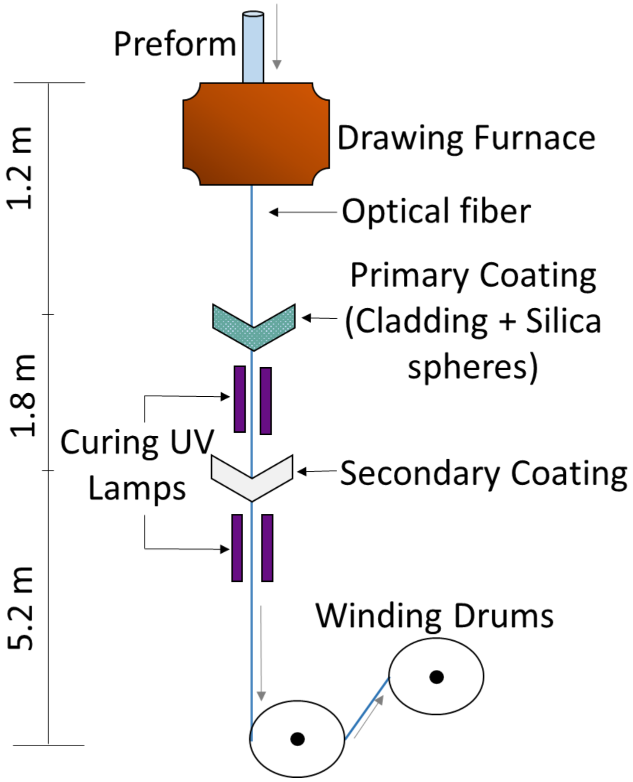

Figure 4-1 Schematic of tower used to fabricate the modified optical fiber and control the silica addition into the cladding.

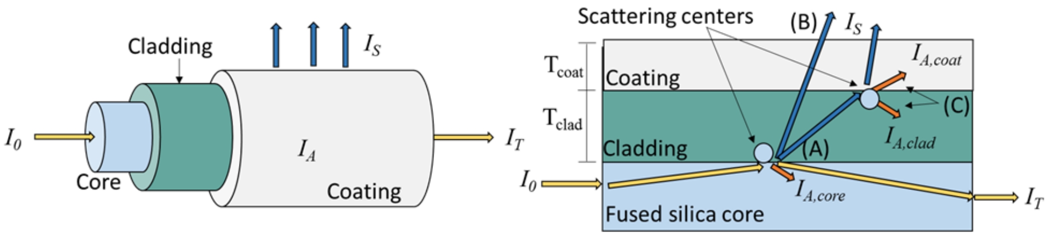

Figure 4-2 Schematic of the light transmission, scattering, and absorption through a single unmodified optical fiber (left) and after addition of scattering centers on optical fiber cladding (right).

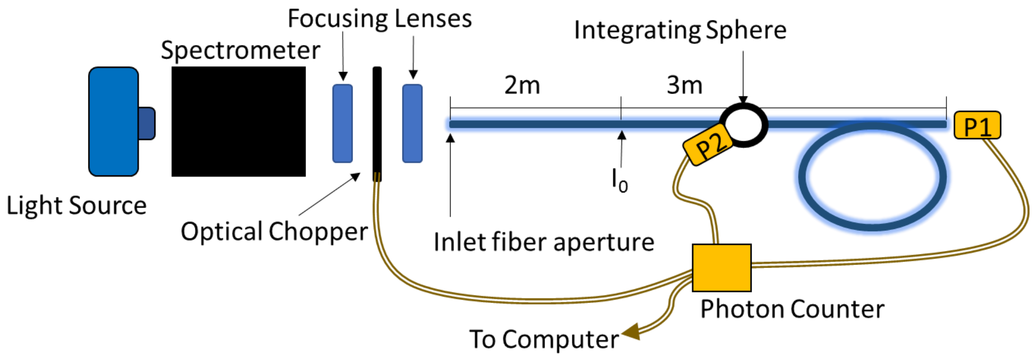

Figure 4-3 Optical setup for light attenuation and scattering analysis. P1 and P2 represent the sensor positions 1 and 2, respectively.

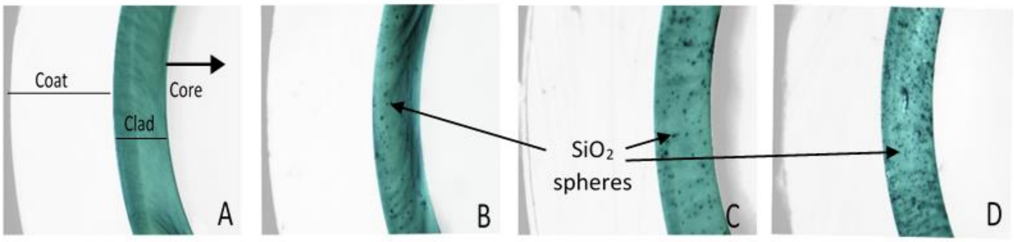

Figure 4-4 Optical microscope images at 40X magnification of optical fibers with 500-nm silica sphere loadings of: (A) neat-clad, (B) 0.5 % wt. SiO_2-clad, (C) 1.0 % wt. SiO_2-clad, (D) 2.0 % wt. SiO_2-clad. Silica spheres are illustrated as black dots on clad.

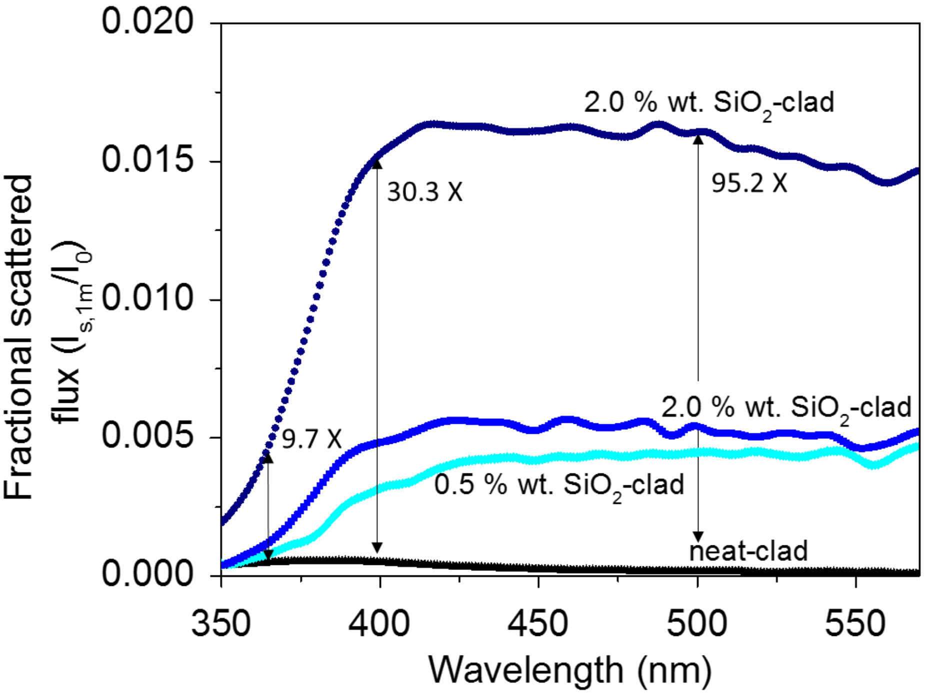

Figure 4-5 Effect of optical fiber clad functionalization on the fractional scattered flux at 1 m position ($I_{s,1m}$) for deuterium lamp source input (I_0) emitting light with wavelengths between 350 and 570 nm. Values right of double sided arrows represent increase in scattering from the unmodified fiber to the 2.0 % wt. SiO_2-clad for λ= 265 nm, 400 nm, and 500 nm.

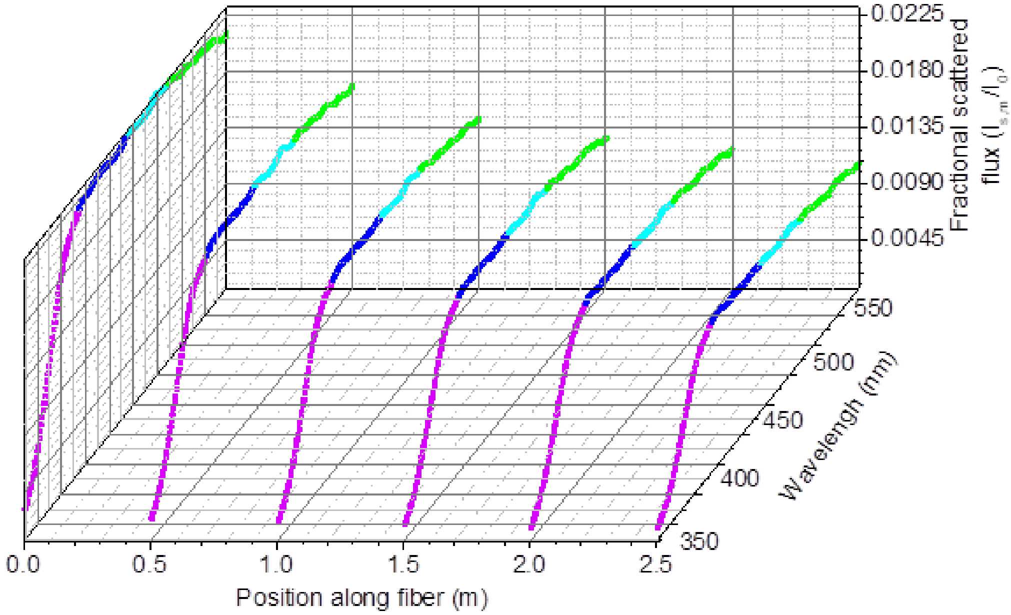

Figure 4-6 Logarithmic reduction in scattered flux along the length (position 0 to 2.5 m) of the 2.0 % wt. SiO_2 optical fiber. Purple lines represent UV-A wavelengths. Blue and green lines represent visible wavelengths.

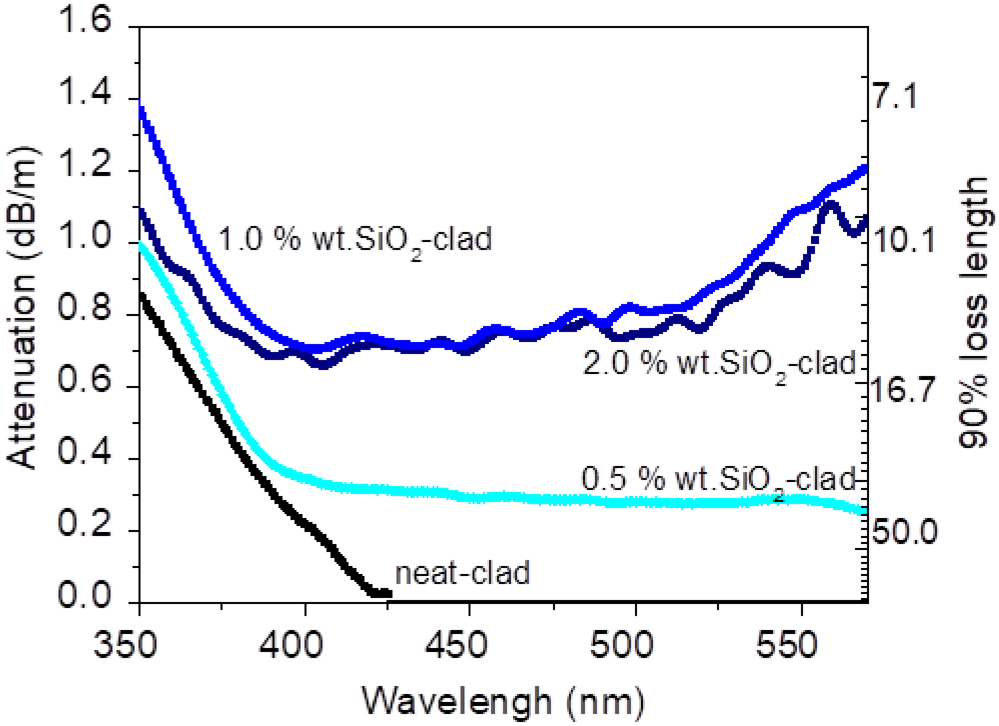

Figure 4-7 Effect of optical fiber clad functionalization with SiO2 spheres on the attenuation of light through the optical fiber for λ = 350–570 nm.

Supplemental Information

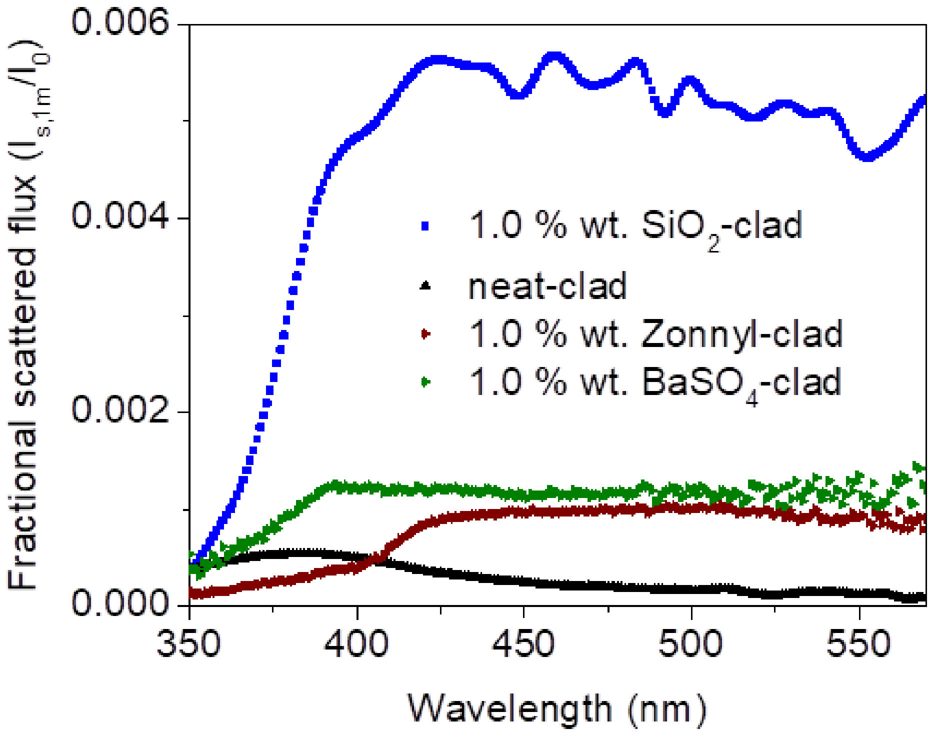

Figure S.I. 4- 1 Effect of material type on the fractional scattered flux at 1 m position ($I_{s,1m}$) for deuterium lamp source input (I_0) emitting light with wavelengths between 350 and 570 nm.

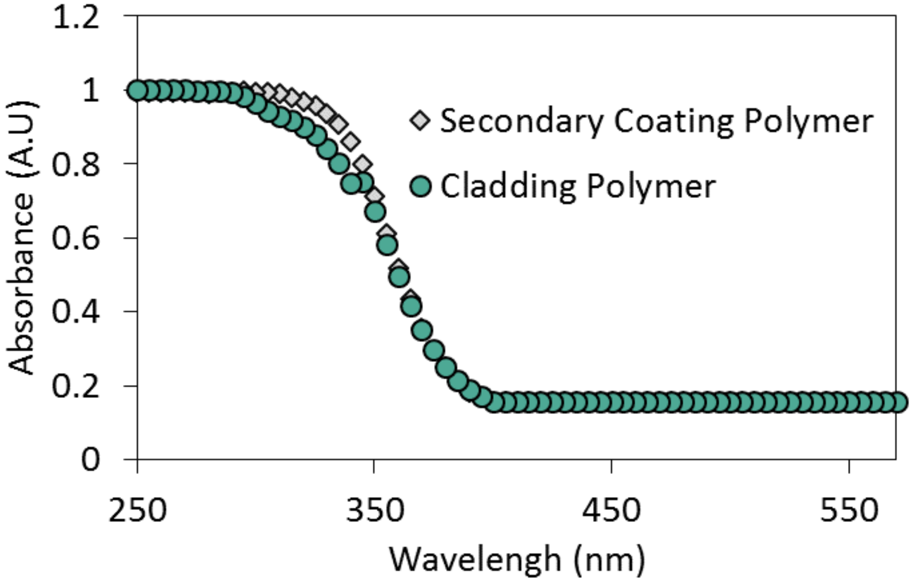

Figure S.I. 4-2 Absorption spectra of cladding polymer (DeSolite DF-0016 (cladding material) and the secondary coating polymer (DeSolite DS-2015) for wavelengths from 350 nm to 570 nm.

CHAPTER 5

NANOPARTICLE AND TRANSPARENT POLYMER COATINGS ENABLE UV-C SIDE-EMISSION OPTICAL FIBERS FOR INACTIVATION OF ESCHERICHIA COLI IN WATER

Text from: Lanzarini-Lopes, M., Cruz, B., Garcia-Segura, S., Alum, A., Abbaszadegan, M., Westerhoff, P. Nanoparticle and transparent polymer coatings enable UV-C side-emission optical fibers for microbial inactivation in water. *Environmental Science and Technology*, 53(18), pp. 10880-10887. Figures included at the end of the chapter.

Abstract

Pathogenic bacteria pose a health threat and operational challenges in drinking water. UV-C light emitting diodes (UV-C LEDs) are becoming a competitive disinfection technology but are limited by their small irradiation area. Side-emitting optical fibers (SEOFs) can serve as a UV-C LED light delivery technology for reactors or tubing. Modifying the surfaces of conventional optical fibers with scattering centers allows for side emission of 265 nm radiation from an LED for microbial inactivation in water. Solid-material absorbance and flux measurements differentiated light absorption from scattering for all materials. Silica spheres > 200 nm in diameter achieved higher scattering than smaller silica. A critical discovery was that treating the silica coated optical fiber in a solution of high ionic strength increased UV-C side emission by greater than six-fold. Additionally, the cladding polymer Cytop^{TM} had negligible absorbance at 265 nm wavelength. A scalable four-step treatment process was developed to fabricate the novel SEOF. Attached to a 265 nm LED, the side-emitting optical fiber achieved 2.9 log inactivation of *E. coli* at a delivery dose of 14.5 mJ/cm^2. The results illustrate proof of

concept that UV-C SEOFs can inactivate *Escherichia coli* and should be further explored for delivering LED light into water.

Introduction

Chemical oxidants produce potentially harmful disinfection by-products (DBPs) in the presence of precursors (e.g. NOM, bromine) and require on-site storage or production from liquid or gaseous feedstocks (An et al., 2019; Nieuwenhuijsen et al., 2000). Germicidal irradiation using light between 250 and 280 nm wavelengths (UV-C) does not produce DBPs and requires only electrical power. Low- and medium-pressure mercury lamps encased in quartz tubes are the most widely used UV-C light sources for water treatment (Schalk et al., 2005). Multiple quartz tubes are usually installed in pipes or basins at water and wastewater treatment plants and disinfect water with less than one minute of contact time. Low-pressure mercury lamps are also employed in point-of-use, portable and industrial water purification systems. However, light emitting diodes (LEDs) are becoming a competitive and lower cost alternative with promising characteristics for water treatment (e.g., lack of warm up time, tunable radiation, no degradation from on/off cycles and longer life of use) (Autin et al., 2013; Beck et al., 2017; J. Chen et al., 2017; Matafonova & Batoev, 2018). A crucial technology barrier of LEDs for disinfection is their small surface area that emits irradiation which will necessitate arrays of many LEDs in even the smallest reactors (Chen et al., 2017; Martín-Sómer et al., 2017; Oguma et al., 2013; Song et al., 2016).

Additionally, it is impractical to use LED arrays or large quartz lamps in certain reactor geometries or other tight spaces where biofilms can grow (e.g., tubing, storage tanks/bladders, spiral-wound membranes and others). Thus, there is a need to distribute light from LEDs for microbial disinfection within reactors and for use in tight spaces to prevent biofilm formation. In these applications, optical fiber can be used as the light delivery medium.

Conventional optical fibers are long, thin glass tubes that can efficiently transmit light over many kilometers. Optical fibers usually have a circular core made of glass or polymer that is then encased by one or more coatings termed cladding and secondary coating (Figure 5-1). Traditional, end emitting optical fibers propagate light axially (transmission) due to complete internal reflection from the lower refractive index cladding surrounding the higher refractive index core (Agrawal, 2010; Mitschke, 2009). Thin glass fibers can be remarkably flexible, but scratches or other damage initiate mechanical failure. The external secondary polymeric coatings protect the glass from breaking when bent. In some applications, only one layer is applied, serving as both the cladding and coating. Commercial-scale optical fiber production is conducted in multi-story drop towers, where glass is melted, molded and coated through a series of in-line rollers, polymer paths and heating or curing chambers (Lanzarini-Lopes et al., 2019). This produces optical fibers up to kilometer lengths.

Side emitting optical fibers deviate from traditional light guides used in telecommunications and laser applications where scattering outside the fiber is undesirable. Methods of obtaining side emission in fibers include (i) optical fiber core modifications (e.g., doped with phosphors), (ii) cladding material of differing refractive indices and optical properties from the fiber core or (iii) addition of imperfections or etching of coating and cladding material (Arie et al., 1986; Rawson, 1974; Rawson, 1972). The result is side-, or “glowsick” like, emission of visible light along the length of the optical fiber. These fibers have been fabricated in the visible wavelengths and are currently commercially used for decorative applications in lengths of 1 to 10 m (e.g., Corning®, Fibrance® Light Diffusing Fiber) (Patent No. WO2014121172A2, 2017). Shorter wavelength side-emitting optical fibers are used for photodynamic therapy in medical applications. Here, a very short section (< 1 cm) of cladding is removed, and imperfections in the glass fiber core induce scattering (Klubben et al., 2016). The wavelength of interest impacts the choice of core, cladding, coating and particle used as scattering material in the optical fiber. They have been previously explored for visible and UV-A water treatment applications by attaching photocatalytic materials directly to the optical fiber core(Ling et al., 2017; Nicola J. Peill & Hoffmann, 1995).

A barrier to emitting UV-C radiation from the side of the optical fibers is the absorption of light by the core and coating of the fiber (Lanzarini-Lopes et al., 2019) that results in inefficiencies. This absorption exponentially increases with decreasing wavelength due to electronic resonances form unbound electrons (Fujino, 2005; Jeanmonod et al., 2011). Currently there are no reported means of modifying optical fibers to allow side-emission of UV-C light. However, such capabilities would enable delivery of UV-C light for microbial inactivation in water treatment reactors with unique geometries.

The objective of this study was to select and optimize the attachment of scattering center nanoparticles on the surface of glass optical fiber cores. The scattering centers induce side-emission of UV-C light generated by a 265 nm LED and thus can inactivate *E. coli* in water. A scalable four-step treatment process was developed to fabricate the novel optical fiber. A crucial step was selecting a UV-C transparent polymer cladding to minimize absorption of UV-C radiation by the fiber itself. Solid-material absorbance, radiometer and chemical actinometry measurements were used to quantify adsorption versus scattering and to parameterize a design model for optical fibers. The paper concludes with a discussion of future steps to scale production to meter-lengths of the UV-C side-emitting optical fibers and discuss their insertion into unique geometries for pathogen and biofilm control.

Fabrication and Experimental Methods

Fabrication of UV-C side-emitting optical fibers

Multimode, UV-transmitting optical fibers of 1 mm diameter, numerical aperture of 0.39 and core refractive index (RI) of 1.46 were purchased from Thorlabs, Newton, NJ USA (FT10000UMT). These hard fluoropolymer clad silica fibers where chosen due to their low UV absorption by the silica core and ability to remove the coating and cladding. A four-step fiber preparation methodology was developed (Figure 5-1).

Step 1 involved stripping the coating and cladding on the commercial fiber using an aluminum razor and soaking the fiber in acetone (99.5 %) at room temperature for 25 minutes to dissolve any remaining cladding. Note that this step would not be required during commercial fabrication. The optical fiber was cut with a ceramic blade into 8.5 cm segments for the test fibers and 3.5 cm segments for the reference fibers. The clean fibers were individually attached to 3.0 cm ferrule connectors (SMO5SMA, Thorlabs) using 1/16” and 3/32” heat shrink tube (Gardner Bender, New Berlin, WI USA, HST- 125), leaving 5.0 cm or 0 cm of exposed optical fiber after polishing. The ferrule connector is a snug hollow tube with a threaded body that allows the optical fiber to be screwed into the polishing and optical set up. The fiber was mounted on a fiber support (D50SMA, Thorlabs) and polished using optical polishing paper (LF30P, LF5P and LF03P) to obtain a smooth surface on each circular face as previously described (O'Neal Tugaoen et al., 2018).

Step 2 involved dip-coating nanoparticle scattering centers onto the cleaned fiber core. Aminated silica spheres (d = 50 nm, 100 nm, 200 nm, 400 nm and 500 nm) suspended in ethanol (99.99 %) at room temperature (nanoComposix, San Diego, CA USA, 10 mg/mL, SIAN*d*-25M) where selected for two primary reasons. First, silica has low absorption in the UV range. Second, positively charged aminated spheres enable electrostatic attachment to negatively charged glass core. Each particle size was separately dip-coated onto different stripped optical fibers. Dip-coating involved submerging the fiber with tweezers into the aminated silica spheres suspension for 60 seconds and then allowing the fiber to air dry for 5 minutes. Dip-coating was repeated up to 7 times to deposit different masses of the silica scattering centers on the fiber. Gravimetric measurements (Sartorius M2P, Wood Dale, IL USA, tolerance = 0.01 mg) of non-coated and coated fibers determined the mass coverage ($\mu g/cm^2$) of spheres on the fiber.

Step 3 involved submerging the coated fiber in variable aqueous ionic strength solutions (0 to 1 M) of sodium sulfate (Na_2SO_4) (Sigma-Aldrich, St. Louis, MO USA, 239313) for 10 seconds at room temperature to increase contact between the silica nanoparticles and optical fiber core. The fiber was allowed to air dry for 5 minutes.

Step 4 involved dip-coating with a polymer at a rate of 1 cm/s. Three polymers were used: (i) fluoropolymer (Cytop^{TM}), (ii) poly(methyl-methacrylate) (PMMA) and (iii) a common optical fiber polymer (DeSolite). Cytop^{TM} was purchased as a polymer from BELLEX International Corp, Wilmington, DE USA (CTX 109AE, RI: 1.34), dissolved in a non-disclosed perfluoro-compound at 9 wt %. PMMA powder (81489, RI: 1.48) was purchased from Sigma-Aldrich and dissolved in toluene (Sigma-Aldrich, 244511) at 9 wt %, 80 °C and 500 rpm. DeSolite® (DF-0016, RI: 1.370) was obtained from Desotech Inc., Elgin, IL USA, as a liquid monomer and polymerized under UV 365 nm after dip-coating. Solid Analysis of the optical fiber surface after each step was obtained by scanning electron microscopy with elemental mapping (SEM/EDX) (Philips XL30-EDAX) with gold and palladium sputtering.

Fabrication of LED-optical fiber device

All optical fiber mounting parts were purchased from Thorlabs. A 30 mm cage system secured by four 8” stainless steel rods (ER8) was used to secure and align all optical components. The 12 mW 265 nm UV-C LED (Boston Electronics, Brookline, MA USA, VPC131) had a measured peak of 267 nm with a spectral width of 30 nm. The LED was secured by a cylindrical lens mount (CYCP), followed by three 1” calcium fluoride uncoated plano-convex lens (LA5370), positioned by kinematic plates (KC1-T). The lenses maximized the light coupling into the optical fiber by capturing, coning and focusing the light onto the optical fiber terminal end. Finally, the polished optical fiber was secured by fiber adapter.

Light measurements

Localized scattering flux. Localized UV-C emission from the optical fibers was assessed by scattering flux measurements using a spectrophotoradiometer (Avantes, Louisville, CO USA, AvaSpec-2048L, calibration: 200 – 1100 nm). The sensor tip of the spectrophotoradiometer (5 mm^2) was placed normal and flush to the center of the optical fiber (2.5 cm from the ferrule connector) as illustrated in Figure 5-1. Only photons that are side emitted are captured by the sensor, and the flux was obtained by integrating the output spectrum.

Total scattering. Photons that are coupled into the optical fiber (I_0) can be transmitted (I_t) through the optical fiber core by internal reflection, absorbed (I_a) by the core or cladding materials, or side emitted (I_s) by scattering of the optical fiber as illustrated in Eq 1 (See S.I. Figure 5-1).

$$I_0 = I_t + I_a + I_s \tag{1}$$

In this study, increasing the fraction of photons side emitted from the optical fiber is beneficial for use in disinfection and is described as scattering ratio (I_s/I_0). Both I_0 (photons/s) and I_s (photons/s) were quantified by potassium ferrioxalate actinometry experiments in the dark. All substances used in the actinometry experiments were purchased from Sigma-Aldrich. The potassium ferrioxalate solution was prepared as previously described (Autin et al., 2013; Bolton, et al., 2011; Hatchard & Parker, 1956). The reference (I_0) and test (I_s) optical fiber coupled to the UV-LED 265 were submerged in the 200 mL actinometry solution (S.I. Figure 5-2). To measure the total scattering from the test fibers, a black rubber casing encompassed the distal submerged terminal end of the fiber and served as a photon sink for any light transmitted through the fiber.

Chemical actinometry. The light side emitted from the fiber photoreduces potassium ferrioxalate, releasing Fe(II). To prevent the Fe(II) from re-oxidizing to Fe(III), the solution was continuously purged with nitrogen gas. The experiment was conducted at room temperature (~22 °C). A 2 mL sample was obtained from the solution at 0, 15 and 30 minutes, individually mixed with 1,10-phenanthroline, and left standing for 30 minutes. The concentration of the Fe(II)-phenanthroline red-colored complex was measured by change in absorption at 510 nm using a UV-VIS spectrometer (HACH DR5000, Loveland, CO USA). A control sample assured no external light reached the actinometry solution. Finally, the quantum yield of the photoreduction of potassium ferrioxalate ($\Phi_{260 < \lambda < 300 \text{ nm}} = 1.25$) (Goldstein & Rabani, 2008; Hatchard & Parker, 1956) was used to calculate the photons side emitted by the test optical fiber (I_s), transmitted by the test optical fiber (I_t) or transmitted by the reference optical fiber (I_0).

Microbial inactivation

Culture preparation. The pure *Escherichia coli (E. coli)* culture was originally obtained from the American Type Culture Collection (ATCC® 25922™, Manassas, Virginia USA). An inoculum from a frozen glycerol *E. coli* stock (kept at -80 °C) was streaked onto a fresh tryptic soy agar (TSA) plate and incubated overnight at 37±1 °C. A single colony from the plate was recovered and inoculated into 5 mL of tryptic soy broth (TSB) and incubated overnight at 37±1 °C to start a liquid culture. The overnight TSB culture was diluted to a desired concentration and used for experiments. The absorbance spectra of the *E. coli* solution peaked at 268 nm, which coincides with the output LED spectra.

UV exposure of *E. coli* culture. The overnight culture of *E. coli* was diluted to approximately 5 x 10^6 colony forming unit (CFU) per mL using 10-fold dilution with phosphate buffered saline (PBS). The 0.5X PBS consisted of NaCl (0.0684 molarity), KCl (0.00134 molarity), Na_2HPO_4 (0.005 molarity), KH_2PO_4 (0.0009 molarity) with the final pH 7.4. A 5 mL aliquot of the diluted culture was transferred to a round bottom polypropylene tube (12 x 74 mm) covered with aluminum foil. The 5 cm UV-C SEOF was completely submerged in the center of the tube resulting in 5.5 mm absorbance pathlength. *E. coli* culture was exposed to UV-C for 15, 30 and 60 minutes to illustrate a linear trend in inactivation over an hour of exposure. A control sample with no UV-C exposure was analyzed for each time to account for any photoreactivation mechanism from the treatment or enumeration environment. After each exposure time, duplicate samples were analyzed to quantify viable *E. coli* using the standard pour plate method. *E.* coli colonies were counted using Reichert Darkfield Quebec Colony Counter for plates containing 30-300 CFU/ml). Triplicates were obtained using different optical fibers.

E. coli UV dose correction. The potassium ferrioxalate actinometry (explained above) measures how much light emitted from the optical fiber is absorbed by the ferrioxalate solution specifically. To correct for dose absorbed by the E. coli solution, the 265 nm light transmitted (UVT265) by the E. coli (75.5 %) and potassium ferrioxalate (2%) solutions were measured by a UV-VIS spectrometer for the 5.5 mm pathlength. A correction factor (CF) of 0.25 was calculated by dividing the fraction of light absorbed (UV-A = 1-UVT) by the E. coli solution (24.5%) by that of the actinometry solution (98.0%). The dose measured by actinometry is multiplied by CF to obtain the E. coli UV dose.

Pour plate method. TSA medium was prepared according to the manufacturer instructions. Briefly, 40 g of TSA powder (Sigma-Aldrich, 22091) was dissolved in 1 L of deionized water while heating (at maximum heat) under constant mixing using a stir bar. After complete TSA dissolution, the medium was autoclaved at 121 ºC for 15 minutes. The autoclaved medium was kept in a water bath set at 48±2 ºC.

The *E. coli* cultures exposed to UV-C were serially diluted (10-fold dilution) using 1X PBS. All dilutions were analyzed in duplicate. Briefly, 1 mL of each dilution was added to a sterile petri dish, followed by addition of 15 mL of liquified TSA medium acclimatized at 48±2 ºC. The plates were quickly swirled to thoroughly mix the liquid TSA with the sample and then left undisturbed in a biosafety hood for 30 minutes or until medium was completely solidified. The plates were incubated at 37±1 ºC for 48 h, and data was recorded as colony forming units (cfu) per mL. Disinfection efficacy of the coated, side-scattering fiber optic probe for each contact time was calculated using the mean log reduction (LR) for *E. coli*.

Material characterization

A UV-VIS spectrophotometer (PerkinElmer, LAMBDA 950 UV/VIS, Waltham, MA USA) equipped with a Spectralon® surface (Labsphere, North Sutton, NH USA) integrating sphere was used to measure the absorption of the materials used in this study. The absorbance (A) of the aminated silica spheres was obtained by diffuse reflective spectroscopy (DRS) and corrected using the Kubelka-Munk equation (Nobbs, 1985). A 1” x 1” quartz substrate (Ted Pella Inc, 26012) was prepared by dripping 300 µL of 99.99 % ethanol-suspended aminated silica on the substrate and letting it dry at room temperature for 30 minutes. This resulted in 4.65 (± 6 %) µg/mm^2 loading. The cycle was repeated 10 times, until the sample was visually opaque. The sample was then placed in the back of the integrating sphere so that any scattering/reflection was measured as T. For the polymer absorption measurements, quartz substrates were prepared by dip-coating at 1 cm/s (same rate as the fiber preparation). The sample was placed in front of the integrating sphere. Transmission measurements were obtained at 265 nm and reported as absorbance, where $A = 1 - T$, assuming insignificant reflection/scattering. There was no noticeable difference in transmission through the spectral output of the LED. Thicknesses was measured by a stylus profilometer (Bruker XT) and was 5–20 μm. Absorption was adjusted to 5 μm per the Beer-Lambert law.

Results and Discussion

Two factors that influence scattering flux of UV-C through the optical fiber length were explored: (i) extinction (absorption and scattering) over the cross-sectional area of the material being used as a scattering center and (ii) loading of scattering centers, which influences how many particles interact with photons. The interactions between photon and scattering centers are possible via two means: (i) light refracting from the quartz fiber waveguide at contact point between the scattering center and optical fiber core or (ii) interaction of particles with the evanescent wave. Evanescent waves are the electromagnetic disturbance formed by total internal reflection at the interface of the transmitted medium. The wave amplitude decays exponentially with the distance from the interface (Ling et al., 2017; Prieve & Walz, 2009). Designing the scattering center materials and loading led to maximum utilization (i.e., side emission) of LED light entering the optical fiber, which enabled microbial disinfection. Each of these factors are described below.

Selecting low UV-C absorbing scattering centers

A particle’s extinction coefficient is a measure of the amount of light removed from a beam that comes in contact with it normalized by the geometric cross-sectional area of the particle that is normal to the beam (Oldenburg, 1999). Here, the light removed from the beam by the particle is either absorbed (absorption cross-sectional area) or scattered (scattering cross-sectional area) (Bohren et al., 1956). For side-emission of light from optical fibers, it is important to select particles with low absorption and high scattering of

UV-C. The theoretical scattering and absorption cross-sectional area of gold, silver and silica were predicted based on Oldenburg's Mie theory (Oldenburg, 1999). Silica spheres were selected as the scattering centers for the UV side-emitting optical fibers due to significantly higher scattering cross-sectional area than absorption cross-sectional area, regardless of the particle size (S.I. Figure 5-3).

Figure 5-2 shows the absorbance at 265 nm of silica spheres between 50 nm and 500 nm. The absorbance of the aminated silica spheres deposited on a quartz substrate was obtained by diffuse reflective spectroscopy (DRS) and corrected using the Kubelka-Munk equation (Nobbs, 1985). During DRS, light cannot be transmitted and is therefore either absorbed or detected by scattering/reflection. Smaller particles (50 nm diameter) absorb more and scatter less 265 nm light than larger silica spheres (> 200 nm diameter), which absorb very little light and instead scatter it (Figure 5-2 inset) (Oldenburg, 1999). This result is explained by Mie theory where I_A/I_S increases with decreasing diameter because the particle scattering cross-sectional area decreases in proportion to its volume for $d \lesssim \lambda$ (Bohren & Huffman, 2007; Van De Hulst, 1957). These measurements suggest larger diameter silica spheres should lead to our preferred outcome of scattering, rather than absorbing, 265 nm light if placed on the glass fiber core.

Maximizing UV-C scattering from the optical fiber by varying silica sphere diameter and loading

The diameter of silica used as scattering center affected the scattering cross-sectional area (illustrated above) as well as the amount of interactions that result in light scattering. Steps 1 and 2 of the fabrication process were followed with each diameter silica sphere. Smaller silica spheres have higher interfacial contact with the optical fiber core. Higher silica sphere loading can also contribute to increased scattering until it plateaus. Figure 5-3 shows the measured scattered light half way down the optical fiber (2.5 cm) after coating the fiber with variable mass loadings (0 to 3 $\mu g/mm^2$) of different diameter silica spheres (50, 100, 200, 400 and 500 nm).

Particle loading was varied by the number of dip-coating cycles. Each dipping cycle resulted in ($0.41\ \mu g/mm^2 \pm 6\%$) additional loading for all the sizes. Electron microscopy images confirmed continuous layers of silica spheres on the surface of the optical fibers (S.I. Figure 5-4). For the 400 nm and 500 nm silica, higher loading results in higher scattering. As expected, a plateau in scattering was reached for every size. Further increasing the loading of silica spheres onto the fiber would not result in increased scattering.

Particles diameters of 200 nm or above achieved similar scattering according to the student t-test with 95% confidence level ($4.4\ \mu W/cm^2$; $p > 0.10$), with slightly more scattering than 100 nm diameter particles ($3.4\ \mu W/cm^2$; $p = 0.023$), and more than five-fold higher scattering than 50 nm spheres. To obtain effective UV-C side emission from optical fibers, spheres > 200 nm should be selected. Subsequent results are presented for 400 nm diameter aminated silica spheres; select experiments with other diameters yielded comparable findings (not shown).

High ionic strength treatment increases side-emission of UV-C light

The benefits on enhanced side-emission of light associated with a post-treatment step using a high ionic strength solution (Step 3) were realized by serendipity. While developing the method, Step 2 was performed at different pH levels to investigate electrostatic interactions between the aminated silica spheres and glass fiber core. The scattering significantly increased at lower pH. Similar results occurred using sulfuric or hydrochloric acid. Subsequent experiments using high molarity sodium sulfate solutions demonstrated the improved scattering was due to higher ionic strength, and results depended less on pH. Figure 5-4 shows representative data, with increasing scattering half way down the optical fiber for different ionic strength solutions using 400 nm silica spheres. For treatment with ionic strength > 0.45 M (0.2 M Na_2SO_4), the scattered flux reached greater than six-fold higher than without Step 3. To verify that the cause of increased scattering was due to ionic strength, the same experiment was conducted with Na_2PO_4, normalizing for ionic strength. The scattering increase results are within the standard deviation for Na_2SO_4. Thus, subsequent fibers were prepared using 0.2 M Na_2SO_4 in Step 3.

Three causes were speculated for the increase in scattering after high ionic strength treatment. First, salt precipitate on the surface of the optical fiber could create additional areas of uniformity. However, neither sodium nor sulfur were present on the optical fiber surface when examined using scanning electron microscopy (SEM) with elemental mapping. Second, high ionic strength could cause the particles to rearrange and form a more uniform monolayer. However, SEM images of the fiber surface did not illustrate a significant change in arrangement pre and post high ionic strength treatment. Third, high ionic strength treatment likely compressed the electric double layer around the aminated spheres, packing them closer to the surface. The third explanation was probably the reason behind enhanced side-emitting light (Figure 5-4). Previous theoretical and experimental work illustrates that the intensity of scattered light is also a function of the separation distance between the particle and the interface (Chew et al., 2008; Prieve &

Walz, 2009). Because the evanescent wave intensity is higher closer to the fiber, there is more interaction between the photons and the scattering centers, increasing scattering. Treating the optical fiber with high ionic strength solution had a clear increase in the side-emission of UV-C light from the optical fiber. However, further work is needed to understand the effect of ionic strength on the interaction between charged particles and the optical fiber interface.

Polymer coating material effect on scattering

A technological barrier for UV-C side-emitting optical fibers is that even if the light is scattered away from the core of the optical fiber, it gets absorbed by the polymer cladding (Lanzarini-Lopes et al., 2019). Step 4 in preparing the UV-C emitting optical fiber involves selecting and applying a UV-transparent polymer cladding. The cladding served dual purposes of reflecting light within the fiber (total internal reflection) and physically protecting the fiber. High optical transmittance of the polymeric coating is essential in side emitting optical fibers because the light must go through the polymer before it can inactivate microorganisms. Three different polymers where considered: DeSolite® 0016 has been previously used in optical fiber manufacturing (Patent No. US 2002/0054744 A1, 2002; Patent No. US 2012/0321265 A1, 2012; Lanzarini-Lopes et al., 2019) ; PMMA has been repeatedly used in UV applications (Kundu & Kelly, 2018; Wang et al., 2017); and Cytop™ is a transparent fluorosis with low refractive index that reports > 95% transmittance (200 μm thickness) for UV 265 nm wavelength (“Cytop - Usage,”). Additionally, Cytop™ reports benefits due to lower index of refraction than the silica core. The polymers were deposited on a quartz substrate, and absorbance of UV 265 nm was measured using diffuse reflective spectroscopy (Figure 5-5 inset). Thicknesses of 5 μm to 20 μm was measured using a stylus profilometer, and absorption was adjusted to 5 μm per the Beer-Lambert law. PMMA and DeSolite® absorbed 11.1 % and 14.8 % of UV 265 nm, respectively. Complete transmission was observed by Cytop™, indicating null absorption of 265 nm light. Therefore, Cytop™ was selected as the polymer coating for Step 4 in the UV-C side-emitting optical fiber fabrication.

To better understand its interaction with silica spheres before and after high ionic strength treatment, the optical fiber was coated with Cytop™ after each preparation step. The localized scattering flux was measured by a spectrophotoradiometer halfway through the fiber (2.5 cm from the ferrule connector). Figure 5-5 illustrates the scattering flux of each preparation step (clean core, 400 nm SiO_2, 400 nm SiO_2 + Na_2SO_4) before and after applying Cytop™. There is a slight increase in scattering after applying Cytop™ to the clean optical fiber (1.1 $\mu W/cm^2$ ± 4 %). This is likely due to impurities in the polymer as this was not done in a clean room. There was no statistically significant difference in scattering before and after the coating was applied to the 400 nm silica coated fiber ($p = 0.31$) or the Na_2SO_4 treated fiber ($p = 0.66$). This supports the claim that Cytop™ does not affect the side emission of the optical fiber to be used in microbial inactivation.

Figure 5-5 additionally compares the effect of each preparation step (Figure 5-1, Steps 1–4) on the flux emission. The stripped fiber averaged a scattering flux of 0.2 $\mu W/cm^2$. Adding 400 nm silica spheres to the surface of the fiber core (Step 2) improved scattering 37-fold to 8.0 $\mu W/cm^2$. Treating the fiber with a solution of high ionic strength increased the localized scattering flux an additional 3.6 times to 36.9 $\mu W/cm^2$. Ionic strength treatment without silica spheres resulted in no significant increase in scattering from the clean fiber (0.23 $\mu W/cm^2$). These results illustrate the importance of each preparation step for obtaining UV-C side-emitting optical fibers. All steps were used in preparing the optical fiber for microbial inactivation.

Microbial inactivation by UV-C side-emitting optical fiber

Figure 5-6 illustrates the log inactivation of *E. coli* by coupling a UV 265 nm wavelength LED to a side-emitting optical fiber. Two optical fibers were prepared for *E. coli* inactivation. The side-emitting optical fiber (blue triangles) included all 4 preparation steps, while the control (red squares) included only Steps 1 and 4 (clean fiber coated with Cytop^{TM}) to assure the Cytop^{TM} was not contributing to inactivation of *E. coli.* The illuminated optical fiber was submersed in the 5 ml polypropylene tube filled with *E. coli* solution as described in the methods. The total photons emitted by the side of the optical fiber was measured by potassium ferrioxalate actinometry and is defined as delivery dose.

The test optical fiber achieved 2.9 log inactivation for a dose of 14.5 mJ/cm^2; this equated to one hour of operation using the low power LED. It is known that experimental set up and exposure conditions can impact the UV doses required for inactivation of different type of bacteria (Sommer et al., 2000; Tosa & Hirata, 1999; Wilson, 1992; Wu et al., 2011; Yaun et al., 2003). UV Dose of 8 mJ/cm^2 to 6 mJ/cm^2 has been reported for 3 $\log_{10}$ inactivation of washed *E. coli* (ATCC 29425) culture (Beck et al., 2017, Rattanakul & Oguma, 2018). The present study used side scattering optical fiber for inactivation of un-washed culture of *E. coli*, directly diluted in PBS. The unwashed culture of test bacteria is expected to contain greater residual organics from nutrient media, which might be responsible for the relatively higher UV dose reported in this study compared to the UV doses reported in literature for inactivation of *E. coli* (Beck et al., 2017; Rattanakul & Oguma, 2018). Additionally, reactivation of bacteria after low UV dose exposure is well documented and can lead to higher required dose for similar inactivation potential (Hijnen et al., 2006; Hu et al., 2005; Nebot et al., 2007). Here, microorganisms can recover activity through repairing pyrimidine dimers in the DNA after damage by low dose UV. Knudson quantitatively showed that reactivation can result in up to 4.6 higher UV fluence required for the same level of inactivation (Knudson, 1985).

The control optical fiber without scattering centers achieved 0.2 log inactivation for a delivery dose of 4.0 mJ/cm^2 over the same one-hour exposure. This illustrates that the Cytop^{TM} coating did not have major germicidal effect for *E. coli* (i.e., it did not damage the cells' DNA (Gayán et al., 2013)) and that the side-emitting UV-C radiation caused the inactivation. The silica sphere modified optical fiber delivered > 3.5 times the UV-C dose and obtained 16 fold higher inactivation then when only Cytop^{TM} was applied. The results illustrate proof of concept that UV-C side-emitting optical fiber can be used to inactivate *E. coli*. In this work, 25% of the radiation applied to the optical fiber was emitted through the side of the optical fiber. Higher output UV LED or better coupling of light into the optical fiber would increase the intensity of UV-C side emission.

Scaling fabrication of UV-C side-emitting optical fibers

This study illustrates a method of modifying optical fibers to side-emit UV-C radiation. Our four-step process can be adapted to large scale fabrication. In commercial scale optical fiber production, the melted, thinned and cooled glass core (Step 1) is pulled through a series of coating dies and drying ovens. For UV-C side-emitting optical fiber fabrication, the first die would contain a solution of aminated silica spheres (Step 2). The fiber would then be rolled through a high ionic strength solution before entering the final die containing Cytop^{TM} (Step 4).

One concern with UV-C side-emitting optical fibers is the logarithmic decay (Beer-Lambert law) of light through the optical fiber that could cause uneven inactivation effectiveness along the fiber length. This logarithmic decay (S.I. Figure 5-5) can be mitigated in two ways. First, the silica sphere loading or side-emitting efficiency can be modulated by either varying the loading of 400 nm silica spheres along the length of the optical fiber or by varying the length of the optical fiber exposed to high ionic strength solutions. Alternatively, light can be supplied from both ends (proximal and terminal sides) of the optical fiber using two LEDs. Future work will explore these design concepts. Additionally, coupling the optical fibers to a higher output LED will decrease retention time needed for inactivation.

Supporting Information. Schematic of photon emission, absorbance and transmission through modified optical fiber. Schematic of potassium ferrioxalate actinometry set up. Theoretical scattering and absorption cross sectional area of gold, silver and silica. SEM image of optical fiber cross section after four-step preparation. Theoretical distribution of light through the length of the four-step modified optical fiber.

Acknowledgements

The authors acknowledge David Warsinger from Purdue University for guidance in finding the Cytop^{TM} coating polymer. We thank A.J. Simon, Mike Messerly and the Lawrence Livermore National Laboratory optical fiber team for the optical fiber knowledge and previous work that led to the ideas for this study. We additionally thank Yuqiang Bi for SEM images of the optical fiber surface and Omar Alrehaili for measuring the polymer thickness. This work was partially funded by the National Science Foundation (NSF) through the Nanotechnology-Enabled Water Treatment Nanosystems Engineering Research Center (EEC-1449500), the Water and Environmental Technology (WET) Center and the Interdisciplinary Graduate Educational Research Traineeship: Solar Utilization Network fellowship (DGE-1144616). We acknowledge the use of facilities within the Eyring Materials Center at Arizona State University supported in part by NNCI-ECCS-1542160. Technical editing was provided by Laurel Passantino.

Figures

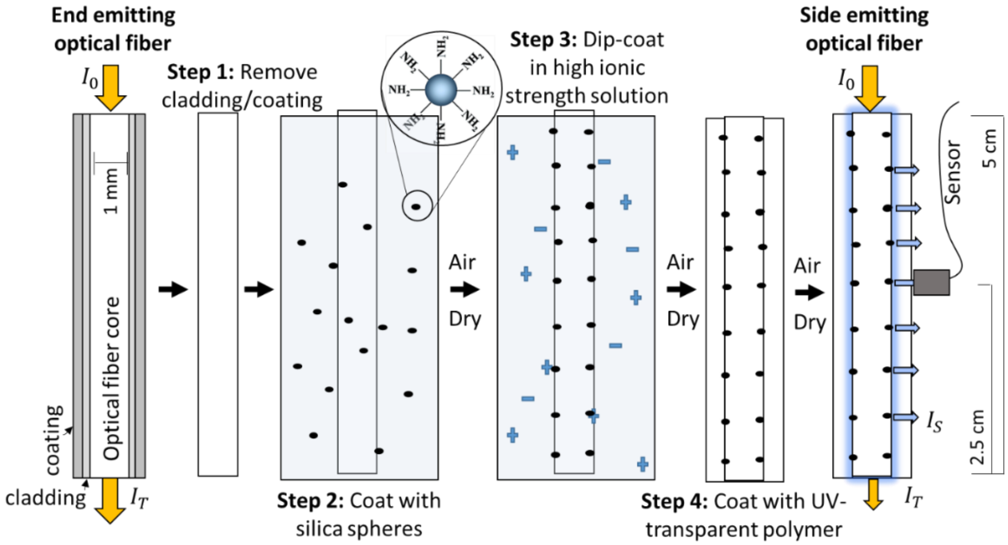

Figure 5-1 Schematic of the 4 steps used to fabricate 5 cm UV-C scattering optical fibers.

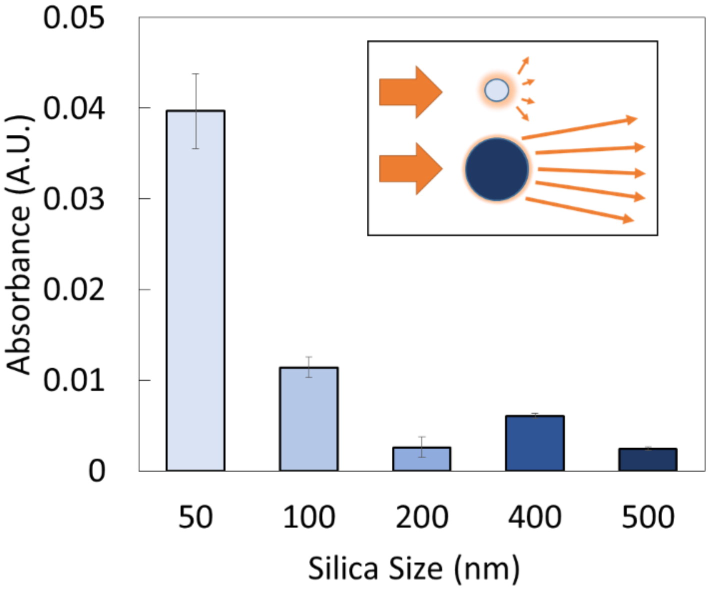

Figure 5-2 Absorbance of silica spheres of different diameters at 265 nm wavelength by diffuse reflective spectroscopy corrected by Kubelka-Munk.

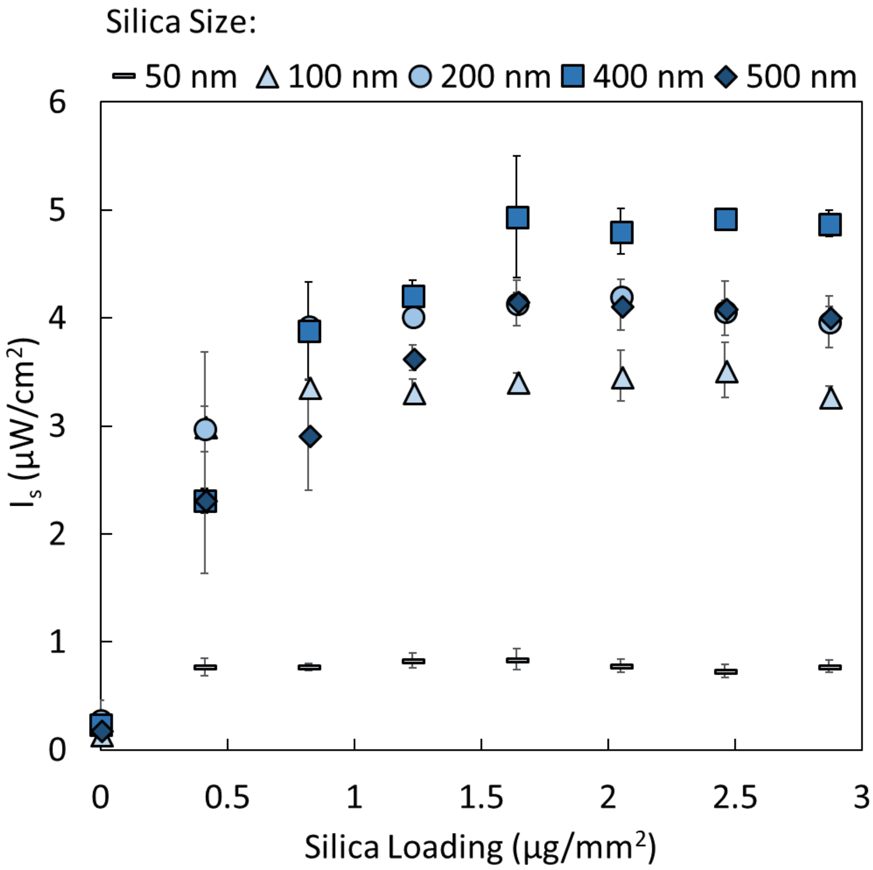

Figure 5-3 Effect of particle size and loading on 265 nm wavelength localized scattering flux.

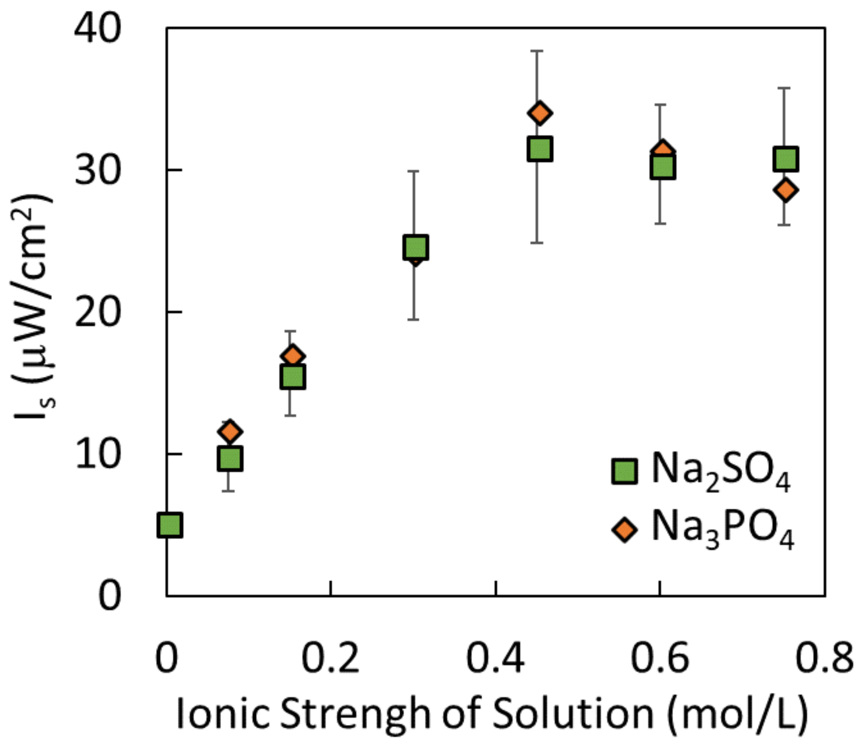

Figure 5-4 Localized scattering flux (I_s) of 265 nm for optical fiber coated with 400 nm silica increased with high ionic strength treatment.

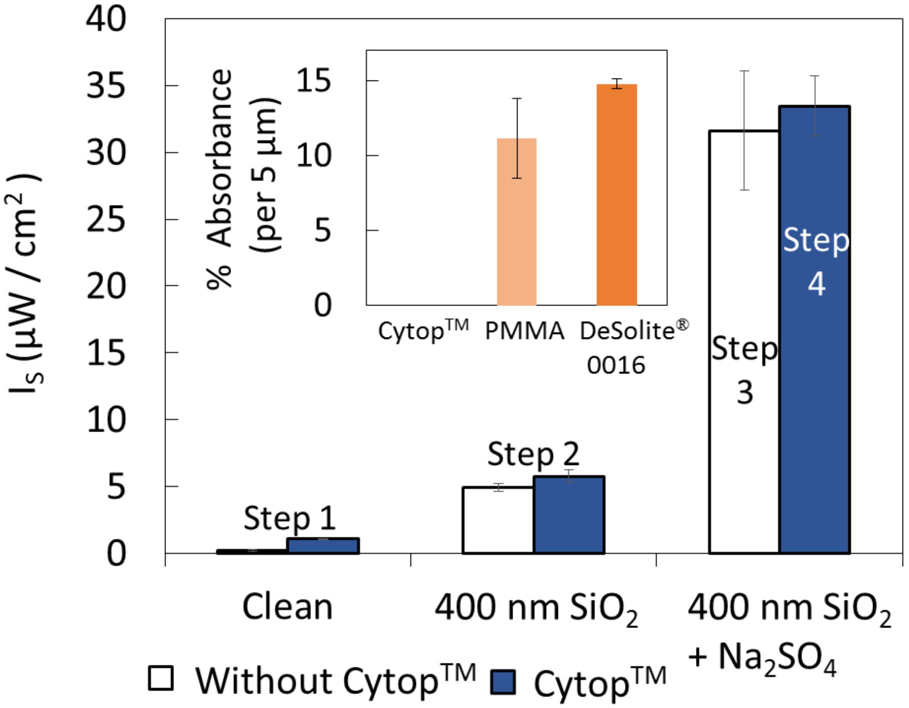

Figure 5-5 Localized scattering flux (I_S) of 265 nm for optical fiber after preparation Step 1, 2 and 3 without Cytop™ (white bars) and with Cytop™ (blue bars).

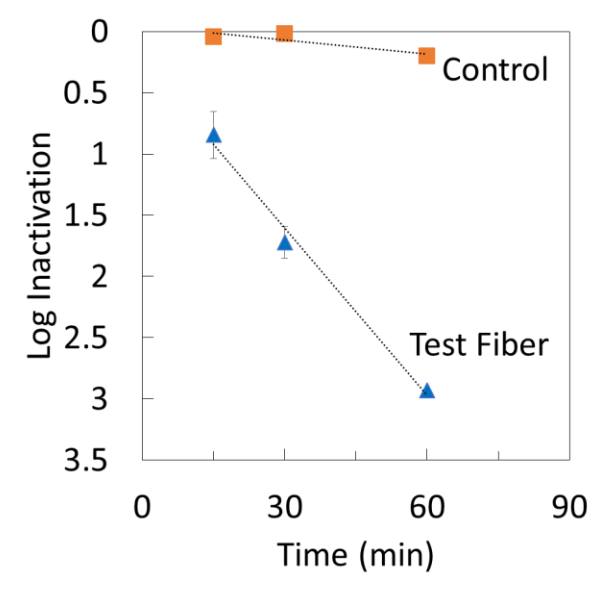

Figure 5-6 Log inactivation of *E. coli* by coupling a UV 265 nm wavelength LED to a side-emitting optical fiber (blue triangles) that included all four preparation steps and a control (orange squares) that included only Steps 1 and 4 (i.e., a clean fiber coated with Cytop^{TM}).

Supplemental Information

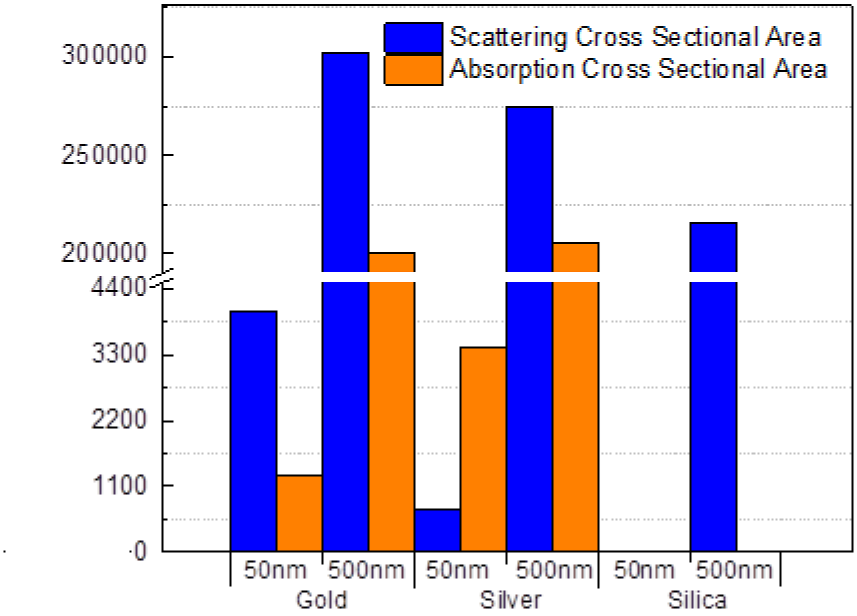

Figure S.I. 5-1 Theoretical scattering and absorption cross sectional area of gold, silver and silica were predicted based on Oldenburg's Mie theory calculator("Mie Theory Calculator," n.d.; Oldenburg, 1999).

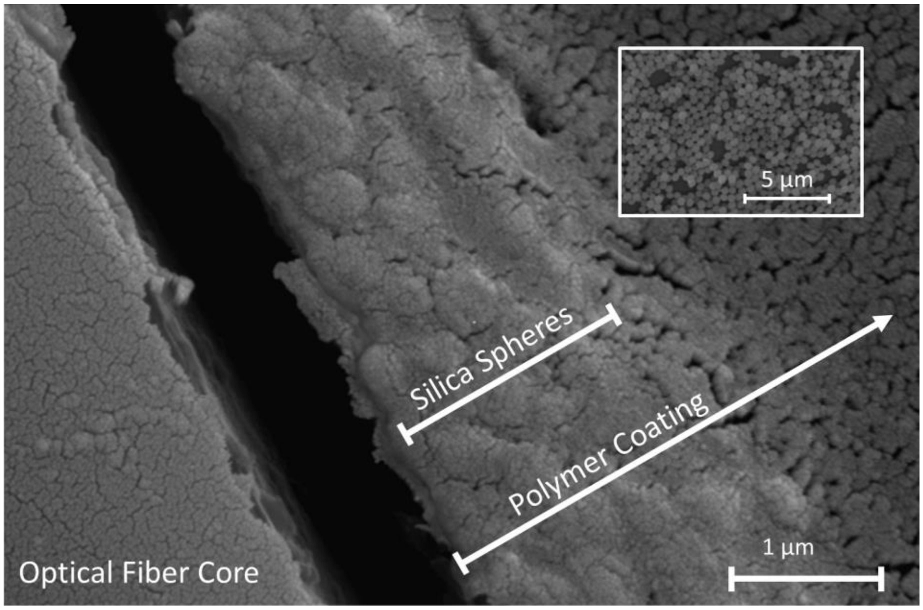

Figure S.I. 5- 2 Scanning electron microscopy (SEM) image of optical fiber cross section after the four-step preparation.

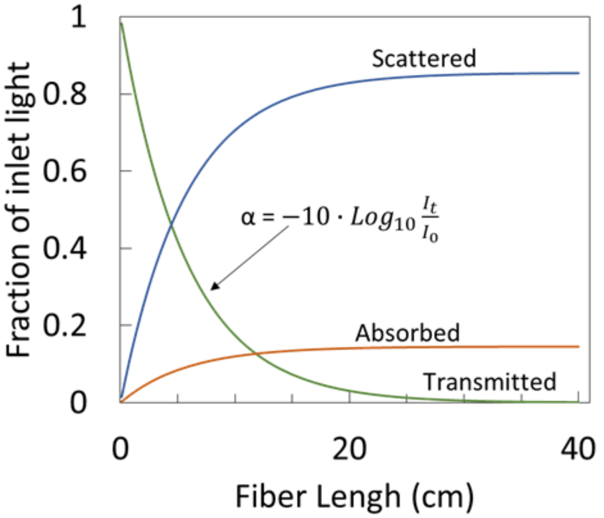

Figure S.I. 5- 3 Distribution of light through the length of the four-step modified optical fiber.

CHAPTER 6

GERMICIDAL SIDE EMITTING OPTICAL FIBERS ENABLE SURFACE INHIBITION OF PSEUDOMONAS AERUGINOSA AND ESCHERICHIA COLI

Text from: Lanzarini-Lopes, Perreault, F., B., Garcia-Segura, S., Westerhoff, P. Germicidal Side Emitting Optical Fibers Enable Surface Inhibition of *Pseudomonas aeruginosa* and *Escherichia coli. Water Research.* (To be submitted in March). Figures included at the end of the chapter.

Abstract

This paper investigates the potential of using UV-C side emitting optical fibers for surface inactivation of pathogenic bacteria. Attaching an SEOF to a single LED increases irradiation area cm^2 by >1000 X that can provide a continuous low-irradiance of UV-C light to prevent biofilm growth on surfaces. A zone of inhibition protocol was developed to quantify the inhibition zone on an agar plate around one optical fiber in function of UV-C fluence. The inhibition zone increased linearly with irradiance time until achieving a maximum inhibition zone. After four hours, an MZI of 2.5 cm to 3 cm was obtained for *P. aeruginosa* and *E. coli*. the surviving lawn edge colonies did not develop UV resistivity after 2 generations of exposure. The agar plate remained bio-available after UV exposure and bacteria could be grown on pre-illuminated area in the absence of UV-C light. These results inform on important design considerations for the use of side emitting optical fibers for surface microbial inhibition in a broad number of applications such as water treatment membranes, distribution pipes and medical equipment's.

Introduction

Pathogenic bacteria growth on surfaces of water treatment and distribution systems create both health hazards and operational problems for the water treatment industry (Garner et al., 2018; Jjemba et al., 2014). In 2017, across the United States there were reported roughly 7,500 cases of Legionnaires disease and 51,000 *Pseudomonas aeruginosa* infections (Centers for Disease Control and Prevention, Legionella). A single planktonic organisms can attach to a surface, grow, and produce extracellular polymers that facilitates the formation of a protective matrix (Donlan, 2001). These rapidly growing organisms can detach from the biofilm and infect drinking water after it has been treated. Additionally, the biofilm itself causes operational problems including iron induced bio corrosion or membrane biofouling (USEPA, 2002).

A crucial step to biofilm management is limiting the initial attachment of microorganism on a surface (Vanysacker et al., 2013). Inactivation of the microorganism by continuous presence of a chemical disinfectant residual can prevent this biological attachment. However, it is nearly impossible to ensure an adequate chemical disinfection dose in premise plumbing through point of use due to stagnant waters, seasonal shutdowns, and low chlorine residuals. Chemical oxidants produce potentially harmful disinfection by-products (DBPs) in the presence of precursors (e.g. NOM, bromine) and require on-site storage or production from liquid or gaseous feedstocks (An et al., 2019; Nieuwenhuijsen et al., 2000).

Ultraviolet radiation (UV) is a chemical-free process for disinfection of pathogens and biofilms and has been studied specifically for the inhibition of *Pseudomonas aeruginosa* biofilm (Argyraki et al., 2017; Chevrefils et al., 2006; Hassen et al., 2000; Stoddart &

Gagnon, 2019). Applying germicidal light requires only electrical power and does not produce DBPs (Schalk et al., 2005). System wide implementation of UV-Light Emitting Diodes (LEDs) specifically would allow for on-demand operation during thriving condition for opportunistic pathogen regrowth (Lu et al., 2015) . These LEDs continue to gain interest in water treatment because to their tunable radiation and power output, lack of warm up time, no degradation from on/off cycle, and lack of mercury (Autin et al., 2013; Beck et al., 2017; Chen et al., 2017; Matafonova & Batoev, 2018). There is a growing interest in using these LEDs to control biofilm growth on surfaces, However, because the emission area of individual LEDs is limited, there is a need for technologies to distribute light from LEDs over larger surface areas. Long arrays of UV LEDs would be needed for adequate illumination to prevent surface bacterial growth (Chen et al., 2017; Martín-Sómer et al., 2017; Oguma et al., 2013; Song et al., 2016). We previously showed 1 LED can be connected to one SEOF that distributes light outward along its entire length to irradiate > 150 cm^2. Multiple (>10) optical fibers can be connected to 1 LED. Thus, SEOFs are envisioned as a strategy to enable LEDs to control biofilm growth over large areas by using a single or networked bundle of multiple SEOFs.

Recently, UV-C Side emitting optical fibers (UV-C SEOF) have been fabricated and illustrated potential for planktonic inactivation of *E. coli* (Lanzarini-Lopes et al., 2019). These optical fibers contain a UV- light guiding silica core, coated with silica nanoparticles, and a UV-transparent polymer coating (Cytop^{TM}). UV-C light traveling through the silica core is scattered by the nanoparticles on the core/cladding interface and emits through the UV-transparent coating into its surrounding. A higher concentration of nanoparticles on the surface of the silica core leads to higher side emission of light. We hypothesize such SEOFs can be used to inhibit biological growth and attachment on surfaces for pathogenic biofilm prevention.

The objective of this study is to demonstrate the potential of UV-C SEOF for surface inactivation of pathogenic bacteria. As illustrated in Figure 6-1, the fiber was place over an agar plate and the zone of inhibition around the fiber was measured to monitor prevention of microbial growth on a surface. *Pseudomonas aeruginosa* (*P. aeruginosa)* was used as the model organism due to its relevance as a biofilm forming pathogen (Vanysacker et al., 2013). *Escherichia coli* (*E. coli)* was also studied for comparison as a well understood organisms. The intensity of UV-C light emitted from an optical fiber was measured along the length and with distance from the SEOF. The lawn's edge colonies where re-exposed to UV to study second and third generation increase in UV-resistivity. Lastly, the bioavailability of the UV-radiated agar was assessed by re-spreading the bacteria over the previous inhibition zone. The paper concludes with important design considerations for the use of optical fibers for surface microbial inhibition.

Methods

2.1 UV-C SEOF fabrication

As previously described (Lanzarini-Lopes et al., 2019), a four-step process enabled fabrication of UV-C side emitting optical fiber. Briefly, the coating and cladding was removed from a 1 mm diameter UV-transmitting optical fiber (FT10000UMT, Thorlabs, Newton, NJ USA), polished and attached to a ferrule connector (O'Neal Tugaoen et al., 2018). A 10 cm fiber was coated with 400 nm aminated silica spheres suspended in ethanol (SIAN*d*-25M, 10 mg/mL, nanoComposix, San Diego, CA USA). The fiber was then submerged in a solution of 0.1 M Na_2SO_4 (239313, Sigma-Aldrich, St.

Louis, MO, USA) and coated with a UV transparent polymer, Cytop^{TM} (CTX 109AE, Bellex international Corp, Wilmington, DE USA).

2.2 Coupling UV-C LED to SEOF

The LED was placed at approximately 1 mm distance (air gap) from the proximal end (near light source) of the optical fiber to maximize light input. A schematic of the UV-LED coupled to the UV-C SEOF is shown in Figure 6-2 Mounting parts were purchased from Thorlabs unless otherwise noted. A (A) 50 mW (max power at 500 mA) 265 nm LED (267 nm peak, 40 nm spectral width) mounted to a 12 X12 mm printed circuit board was purchased from Crystal IS (KL265-50T-SM-WDM2, Island, NY USA). A (B) 15 mm^2 copper plate followed by a (C) 14 mm^2 x 7 mm anodized aluminum heatsink (B07217N5LS, Amazon, Seattle, WA USA) was attached to the back of the LED to assure proper semiconductor cooling. After soldering copper wires to the electrodes, the LED was secured to a (D) lens tube (SM1L05, 0.50’’ length, 1.0’’ diameter) by a (E) ¼’’ expanded PTFE joint sealant (G7816551, Zoro, Buffalo Grove, IL USA) shaped as an o-ring. The (F) UV-C side emitting optical fiber was secured to a (G) stainless steel ferrule multimode fiber connector (110408) and attached to a (H) fiber adapter plate (SM05SMA). Finally, the (I) lens tube adapter (SM1A6FW) connected the fiber components to the LED. In (J) the final set up, the UV-C SEOF is nearly touching the LED to optimize light coupling into the fiber. The optical fiber and UV LED laid horizontal. A fan (HT 900, Honeywell, Charlotte, NC USA) was directed to the LED to increase heat dissipation. A current of 450 mA was delivered to the UV-C LED for all experiments.

2.3 Optical dose measurements

UV-C side emitting flux measurements at fixed locations along the length (L) and perpendicular distance (D) to the surface of the SEOF were obtained using a spectrophotoradiometer (AvaSpec-2048L, Avantes, Louisville, CO USA, calibration: 200 – 1100 nm). The sensor tip of the spectrophotoradiometer (5 mm^2) was placed normal to the fiber (Figure 6-2) . The flux is obtained by integrating the output spectrum. The UV-C LED operated at 450 mA current for all measurements and experiments. Triplicate where obtained for each position along independent optical fibers. In this study, light intensity was measured with air as the medium. The attenuation of light will change for applications in water and other mediums.

2.4 Cell culture

Luria-Bertani (LB) Broth media was prepared according to the manufacturer instructions. Briefly, 25g of LB Broth powder (22091, Sigma-Aldrich, St. Louis, MO USA) was added to 1 L of nano purified water and autoclaved for 15 minutes at 121 °C. *Pseudomonas aeruginosa* (*P. aeruginosa*, ATCC 15692) and *Escherichia coli* (*E. coli,* ATCC 25922) were grown in the media on a shaker plate at 140 rpm in an Isotemp incubator (MaxQ 400, Fisher Scientific, Hampton, NH USA) at 37 °C for 12 hours. The culture was diluted in LB (1:10) and grown in the same conditions until it reached an optical density (OD) of 1 as measured by a Spectrophotometer (Odyssey DR/2500, HACH, Loveland, CO USA). The culture was washed 3 times and resuspended in the wash solution. The wash solution was prepared by diluting 0.9 % wt. of sodium chloride (S7653, Sigma-Aldrich) in nano purified water and autoclaved for 15 min at 121 °C. The process was repeated for each experiment.

2.5 UV-C exposure and zone of inhibition analysis

Zone of inhibition of the UV-C SEOF was measured by placing the fiber on an agar plate spread with a culture of *P. aeruginosa*. The LB Broth agar plates were prepared by dissolving 10 g of Tryptic Soy Agar (2291, Sigma-Aldrich) in 1 L of LB Broth media (described above). The solution was autoclaved, cooled and poured onto 10 cm^2 gridded polystyrene square petri dishes (741470, Carolina, Burlington, NC USA). Once the media solidified, 50 µL of the *P. aeruginosa* solution was spread on top of the agar in order to form a lawn as previously described in inhibition zone studies (Hudzicki, 2009). The UV-C SEOF was immediately positioned directly above the agar through 2 small holes on the side of the plate. The plate remained closed to avoid unwanted contamination. The *P. aeruginosa* spread plates were exposed to UV-C for 0, 30, 60, 120, 249, 480 min of UV light. Triplicates where obtained for each experimental time using different optical fibers.

Two controls were analyzed. In the first, no fiber was added to the plate to visualize a healthy lawn formation. In the second, the fiber was placed on the plate without turning on the LED. This assured that the material properties of the fiber did not have major germicidal effects on *P. aeruginosa*. Additionally, a bare optical fiber was analyzed for comparison. This fiber was stripped of the previous coating and coated with the UV transparent polymer without the addition of nanoparticles. After UV-C exposure, the plates were incubated at 37±1 ºC for 24 h. The distance between the optical fiber and the *P. aeruginosa* lawns on either side of the optical fiber was measured and recorded as the zone of inhibition. The measurement was taken at 0, 2, 4, 6, 8 cm length of the optical fiber to understand how light attenuation affects zone of inhibition.

Results and discussion

3.1 UV-C SEOF light emission profile

Light flux from UV-C SEOFs was measured along the length (L) of the optical fiber at 0, 2, 4, 6, 8 cm and at 0, 1, 2, 3, 4, 6 cm distance (D) perpendicular to the optical fiber. Three UV-C SEOF were measured for triplicate analysis. Figure 6-3 shows that directly adjacent to the fiber (D = 0 cm) there is 19% decrease in the side emitted light flux from the proximal (L = 0 cm) to distal (L = 8 cm) end. At a 3 cm distance, the light flux slightly increases towards the center (L = 4 cm). The path of side emitted photons is not directly normal to the optical fiber and, consequently, at increasing distance from the optical fiber the localized light flux is a sum of the flux form the entire length of the optical fiber. A larger fraction of light rays will reach the spectrophotometer at the center (L = 4 cm) position.

Figure 6-3 inset shows an attenuation of light with increased distance from the optical fiber based on average flux measurements at distance from the fiber. The localized flux drops from an average of 30 µW/cm^2 at D = 0 cm to 0.5 µW/cm^2 at D = 6 cm. Perpendicular to the fiber, light intensity (I_0) exponentially decreases as it passes through air or water. This phenomenon is modeled through Beer- Lamberts law, where I is the resulting intensity after a specific pathlength (l) and (α) is the attenuation (absorbing and scattering) coefficient of the medium.

$$I = I_0 \cdot e^{-l \cdot \alpha}$$

However, two factors limit the decay of light from the UV-C SEOF from directly fitting Beer-Lambert law. First, at D = 0 cm the sensor is directly in contact with the optical fiber and can be measuring components of the evanescence wave that does not permanently leave the optical fiber core. Optical fibers are waveguides, meaning they deliver light from one end to the other (Figure 6-3A). Light is totally reflected internally by a difference in index of refraction from the optical fiber core and external cladding. Every time photons reach the surface of the optical fiber and are reflected inwards, it results in an electromagnetic disturbance, called the evanescent wave (Prieve & Walz, 2009). This wave exits the fiber core and exponentially decays with distance from the fiber interface. If there is no physical interference (i.e. impurities, nanoparticles), the wave returns to the cladding without losing energy and the light is emitted at the end of the fiber (Figure 6-3A). This explains the 90% drop in light intensity from D = 0 to D= 1 cm.

Second, Beer-Lambert Law assumes one-point source. As D increases so does the number of point sources from the optical fiber that are detected by the spectrophotoradiometer. This results in an overall higher localized flux than modeled by Beer – Lamberts Law. Figure 6-3 (inset) shows Equation 1 closely fits the data after 2 cm from the optical fiber. At this point there is no longer significant addition of point sources with increasing distance from the optical fiber. In conclusion, there is decrease in light flux through the length of the SEOF. Additionally, beer lamberts law can be used to predict light decay with distance from the fiber.

3.2 Zone of inhibition around SEOF

A UV-C SEOF was placed 3 mm above an agar plate covered with a culture of either *P. aeruginosa* or *E. coli*. Figure 6-4 illustrates the *E. coli* lawn after eight hours of irradiation for the optical fiber without SiO^2 modification (Figure 6-4A) compared against a UV-C SEOF (Figure 6-4B). Figure 6-4 insets show the light distribution through the length of the optical fiber. The image was captured under dark conditions with a paper towel placed below the optical fiber. The blue light seen in the image is an artifact of the paper towels interaction with the UV-C light that results in a quantum-shift. The bright spots seen towards the top of both images is due to (i) end emission of light, and (ii) back reflection at the distal (away from light source) end of the fiber. When the light reaches the distal end of the fiber, most of it exits the fiber. A portion of light also reflects towards the optical fiber creating a second “input” light and higher photo density at the distal end of the optical fiber.

The Zone of inhibition 8 hours of irradiation with the SEOF is 2.8 cm. In contrast the zone of inhibition is 11 X smaller (0.26 cm) for no SiO_2 scattering centers on the optical fiber. The nanoparticles on the former, interact with the evanescent wave and results in side-emission through Mie scattering, creating the visible side emission “glow” from Figure 6-3B inset (Lanzarini-Lopes., 2019). This glowing germicidal light enables the microbial inactivation through the length of the optical fiber illustrated in Figure 6-3B. The observable inactivation along the length of the bare optical fiber is likely due to impurities in the surface of the optical fiber since the fiber was not prepared in a clean room. Additionally, the zone of inhibition increases slightly towards the distal end of the fiber. This is due to the higher photon density of photons at the fiber that was described earlier.

3.3 Zone of inhibition of E. coli and P. aeruginosa increases with dose

Figure 6-5 illustrates the zone of inhibition of *P. aeruginosa* (Figure 6-4A) and *E. coli* (Figure 6-4B) resulting from UV-C SEOF exposure on an agar plate lawn. Exposure times of 0, 30, 60, 120, 240, and 480 minutes to study the effect of UV-C dose (dose =

flux x time) on zone of inhibition. At each exposure time, the zone of inhibition was measured at L = 0, 2, 4, 6, and 8 cm along the length of the fiber, from the proximal end of the LED source. A dark control was obtained by placing the modified optical fiber in the agar plate with to UV exposure. No inhibition was observed by the dark control, indicating that the exterior materials of the optical fiber did not contribute to the germicidal effect of the UV-C SEOF.

Figure 6-5 shows the zone of inhibition is highest at the proximal end and lower towards the distal end for lower exposure times ($t < 120$ min) with both *P. aeruginosa* and *E. coli.* This observation corresponds with the UV-C side emission profile (Figure 6-3). As light side emits from the optical fiber, the density of photons inside the fiber decreases. This phenomenon is called the Beer-Lambert law of attenuation through a waveguide. A lower density of photons means that less light can be emitted through the side of the fiber. However, the path of side emitted photons is not directly normal to the optical fiber. At increasing distance from the optical fiber, the localized light flux is a sum of the flux form the entire length of the optical fiber.

Figure 6-5 also shows that for $t > 120$ min a maximum zone of inhibition is reached, defined as the maximum zone of inhibition (MZI). Figure 6-5C illustrates that linear increase in zone of inhibition with time reaches a maximum of ~2.9 cm at around 4 hours of irradiation. At 4 hours at the edge of the MZI, the UV dose is approximately 18.7 mj/cm^2 (flux = 1.3 uW/ cm^2). Between 4 and 8 hours there is no statistically significant change in zone of inhibition for either organisms according to the student t-test with 95% confidence level ($p > 0.05$).

At the edge of the inhibition zone, the localized photon flux is insufficient to either (i) damage the DNA and protein of the organism, or (ii) surpass the rate of DNA and protein reconstruction (Hu et al., 2005; Quek & Hu, 2008). Ultraviolet-C radiation is categorized as germicidal because it inhibits pathogens (i.e. bacteria, virus, protozoa) from replicating and infecting a host (Gayán et al., 2013). Absorption of UV light by nucleic acids results in crosslinking between thymine and cytosine. The mutation disables hydrogen bonds to the purine base of the opposite strand, therefore inhibiting replication and resulting in cell death. The amount of cross linked pyrimidine nucleoside bases is directly related to the UV exposure (Blatchley et al., 2001). Certain organisms can repair damaged DNA when the UV dose is too low. This process reverts DNA back into its undamaged form (Branzei & Foiani, 2008). At the low localized photon flux after MZI the DNA repair can exceed DNA damage, limiting further inactivation of the microorganism.

The MZI is a dependent on (i) the sensitivity of the microorganism to UV light, and (ii) the input power of the LED. By student – t test here is no statistical difference in either MZI or zone of inhibition ($p > 0.05$) at each irradiation time of *P. aeruginosa* and *E. coli* through the entire length of the fiber. This result is supported by similar UV sensitivity reported for these organisms. For 4 log inactivation, a range between 3.1 – 17 mJ/cm^2 has been reported for planktonic *P. aeruginosa and* 3.0 to 20 mJ/cm^2 for planktonic *E. coli* (Abshire & Dunton, 1981; Chatterley & Linden, 2010; Chevrefils et al., 2006; Clauß, 2006; Quek & Hu, 2008).

3.4 Edge colonies did not illustrate higher UV resistance

To understand if the edge colonies (Figure 6-1) have significantly higher UV resistivity then the bulk, the same zone of inhibition experiments where conducted with the edge colonies as the inoculum. Like the zone of inhibition measurements, the UV-C SEOF was placed 3 mm above an agar plate covered with a culture of *P. aeruginosa*. After 4 hours of irradiation, the fiber was removed, and the plate was incubated for 24 hrs. One isolated colony at the edge of the *P. aeruginosa* lawn was resuspended in LB overnight and spread on a new agar plate followed by the cell culture and zone of inhibition analysis procedure. The entire process was repeated twice. The zone of inhibition after 4 hours was then measured to understand if the colonies at the edge of the lawn where more resistant to UV. Figure 6-6 illustrates the sequence of experiments, where Figure 6-6A is the virgin plate, and Figure 6-6B and 6-6C illustrate the results after one and two resuspensions, respectively. In the image, the LED is located towards the bottom of the plate and the fiber ran through the center (through the visual hole on the top and bottom). The black circle in Figure A and B illustrates the colonies that were resuspended for the following experiment.

The zone of inhibition of 0, 1, and 2 generations are 2.40 cm, 2.52 cm, and 3.10 cm. There results fall within 1 standard deviation of the average zone of inhibition for 4 hours of irradiation. The protrusions and patchiness patterns in each agar plates results from uneven spread plate pressures and agar scrapes (see center of Figure 6-6B). Overall, there was no significant difference in the zone of inhibition after one or two resuspensions. Consequently, the survival of the edge bacteria is because of insignificant UV flux as explained in section 3.2. Thurs, the zone of inhibition is a valid measurement to inform the maximum necessary optical fiber distance for complete surface inactivation. The UV flux that reaches this area is insufficient to either damage the DNA and protein of the organism, or surpass the rate of DNA and protein reconstruction (Hu et al., 2005; Quek &

Hu, 2008). However, to truly understand weather UV resistivity is being developed a longer-term study with more than two generations of resuspension should be conducted.

3.5 Agar plate remained bio-available after UV exposure

The zone of inhibition is measured by prevention of cell growth on an agar plate. It is possible that cells would not grow on the plate if (i) the cell themselves are damaged, or (ii) the nutrients on the agar plate are no longer bioavailable because of surface damage by UV-C light. To establish the former as the primary mechanism, the *P. aeruginosa* colonies were re-spread on an agar plate after initial UV irradiation. The three steps to this procedure are illustrated in SI. Figure 6-1. Si. Figure 6-1A is the *P. aeruginosa* lawn after 4 hours of inactivation and 24 hours of incubation. S.I. Figure 6-1B illustrates the plate after the lawn has been evenly respreads through the plate, and S.I. Figure 6-1C illustrates the plate after an additional 24 hours of incubation.

The cell density on the sides of the initial plate is extremely dense. Re-spreading those cells results in streaks and uneven distribution of bacteria throughout the agar plate. However, there is a clear difference in density before and after 24 hour incubation indicating cell replication. The growth of cells on the entire surface of the agar plate illustrates that the agar remains bio-available after UV radiation. Additionally, the center of the agar plate has higher cell growth as indicated by opaqueness. Existing cellular and extracellular material from S.I. Figure 6-1A likely remained on the surface of the agar preventing new cells from using the nutrients underneath them. Thus, we conclude the UV-C SEOF inactivated the microorganisms within the measured zone of inhibition.

Summary and Conclusions

UV- C SEOF can effectively inactivate *P. aeruginosa* and *E. coli* even very nutrient-rich surfaces. Subsequent experiments using the edge lawn- colonies as the inoculum indicated that the bacteria do not develop significant UV resistivity within two generations of exposure. Re-spreading the previously UV radiated plate indicated that microbial growth prevention was due to biological inactivation and not damage to the agar. The zone of inhibition at various times was compared. The zone of inhibition increased linearly with dose until a MZI of 2.88 and 2.81 cm was achieved for *P. aeruginosa* and *E. coli* respectively after four hours of exposure. After which the low flux of radiation reaching the surface is too low to damage the cell's DNA. The photon flux at the edge of MZI is the minimum flux needed to inactivate the bacteria of interest. This needs to be considered when designing UV-C SEOF configurations for surface disinfections. For example, the flux (Figure 6-3 inset) that reaches the MZIs of 2.88 and 2.81 cm are 2.31 $\mu W/cm^2$ and 2.37 $\mu W/cm^2$, respectively. To assure full inactivation of *P. aeruginosa* and *E. coli*, it is crucial that the localized flux in the entire surface of interest is greater than those values.

The maximum distance between the optical fibers can be varied by changing the input power of the LED or decreasing the density of nanoparticles at the surface of the optical fiber. Higher power to the LED would directly result in higher side emission flux, which would increase the maximum separation distance. Alternatively, attaching less nanoparticles to the surface of the optical fiber core would decrease how much light leaves the optical fiber (scattering coefficient) at each location, decreasing the maximum separation distance. Because less light is side emitted per distance, this modification would enable longer optical fibers to be fabricated. These results inform engineering design decisions for surface disinfection with UV-C SEOF. For example, these optical fibers can be used as spiral wound membrane spacers to prevent biological fouling. Spacer holes are relatively small (< 0.1 cm) to ensure proper hydraulic turbulence. In this configuration, long optical fibers with increasing scattering coefficients would be designed to assure even light distribution across the optical fiber mesh.

The SEOFs described herein can overcome the largest barrier to UV-C disinfection: optical obstruction in reactors as a result of bends or suspended particles. Figure 6-7 illustrates a schematic of light distribution in a U-bend cylindrical geometry (A) without and (B) with side emitting optical fiber. Any interference between the linear pathway of a light source and surface will result in non-effective illumination of that surface. An SEOF simulates infinite light sources, guiding the light past the optical obstructions, and illuminating the entire inter surface of interest. The flexibility of these optical fiber enables them to follow any shape, preventing microbial growth in any geometry or configuration (i.e. pipes, membranes, etc). Future work will explore long term microbial prevention in flexible pipes and tubbing.

Acknowledgements

We thank Professor Morteza Abbaszadegan and Dr. Absar Alum for the knowledge about microbial essays. We additionally thank Michelle Ladreville and for assistance during previous biofilm work that led to this study. This work was partially funded by the National Science Foundation (NSF) through the Nanotechnology-Enabled Water Treatment Nanosystems Engineering Research Center (EEC-1449500) and the Interdisciplinary Graduate Educational Research Traineeship: Solar Utilization Network fellowship (DGE-1144616). We acknowledge the use of facilities within the Eyring Materials Center at Arizona State University supported in part by NNCI-ECCS-1542160. Technical editing was provided by Laurel Passantino.

Figures for Germicidal Optical Fibers Enable Surface Inactivation of Pseudomonas aeruginosa

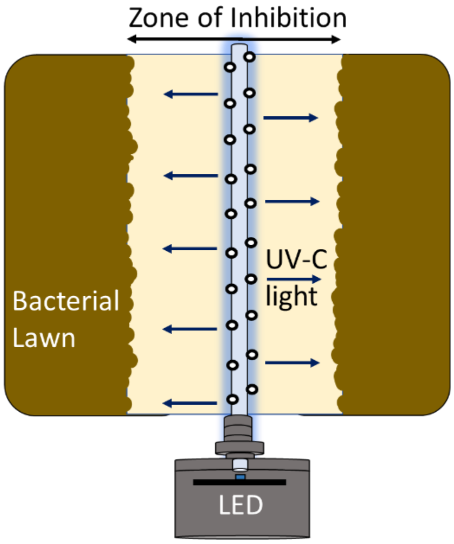

Figure 6-1 Schematic of the zone of inhibition resulting from placing a UV-C SEOF over a bacterial spread agar plate.

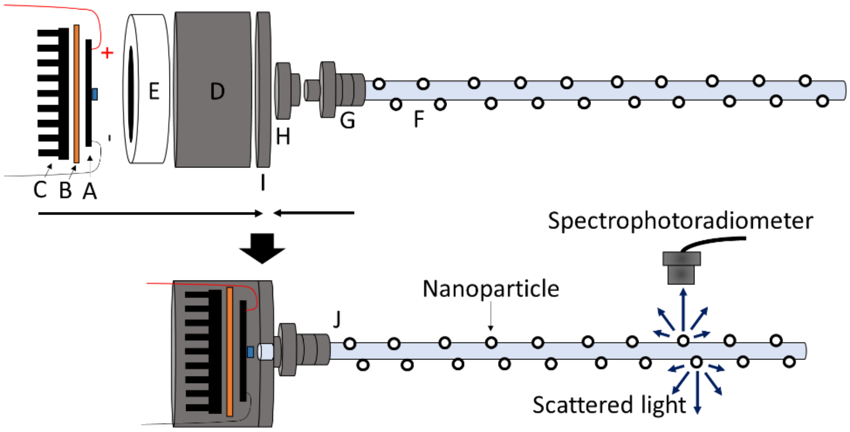

Figure 6-2 Schematic of UV-C LED coupled to an SEOF.

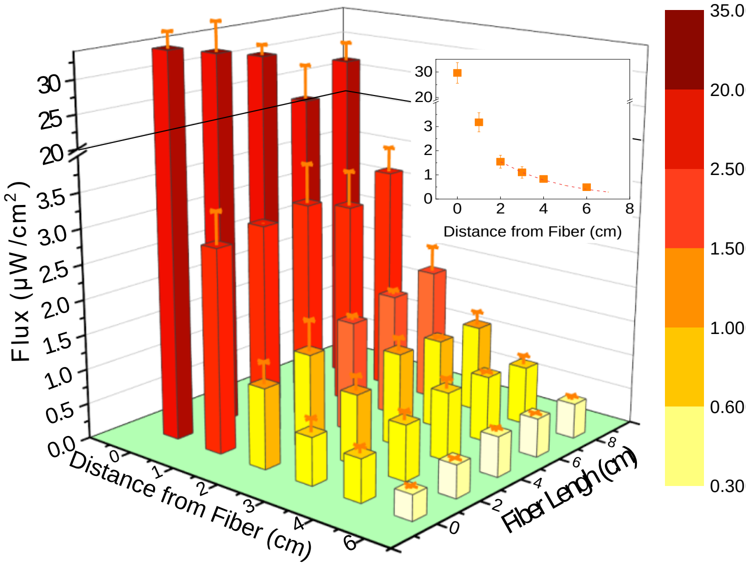

Figure 6-3 Experimental flux measurement at different distances away from the surface of a SEOF, and along the length of the fiber. Inset illustrates the average UV flux with a distance from the UV-C SEOF.

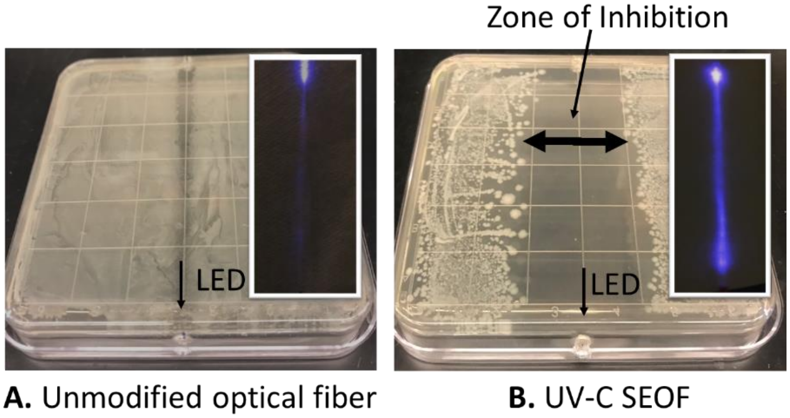

Figure 6-4 *E. coli* lawn after eight hours of exposure to an (A) unmodified optical fiber and (B) UV-C SEOF connected to a UV 265 nm LED. The inset of both images illustrates the corresponding optical fiber used in each experiment.

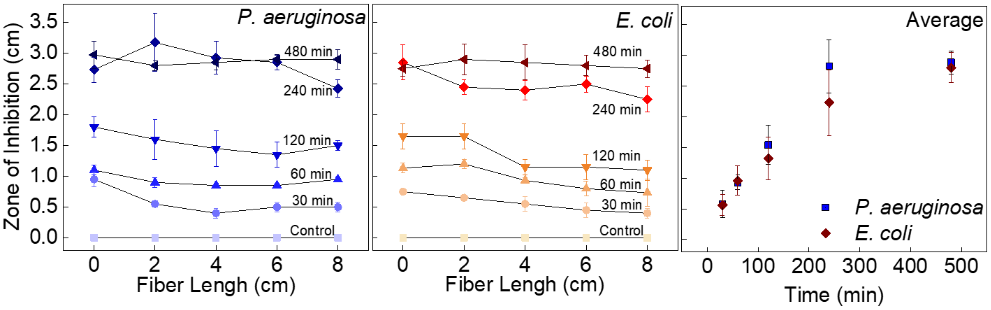

Figure 6-5 Zone of inhibition for (A) *P. aeruginosa* and (B) *E. coli* respectively through the length of the optical fiber and (C) as an average of the fiber length.

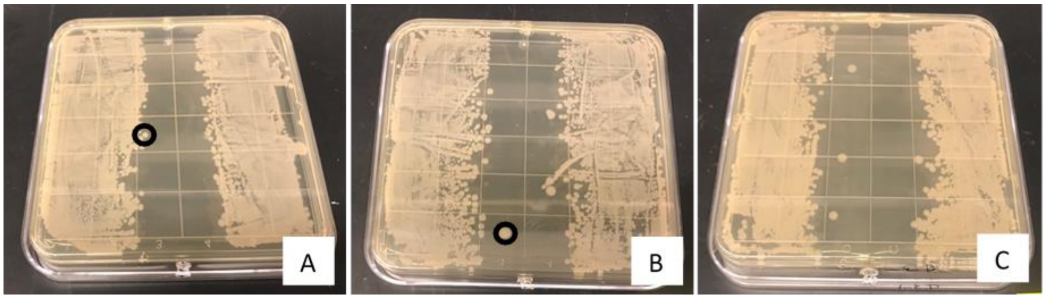

Figure 6-6 Photos of the edge colony resuspension sequence. Photo A is the virgin inoculum and B and C are the plates after one and two resuspension and irradiation respectively.

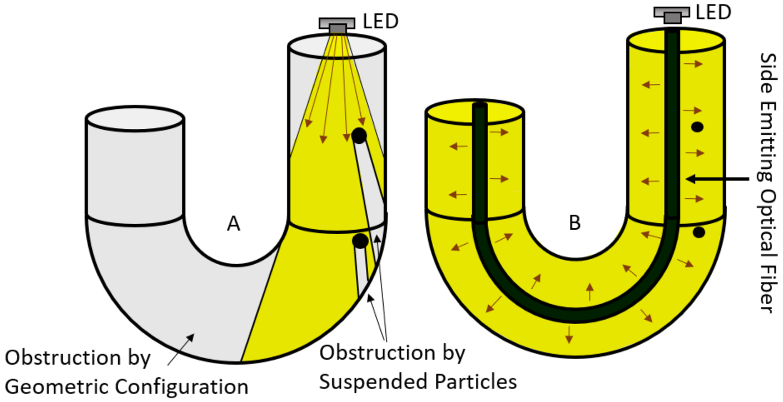

Figure 6-7 Schematic of light distribution by UV LED in a tubular geometry (A) without (B) with side emitting optical fiber.

Supplemental Information for: Germicidal Side Emitting Optical Fibers Enable Surface Inhibition of Pseudomonas aeruginosa and Escherichia coli

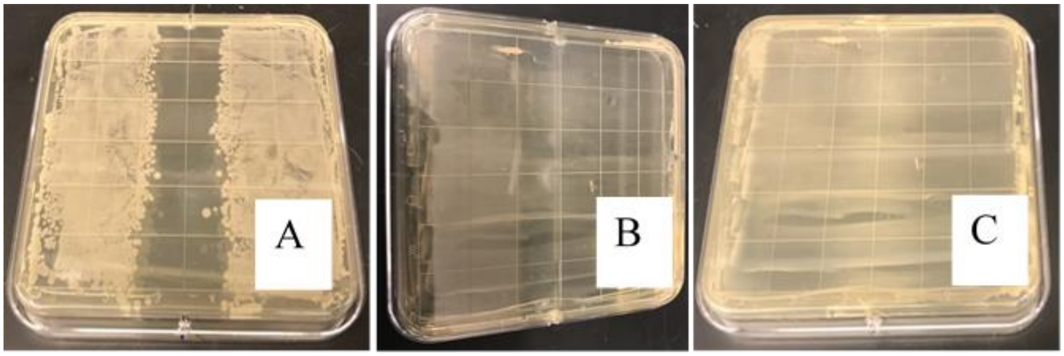

Figure S.I. 6-1 Photos *P. aeruginosa* lawn agar plate after a (A) 4 hr. zone of inhibition experiment, (B) re-spreading of the same plate and (C) incubation of that plate for 24 hours.

CHAPTER 7

SYNTHESIS

I am interested in exploiting light driven reactions to avoid the adverse environmental impacts associated with continuous chemical and material consumption of advanced water treatment technologies used today. A barrier to light-driven water treatment is optical obstruction in aquifers or pipelines that limits light propagation from the sun or a single artificial light source. As demonstrated in this dissertation, side emitting optical fibers (SEOF) can guide light past optical obstructions (Figure 7.1) increasing the surface area (cm^2) of a small point source by 1000 X to enable water purification. The purpose of this chapter is to synthesize knowledge presented throughout dissertation to identify barriers and opportunities for large scale fabrication and implementation of visible – UV SEOF in water purification.

Figure 7-1 illustrates the three objectives of this dissertation that enabled the fabrication and application of SEOFs in the visible through UV-C spectrum. The first objective was to use a visible light SEOF to increase oxygen level in a subsurface environment. We achieved supersaturated oxygen level of > 15 mg/L during ON light conditions (Lanzarini-Lopes et al., 2018). This objective illustrated the capability of enhancing environmental remediation through SEOF. However, UV absorption (~ 100 %) by the polymeric core limited the application of this optical fiber to visible light only.

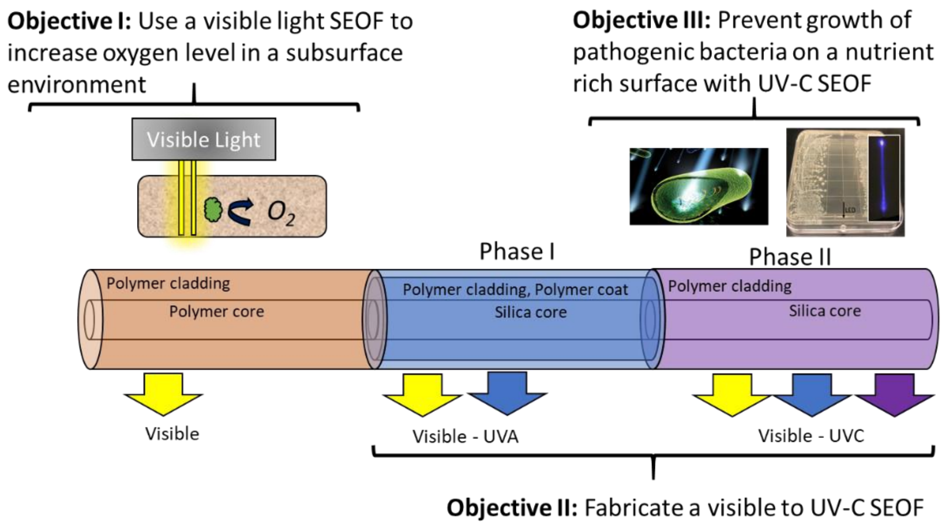

Figure 7-1 Schematic of three objectives of this dissertation along with the optical fibers used and developed in completing each objective.

The second objective was to fabricate a SEOF able to side emit visible to ultraviolet wavelengths of light to inactivate planktonic bacteria. This was accomplished in two phases. First, I modified the cladding of silica core optical to increase UV light side emission by ~10 times. I identified that (i) that silica particles can serve as scattering centers when positioned near the optical fibers core and (ii) UV-C light emission was limited by the absorption of high frequency radiation by the polymer cladding (Lanzarini-Lopes, Garcia-Segura, et al., 2019). In Second, I used silica nanoparticles and a UV-transparent polymer to fabricate a visible through UV-C SEOF. One optical fiber coupled to a 265 nm LED achieved 3 log inactivation of E. coli in 1 hour of contact time (Lanzarini-Lopes et al., 2019).

The third objective was to prevent growth of pathogenic bacteria on a nutrient rich surface with a UV-C SEOF. By placing the UV-C SEOF above pathogen spread agar plates, I visually illustrated that one optical fiber can inhibit growth of *P. aeruginosa* and *E. coli* for ~ 2.9 cm along the length of the fiber.

A different optical fiber was used in each study. In Objective I the fiber contains a polymer core with a polymer cladding. The optical fiber in Phase I of Objective II, contained a silica core covered by a polymer cladding and an additional polymer coating for protection. The optical fiber used in both the second phase of Objective II and in Objective III, contained silica core coated with one polymer cladding. These differences are a function of whether the cladding material is structurally able to protect the optical fiber core. If both the cladding and core was made of glass or hard polymer materials, then a second layer of polymer was applied (i.e. Phase II - Objective II).

Selection of UV-non absorbing silica core, nanoparticle scattering centers and polymer coating is important in the fabrication of visible through UV SEOF. The silica preforms used in the optical fiber core should have high hydroxyl content. Hydroxyl functional groups decreases UV loss caused by electronic resonances from unbound electrons (Fujino, 2005; Jeanmonod et al., 2011). Additionally, the nanoparticles used as scattering center should have a low ratio of absorption to scattering coefficient. Light interaction with a particle is either absorbed (absorption cross-sectional area) or scattered (scattering cross-sectional area) (Bohren, 1956) . The theoretical scattering and absorption cross-sectional area of nanoparticles can be predicted based on Oldenburg's Mie theory (Oldenburg, 1999). For example, silica spheres are ideal nanoparticle choice because of their significantly higher scattering cross-sectional area than absorption cross-sectional area as illustrated in the Chapter 5 S.I. The size of the nanoparticle is as significant as the material. The ratio of absorbed to scattered energy (I_A/I_S) increases with decreasing diameter because the particle scattering cross-sectional area decreases in proportion to its volume for $d \lesssim \lambda$ (Bohren & Huffman, 2007; Van De Hulst, 1957). Therefore, the nanoparticle should be slightly larger than the wavelength being scattered.

Like many other technologies, for the visible through UV SEOFs to impact the water treatment industry, they must be commercialized. The maturity of research innovation can be assessed by the index of technology readiness for commercialization created by NASA. The technology readiness levels (TRL) ranges from fundamental research phase (1) to commercial deployment (9). SEOFs are currently in feasibility demonstration phase (TRL 3). Higher TRLs (4-6) includes lab scale development, technology development, and viability demonstration. The appropriate roadmap to reach these TRLs include the large-scale fabrication of SEOFs and testbed design with metric driven process for both biological remediation and ultraviolet disinfection described below.

Large Scale Production of Visible to UV-C SEOF

The four step UV-C SEOF process identified in chapter 5 can be scaled up to fabricate > 1 km of optical fiber in existing optical fiber draw towers. Figure 7-2 illustrates the existing draw tower process of fabricating optical fibers. The silica glass preform is placed in a 1,900 °C drawing furnace and dropped three stories at variable speeds to achieve the desire diameter of the core. Two sets of polymer dies coat the optical fiber with a cladding and coating layer. The fiber is then wound into 0.2 m diameter drums to allow for fabrication of ~30 km of optical fiber. In the fabrication of the SEOFs described here, the primary die would contain a solution of aminated silica spheres to evenly coat the optical fiber with the nanoparticles. The secondary die would contain the UV-C transparent polymer, Cytop^{TM}. Alterations to this process is to suspend the silica nanoparticles in Cytop^{TM}, like the procedure described in Chapter 4.

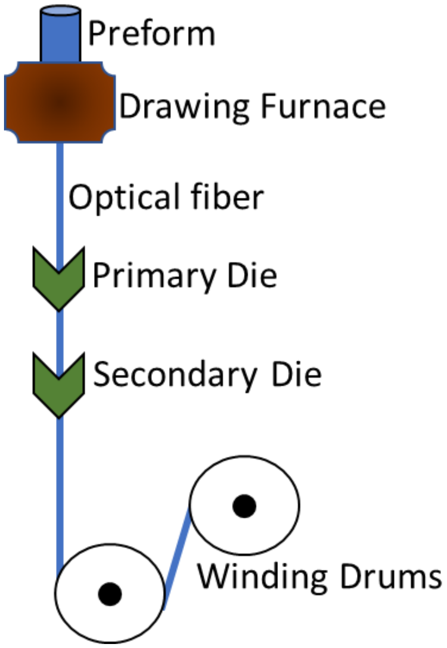

Figure 7-2 Schematic of tower used to fabricate the modified optical fiber and control the particle addition into the cladding.

The limited availability of UV transparent polymers in the market is a barrier for the scaled-up production of visible through UV SEOFs. PMMA has been repeatedly used in UV-AB applications (Kundu & Kelly, 2018; Wang et al., 2017). The exponential increase in absorption of light below wavelength of 300 nm limits PMMA to UV-AB applications only. Cytop^{TM} is a transparent fluoropolymer that reports > 95% transmittance (200 µm thickness) for UV 265 nm wavelength ("Cytop - Usage,"). Additionally, Cytop^{TM} is ideal in optical fiber application due to the lower index of refraction than the silica core. However, Cytop^{TM} currently costs ~$950 /50 ml, therefore more economical options should be considered when scaling up the SEOFs.

A second barrier of side-emitting optical fibers is the logarithmic decay of light through the optical fiber, guided by Beer-Lambert law, that could cause uneven side emission along the fiber length. This logarithmic decay can be mitigated by either (i) exponentially increasing the scattering coefficient through the length of the optical fiber, and (ii) adding a light source at both ends of the optical fiber.

The scattering coefficient of the optical fiber determines what percent of the total light in the fiber will leave per length of fiber. Figure 7-3 illustrates the theoretical uniformity that can be achieved by exponentially increasing the scattering coefficient along the length of the optical fiber (Biyarin et al., 2017; Patent No. WO2014121172A2, 2017). The dotted lines represent the theoretical side emission (μW/m) and total power (mW) in red and black respectively for an SEOF with constant scattering coefficient. As expected, both the total power and side emission logarithmically decrease through the optical fiber length. The solid lines represent the theoretical side emission (μW/m) and total power (mW) in red and black respectively for an SEOF with exponentially increasing scattering coefficient. As illustrated, we can achieve a constant side emission with a linear decrease in total power within the optical fiber. In fabrication of aSEOF, the scattering coefficient can be controlled by the (i) density of nanoparticles or (ii) ionic strength of the solution the optical fiber is exposed to.

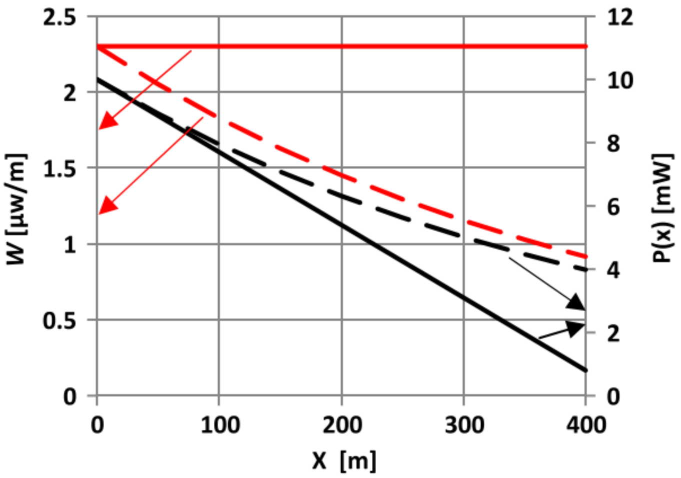

Figure 7-3 Theoretical side emission (red line: µW/m) and total power (black line: mW) through an optical fiber with constant scattering coefficient (dotted line) and exponential increase in scattering coefficient (solid line). This figure was taken from Biyarin et al. 2017(Biyarin et al., 2017).

Alternatively, light can be supplied from both ends (proximal and terminal sides) of the optical fiber using two LEDs. Figure 7-4 illustrates the theoretical side glowing intensity profile (A.U.) of the optical fiber with one light source at each end individually (1,2) and with both combined (Total) (Xu et al., 2008b). In this study, the optical fiber had a consistent scattering coefficient of 0.01 m^{-1}. Both the total power and uniformity of side emission significantly increases for the 100 m optical fiber.

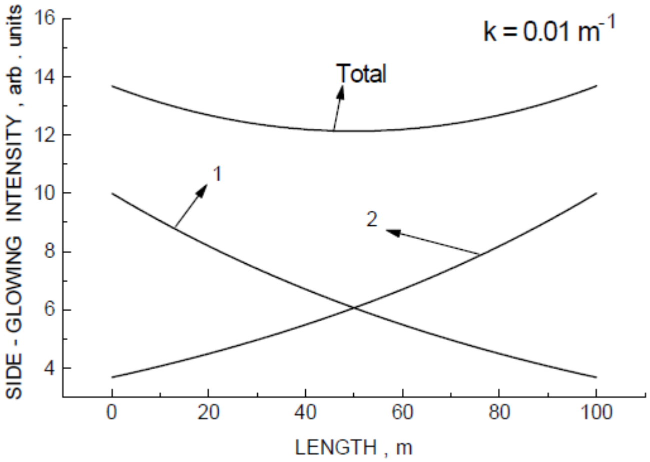

Figure 7-4 Theoretical light emission through the length of an optical fiber with one light source at each end. The figure was taken from Spigulis 2005 (Spigulis, 2005).

Visible light to Enable Passive Treatment of Groundwaters

Remediation of polluted groundwater often requires artificial oxygen delivery into subsurface to sustain aerobic bacteria (Chapelle, 1999; Hess et al., 1996; Khan et al., 2004; Korda et al., 1997). Oxygen is used as an electron acceptor and metabolic co-reactant for various microorganism. However, these methods energy and resource intensive. Instead, oxygen surplus can be simulated by growing photosynthetic microorganisms in soils by delivering natural sunlight to the subsurface with visible light SEOFs in a passive biological treatment wall-like system (Khan et al., 2004). With enough light, photosynthetic microorganisms convert carbon dioxide into cellular material and generate oxygen (Kuo et al., 2012). Phototrophic organic material can provide substrate for a diverse group of microbes to aid in pollutant degradation (Filip et al., 1979). Therefore, carbon can be cycled between inorganic and organic forms in a sustainable strategy. Chapter 3 demonstrated that one SEOF can increase the oxygen level of a granulated sand reactor to 15 mg/L.

The next phase of this work should include a test bed design with metric driven processes for biological remediation. Figure 7-5 illustrates a conceptual model for creating a bio-barrier with visible light SEOFs. Multiple optical fibers would be placed in parallel creating a curtain like structure normal to the flow of water. Solar light alone or augmented by artificial light can be used for passive treatment of induced hydrocarbon plumes. Metrics of electrical energy per order and mineralization coefficient would be used for technology comparison to artificial oxygen delivery to the subsurface.

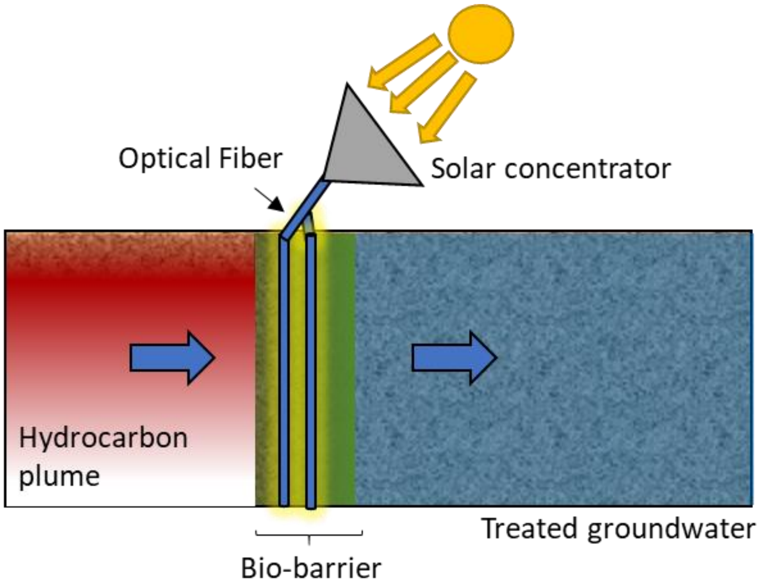

Figure 7-5 Conceptual model of a bio-barrier for hydrocarbon treatment of groundwater in a subsurface environment with solar light delivery through optical fibers.

UV-C SEOFs can Prevent Biofilm Formation

Growth of pathogenic bacteria in hard to reach places (i.e. water distribution pipes, storage systems) create both health hazards and operational problems for the water treatment industry (Garner et al., 2018; Jemba et al., 2014). A single planktonic organisms can attach to a surface, grow and produce extracellular polymers that facilitates the formation of a protective matrix of the biofilm (Donlan, 2001). Once mature, the biofilm releases high concentration of microorganisms facilitating rapid subsequent biofilm growth and human infection.

Chapter 6 illustrated that the SEOFs fabricated in this dissertation can deliver a constant dose of germicidal radiation to prevent microbial growths on surfaces. This finding indicated elimination of the first crucial step to biofouling (Vanysacker et al., 2013). Additionally, the SEOFs can overcome the largest barrier light driven reactions: optical obstructions in reactors as a result of bends or suspended particles. However, no research has been done with SEOFs in bent configurations or confined spaces. The next phase of research should include test bed designs for biofilm prevention in (i) membrane spacers and (ii) U-bent cylindrical tubes as described below.

SEOFs can be used as spiral wound membrane spacers to prevent biological fouling. Thinner SEOFs (< 300 um) would be fabricated to increase the flexibility of the material. The optical fibers should then be arranged in a crossed mesh configuration to assure proper hydraulic turbulence of existing membrane spacers. Metrics of assessment should include membrane flux and biological cell growth on the membrane surface when compared with standard membrane mesh. Various mesh configurations can also be compared. Chapter 6 illustrated that the maximum separation distance between the optical fibers for successful microbial inactivation is determined by the emitted UV-C flux. The flux can be controlled by changing the input power of the LED or decreasing the density of nanoparticles at the surface of the optical fiber. Higher power to the LED would directly result in higher side emission flux, which would increase the maximum separation distance between the optical fibers. Alternatively, lower nanoparticle loading on the surface of the optical fiber core decreases how much light leaves the optical fiber (scattering coefficient) at each location, decreasing the maximum separation distance. The second test bed case study should be biofilm prevention in U-shaped cylindrical tubes. Growth of legionella on piping of shower heads cause > 7,000 biofilm related infections each year. Although ultraviolet radiation can prevent biofilm growth, propagation of UV light through pipes are difficult due to bent geometries that result in shading. Any interference between the linear pathway of a light source and surface will result in non-effective illumination of that surface. An SEOF simulates infinite light sources, guiding the light past the optical obstructions, and illuminating the entire inter surface of interest. One SEOF connected to a single UV-C LED can illuminate > 1 m of length along the shape of the pipe. Figure 7-6 illustrates a schematic of light distribution in a U-bend cylindrical geometry (A) without and (B) with side emitting optical fiber. This test bed study should analyze the long-term ability of SEOFs to prevent biofilm growth on U-shaped pipe.

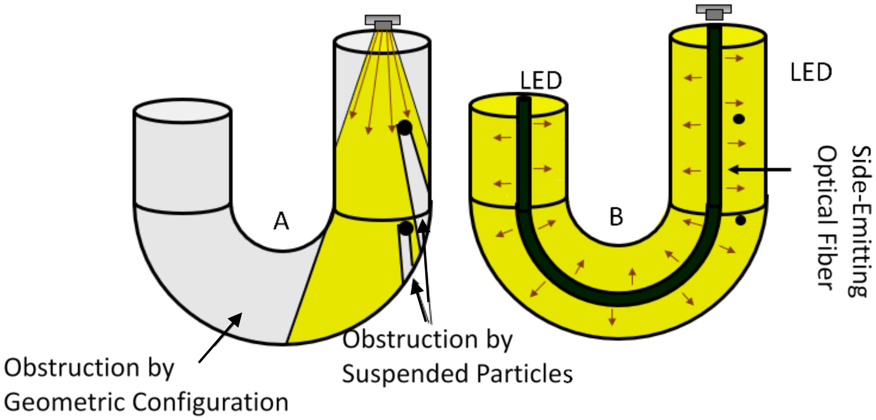

Figure 7-6 Schematic of possible optical obstructions within reactors and environmental systems that hinder the use of existing lamps in light driven water treatment. Figure A illustrates an U-shaped reactor with illumination from a stand alone UV-C LED. Figure B illustrates the same U-shaped reactor with a UV-C LED attached to an SEOF. Maroon arrows indicate ray traces.

The Future of SEOFs

Laboratory scale experimental results showed promising potential for enhancing water purification with visible through UV-C SEOF. In order to reach higher technology readiness levels, the optical fiber and experimental conditions must be scaled up. Scale up of visible through UV-C SEOFs should be done using existing optical fiber draw towers with few modifications. The main impact of scaling up visible SEOFs is for passive biological remediation of groundwaters. The main impact of scaling up

UVSEOFs is the opportunity to prevent biofilm formation in membranes and pipingby coupling > 1 m SEOF to a UV-C LED. The long-term vision of this work is providing a consistent disinfection dose in premise plumbing and water distribution pipes. These optical fibers can be implemented in shower heads to prevent opportunistic respiratory pathogens from infecting immunocompromised individuals. Integrating optical fibers within the entire network of water distribution systems could effectively prevent (i) operational problems and (ii) health hazards associated with the growth of pathogenic organisms in piping. Ultraviolet-C side emitting optical fibers could light the way to new generation of sustainable water treatment technologies.

CHAPTER 8

CONCLUSIONS AND RECOMMENDATONS FOR FUTURE RESEARCH

This chapter summarizes the main conclusions and research answers from each chapter, and to provide recommendation for future work. The overarching research question for this dissertation was: **How can side emitting optical fibers enable visible through ultraviolet light driven processes to purify water.** Chapter two introduced three promising light driven processes that can significantly reduce the need of chemical additives for water purification. Visible light enables photosynthetic biological remediation and sustains chemotrophic aerobic remediation. Both visible and UV-AB light activates photocatalytic oxidative and reductive water treatment processes. Finally, UV-C light inactivates pathogenic microorganisms in plumbing.

Light propagation from one-point source such as the sun, LED or lamp is limited by optical obstructions in both the environment and reactors. Side emitting optical fibers can increase light distribution by > 1000 X from one-point source, but absorbance of UV light by conventional optical fibers limit their application to visible light only. I was the first to obtain UV-C side emission from optical fibers by placing nanoparticles on the surface of glass optical fibers. The nanoparticles induced side-emission via Mie scattering and interactions with evanescent wave. By tuning the separation distance between the nanoparticle and fiber surface we modulated the side emission of the optical fiber. Chapter 3-6 described how SEOFs in the visible through UV-C spectrum was fabricated and applied in water purification. The research questions and objective for each of these chapter is reinstated, and key conclusions are summarized below:

Objective I: Use a visible light SEOF to increase the oxygen level in a subsurface environment.

Chapter 3: Optical fiber-mediated photosynthesis for enhanced subsurface oxygen delivery

Research Question 1: What levels of dissolved oxygen can side emitting optical fibers enable in subsurface environments?

- The dissolved oxygen in the SEOF reactor reached supersaturation levels of > 15mg DO/L during light ON conditions creating oxidative zones.
- Polymer SEOF transported visible light to the subsurface at a dosage suitable to enhance phototrophic activity for biological remediation.
- Absorption of UV wavelengths by the core (~ 100%) limited the application of polymer optical fibers to visible light only.

Objective II: Fabricate a SEOF able to side emit visible through ultraviolet wavelengths of light.

Chapter 4: Particle-modified polymeric cladding on glass optical fibers enhances radial light scattering

Research Question 2: How can cladding modification increase side emission of UV light from silica core optical fibers?

- Suspending silica nanoparticles on conventional optical fiber polymer cladding induced side emission of UV-A light. A ~10 fold and ~95 fold increase in side emission flux was observed for the UV-A and visible light range respectively.
- Mie scattering was the primary mechanism of the increased flux of side emission with the 500 nm silica nanoparticles.

Research Question 3: Which material properties of optical fibers prevent side emission of UV-C light.

- UV-C light emission was limited by absorption of high frequency radiation by the polymer cladding. Scattering exponentially decreased, and attenuation exponentially increased for $\lambda < 350$ nm both with and without nanoparticle modification. This trend corresponded with the spectral absorption of H-C bonds present in most polymers. Polymers used in UV-C SEOFs should not have H-C bonds in the core polymeric chain.

Chapter 5: Nanoparticle and transparent polymer coatings enable UV-C side-emission optical fibers for microbial inactivation in water

Research Question 4: How can UV-C side emission form optical fibers be achieved to disinfect water.

- Aminated silica spheres attached to negatively charged glass optical fiber core enables UV-C side emission from high- OH optical fibers. Adding 400 nm silica spheres to the surface of the fiber core improved scattering 37-fold to 8.0 $\mu W/cm^2$.
- High ionic strength treatment can be used to tailor the proximity of the nanoparticle to the optical fiber core. Decrease in distance of nanoparticle and waveguide increased the fraction of light scattered per length of optical fiber. By increasing the ionic strength of the treatment solution, the scattering flux increased up to an additional 3.6 times to 36.9 $\mu W/cm^2$. At higher ionic strengths, the nanoparticle was closer to the optical fiber and therefore had higher interaction with the evanescent wave.

- Cytop^{TM} polymer served as a UV-C transparent optical fiber cladding. The cladding polymer Cytop^{TM} had negligible absorbance at 5 µm thickness which was illustrated by no change in the emission flux.
- The UV-C SEOF can be used for planktonic inactivation of *E. coli*. Attached to a 265 nm LED light source, the side-emitting optical fiber achieved 2.9 log inactivation of *E. coli* at a delivery dose of 14.5 mJ/cm^2.

<u>Objective III. Prevent growth of pathogenic bacteria on nutrient rich surface with a UV-C SEOF</u>

Chapter 6: Germicidal side emitting optical fibers enable surface inhibition of *Pseudomonas aeruginosa*

Research Question 5: What is the effectiveness of UV-C SEOF in preventing microbial surface growth.

- UV-C SEOF can prevent surface microbial growth on nutrient rich LB agar plates. One UV-C SEOF achieved ~2.9 cm inhibition of both *P. aeruginosa* and *E. coli.*
- Below a UV-C flux of ~2.3 µW/cm^2 the light flux limits the zone of inactivation by UV-C radiation. To assure full inactivation of *P. aeruginosa* and *E. coli*, it is crucial that the localized flux in the entire surface of interest is greater than ~2.3 µW/cm^2.

Recommendation for Future Research

My main contribution has been the fabrication of a UV-C side emitting optical fiber which has been published in journals and are a key part of a provisional patent. These fibers will enable technology developments for commercial applications in water treatment and biofilm prevention. This dissertation focuses on systematics modifications to the optical fibers as well as bench scale demonstrations and experiments for visible light bioremediation and UV-C microbial inhibition.

My work explains the science of UV-C SEOFs and proof of concept use of SEOF controlling planktonic and surface attached bacteria.

A lab scale reactor in Chapter 3 served as a demonstration for the fibers and showed that oxygen levels can be increased to > 15 mg/L and diverse microbial communities can be maintained near the zone of illumination. However, the degradation of a contaminant was not assessed. Further research should explore the potential of an optical fiber bio-barrier for degradation of hydrocarbons (i.e. toluene). If proven successful, visible light SEOF should be implemented in a large-scale passive biological remediation of contaminate soils and aquafers.

Although I successfully fabricated 30 cm lengths of 1 mm diameter SEOFs in the lab, longer (> 1 m) and thinner (< 300 um) optical fiber lengths are limited by the brittle nature of the glass. To fabricate longer fibers, the optical draw tower described in chapter 4 should be used. These draw towers allow for precision-controlled manufacturing of > 30 km length and < 300 um diameter optical fibers. The inline nature of the process allows the\ optical fiber core to be coated before it is handled, preventing breakage of the glass.

Side emitting optical fibers should be explored in preventing growth of complex biofilms in pipes. Figure 8-1 shows a conceptual schematic for a UV-C SEOF biofilm prevention experimental set up. This research would validate the potential to commercially install UV-C SEOFs to prevent biofilm formation and contamination of drinking water.

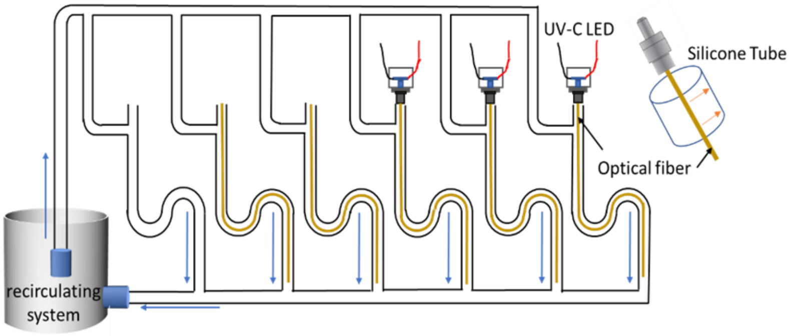

Figure 8-1 Schematic for recirculating pipe loop with six parallel 1 m lengths of silicon tubing.

My long-term vision is to integrate SEOFs in environmental systems, premise plumbing and reactors to provide a consistent dose of light to either enhance beneficial microbial communities or inhibit growth of pathogenic bacteria. These fibers have the potential to passively prevent water related infections in both developed and underdeveloped communities. Ultimately, side emitting optical fibers will light the way to a new generation of sustainable water treatment technologies.

REFERENCES

Abshire, R. L., & Dunton, H. (1981a). Resistance of selected strains of Pseudomonas aeruginosa to low-density ultraviolet radiation. *Applied and Environmental Microbiology*, *41*(6), 1419–1423.

Abshire, R. L., & Dunton, H. (1981b). Resistance of selected strains of Pseudomonas aeruginosa to low-intensity ultraviolet radiation. *Applied and Environmental Microbiology*, *41*(6), 1419–1423. Retrieved from http://www.ncbi.nlm.nih.gov/pubmed/6787985

Agrawal, G. P. (2010). *Fiber-Optic Communication Systems* (4th ed..). Hoboken: Wiley.

An, D., Chen, Y., Gu, B., Westerhoff, P., Hanigan, D., Herckes, P., … Atkinson, A. (2019). Lower molecular weight fractions of PolyDADMAC coagulants disproportionately contribute to N-nitrosodimethylamine formation during water treatment. *Water Research*, *150*, 466–472. https://doi.org/10.1016/j.watres.2018.12.002

Anderson, L. a, & Sarmiento, J. L. (1994). *data analysis ø o o I © observations*. *8*(1), 65–80.

Antopol, S. C., & Ellner, P. D. (1979). Susceptibility of Legionella pneumophila to ultraviolet radiation. *Applied and Environmental Microbiology*, *38*(2), 347–348. Retrieved from http://www.ncbi.nlm.nih.gov/pubmed/518088

Argyraki, A., Markvart, M., Bjørndal, L., Bjarnsholt, T., & Petersen, P. M. (2017). Inactivation of Pseudomonas aeruginosa biofilm after ultraviolet light-emitting diode treatment: a comparative study between ultraviolet C and ultraviolet B . *Journal of Biomedical Optics*, *22*(6), 065004. https://doi.org/10.1117/1.jbo.22.6.065004

Arie, A., Karoubi, R., Gur, Y. S., & Tur, M. (1986). Measurement and analysis of light transmission through a modified cladding optical fiber with applications to sensors. *Applied Optics*, *25*(11), 1754. https://doi.org/10.1364/AO.25.001754

Armstrong, J., Armstrong, W., & Beckett, P. . (1990). *Measurement and modeling of oxygen release f* (pp. 41–52). pp. 41–52. Oxford, United Kingdom: Pergamon Press.

Austin, D., Lohan, E., & Verson, E. (2003). Nitrification and Denitrification in a Tidal Vertical Flow Wetland Pilot. *Water Environment Technical Conference*, 1–25. Los Angeles.

Autin, O., Romelot, C., Rust, L., Hart, J., Jarvis, P., MacAdam, J., … Jefferson, B. (2013a). Evaluation of a UV-light emitting diodes unit for the removal of micropollutants in water for low energy advanced oxidation processes. *Chemosphere*, *92*(6), 745–751. https://doi.org/10.1016/j.chemosphere.2013.04.028

Autin, O., Romelot, C., Rust, L., Hart, J., Jarvis, P., MacAdam, J., … Jefferson, B. (2013b). Evaluation of a UV-light emitting diodes unit for the removal of micropollutants in water for low energy advanced oxidation processes. *Chemosphere*, *92*(6), 745–751. https://doi.org/10.1016/j.chemosphere.2013.04.028

Ballato, J., Hawkins, T., Foy, P., Stolen, R., Kokuoz, B., Ellison, M., … Powers, D. R. (2008). Silicon optical Fiber. *Optics Express*, *16*(23), 18675. https://doi.org/10.1364/OE.16.018675

Beck, S. E., Hull, N. M., Poepping, C., & Linden, K. G. (2018). Wavelength-Dependent Damage to Adenoviral Proteins Across the Germicidal UV Spectrum. *Environmental Science & Technology*, *52*(1), 223–229. https://doi.org/10.1021/acs.est.7b04602

Beck, S. E., Ryu, H., Boczek, L. A., Cashdollar, J. L., Jeanis, K. M., Rosenblum, J. S., … Linden, K. G. (2017). Evaluating UV-C LED disinfection performance and investigating potential dual-wavelength synergy. *Water Research*, *109*, 207–216. https://doi.org/10.1016/j.watres.2016.11.024

Beckers, M., Schlüter, T., Vad, T., Gries, T., & Bunge, C. A. (2015). An overview on fabrication methods for polymer optical fibers. *Polymer International*, *64*(1), 25–36. https://doi.org/10.1002/pi.4805

Behrends, L., Houke, L., Bailey, E., Jansen, P., & Brown, D. (2001). Reciprocating constructed wetlands for treating industrial, municipal and agricultural wastewater. *Water Science and Technology*, *44*(11–12), 399 LP – 405. Retrieved from http://wst.iwaponline.com/content/44/11-12/399.abstract

Bezbaruah, A., & Zhang, T. C. (2005). Quantification of oxygen release by bulrush (Scirpus validus) roots in constructed treatment wetland. *Biotechnology Bioengineering*, *89*(3), 308–318. https://doi.org/10.1002/bit.20332

Bichai, F., Barbeau, B., & Payment, P. (2009). Protection against UV disinfection of E. coli bacteria and B. subtilis spores ingested by C. elegans nematodes. *Water Research*, *43*(14), 3397–3406. https://doi.org/10.1016/j.watres.2009.05.009

Biology, E., & Sciences, E. (2007). TOWARD AN ECOLOGICAL CLASSIFICATION OF SOIL BACTERIA Edited by Foxit Reader. *Ecology*, *88*(6), 1354–1364. https://doi.org/10.1890/05-1839

Biyarin, A. M., Eronyan, M. A., Kulesh, A. Y., Meshkovskiy, I. k., Eutsky, A. L. A. R., Hcheglov, A. R. A. S., & Stinov, S. E. V. U. (2017). Light-emitting optical fibers with controllable anomalous small-angle scattering. *Journal of the Optical Society of America*, *34*(11), 2396–2399.

Blatchley, E. R., Dumoutier, N., Halaby, T. N., Levi, Y., & Laîné, J. M. (2001). Bacterial responses to ultraviolet irradiation. *Water Science and Technology : A Journal of the International Association on Water Pollution Research*, *43*(10), 179–186. Retrieved from http://www.ncbi.nlm.nih.gov/pubmed/11436779

Bohren, C. F. (Pennsylvania S. U. (1956). Handbook of Optics. In *Physical Review* (3rd ed., Vol. 104, pp. 811–815). https://doi.org/10.1103/PhysRev.104.811

Bohren, C. F., & Huffman, D. R. (2007). *Absorption and Scattering of Light by Small Particles*. John Wiley & Sons.

Bolton, J. R., Stefan, M. I., Shaw, P. S., & Lykke, K. R. (2011). Determination of the quantum yields of the potassium ferrioxalate and potassium iodide-iodate actinometers and a method for the calibration of radiometer detectors. *Journal of Photochemistry and Photobiology A: Chemistry*, *222*(1), 166–169. https://doi.org/10.1016/j.jphotochem.2011.05.017

Borde, X., Guieysse, B., Delgado, O., Muñoz, R., Hatti-Kaul, R., Nugier-Chauvin, C., … Mattiasson, B. (2003). Synergistic relationships in algal–bacterial microcosms for the treatment of aromatic pollutants. *Bioresource Technology*, *86*(3), 293–300. https://doi.org/10.1016/S0960-8524(02)00074-3

Branzei, D., & Foiani, M. (2008). Regulation of DNA repair throughout the cell cycle. *Nature Reviews Molecular Cell Biology*, *9*(4), 297–308. https://doi.org/10.1038/nrm2351

Brescia, P. (2012). *Micro-Volume Purity Assessment of Nucleic Acids using A 260 / A 280 Ratio and Spectral Scanning*.

Brown, M. A., Goel, A., & Abbas, Z. (2016). Effect of Electrolyte Concentration on the Stern Layer Thickness at a Charged Interface. *Angewandte Chemie - International Edition*, *55*(11), 3790–3794. https://doi.org/10.1002/anie.201512025

Buck, J. A. (2004). *Fundamentals of Optical Fibers* (Second; B. E. A. Saleh, Ed.). New Jersey: Wileyn.

Bunge, C.-A., Kruglov, R., & Poisel, H. (2006). Rayleigh and Mie scattering in polymer optical fibers. *Journal of Lightwave Technology*, *24*(8), 3137–3146. https://doi.org/10.1109/JLT.2006.878077

Butler, R. C., Lund, V., & Carlson, D. A. (1987). Susceptibility of Campylobacter jejuni and Yersinia enterocolitica to UV radiation. *Applied and Environmental Microbiology*, *53*(2), 375–378. Retrieved from http://www.ncbi.nlm.nih.gov/pubmed/3551844

Caporaso, J. G., Bittinger, K., Bushman, F. D., DeSantis, T. Z., Andersen, G. L., & Knight, R. (2010). PyNAST: a flexible tool for aligning sequences to a template alignment. *Bioinformatics (Oxford, England)*, *26*(2), 266–267. https://doi.org/10.1093/bioinformatics/btp636

Centers for Disease Control and Prevention. (n.d.-a). Leegionella.

Centers for Disease Control and Prevention. (n.d.-b). Pseudomonas aeruginosa in Healthcare Settings.

Cerniglia, C. E., Freeman, J. P., & Van Baalen, C. (1981). Biotransformation and toxicity of aniline and aniline derivatives in cyanobacteria. *Archives of Microbiology*, *130*(4), 272–275. https://doi.org/10.1007/BF00425939

Cervero-Aragó, S., Sommer, R., & Araujo, R. M. (2014). Effect of UV irradiation (253.7 nm) on free Legionella and Legionella associated with its amoebae hosts. *Water Research*, *67*, 299–309. https://doi.org/10.1016/j.watres.2014.09.023

Chandra, R., & Sobti, R. (2019). *Microbes for Sustainable Development and Bioremediation* (1st ed.).

Chang, J. C., Ossoff, S. F., Lobe, D. C., Dorfman, M. H., Dumais, C. M., Qualls, R. G., & Johnson, J. D. (1985). UV inactivation of pathogenic and indicator microorganisms. *Applied and Environmental Microbiology*, *49*(6), 1361–1365. Retrieved from http://www.ncbi.nlm.nih.gov/pubmed/2990336

Chapelle, F. H. (1999). Bioremediation of Petroleum Hydrocarbon-Contaminated Ground Water: The Perspectives of History and Hydrology. *Ground Water*, Vol. 37, pp. 122–132. https://doi.org/10.1111/j.1745-6584.1999.tb00965.x

Chatterley, C., & Linden, K. (2010a). Demonstration and evaluation of germicidal UV-LEDs for point-of-use water disinfection. *Journal of Water and Health*, *8*(3), 479–486. https://doi.org/10.2166/wh.2010.124

Chatterley, C., & Linden, K. (2010b). Demonstration and evaluation of germicidal UV-LEDs for point-of-use water disinfection. *Journal of Water and Health*, *8*(3), 479–486. https://doi.org/10.2166/wh.2010.124

Chen, J., Loeb, S., & Kim, J.-H. (2017a). LED revolution: fundamentals and prospects for UV disinfection applications. *Environ. Sci.: Water Res. Technol.*, *3*(2), 188–202. https://doi.org/10.1039/C6EW00241B

Chen, J., Loeb, S., & Kim, J.-H. (2017b). LED revolution: fundamentals and prospects for UV disinfection applications. *Environ. Sci.: Water Res. Technol.*, *3*(2), 188–202. https://doi.org/10.1039/C6EW00241B

Chen, T., Delgado, A. G., Yavuz, B. M., Proctor, A. J., Maldonado, J., Zuo, Y., … Rittmann, B. E. (2016). Ozone enhances biodegradability of heavy hydrocarbons in soil. *Journal of Environmental Engineering and Science*, *11*(1), 7–17. https://doi.org/10.1680/jenes.16.00002

Chevrefils, G., Caron, É., Wright, H., & Sakamoto, G. (2006). UV dose required to achieve incremental log inactivation of bacteria, protozoa and viruses. *IUVA News*, *8*(1), 38–45. Retrieved from http://uvsalesinfo.com/Documents/NavLink/UV_Destruction_Chart_uid7102009502412.pdf

Chew, H., Wang, D.-S., & Kerker, M. (2008). Elastic scattering of evanescent electromagnetic waves. *Applied Optics*, *18*(15), 2679. https://doi.org/10.1364/ao.18.002679

Chong, M. N., Jin, B., Chow, C. W. K., & Saint, C. (2010). Recent developments in photocatalytic water treatment technology: A review. *Water Research*, *44*(10), 2997–3027. https://doi.org/10.1016/j.watres.2010.02.039

Chu, P. L. (n.d.). FIBER OPTIC DEVICES AND SYSTEMS. In *Electrical Engineering*: *Vol. II*.

Clauß, M. (2006a). Higher effectiveness of photoinactivation of bacterial spores, UV resistant vegetative bacteria and mold spores with 222 nm compared to 254 nm wavelength. *Acta Hydrochimica et Hydrobiologica*, *34*(6), 525–532. https://doi.org/10.1002/aheh.200600650

Clauß, M. (2006b). Higher effectiveness of photoinactivation of bacterial spores, UV resistant vegetative bacteria and mold spores with 222 nm compared to 254 nm wavelength. *Acta Hydrochimica et Hydrobiologica*, *34*(6), 525–532. https://doi.org/10.1002/aheh.200600650

Clauß, M., Mannesmann, R., & Kolch, A. (2005). Photoreactivation ofEscherichia coli andYersinia enterolytica after Irradiation with a 222 nm Excimer Lamp Compared to a 254 nm Low-pressure Mercury Lamp. *Acta Hydrochimica et Hydrobiologica*, *33*(6), 579–584. https://doi.org/10.1002/aheh.200400600

Cleveland, C. C., & Liptzin, D. (2007). C:N:P stoichiometry in soil: Is there a “Redfield ratio” for the microbial biomass? *Biogeochemistry*, *85*(3), 235–252. https://doi.org/10.1007/s10533-007-9132-0

Collins, R. J., & Fan, H. Y. (1954). Infrared Lattice Absorption Bands in Germanium, Silicon, and Diamond. *Physical Review*, *93*(600), 674–677.

Cytop - Usage. (n.d.). Retrieved January 2, 2019, from https://www.agc-chemicals.com/jp/en/fluorine/products/detail/use/detail.html?uCode=JP-EN-F019_5

Delgado, A. G., Fajardo-Williams, D., Bondank, E., Esquivel-Elizondo, S., & Krajmalnik-Brown, R. (2017). Coupling Bioflocculation of Dehalococcoides mccartyi to High-Rate Reductive Dehalogenation of Chlorinated Ethenes. *Environmental Science and Technology*, *51*(19), 11297–11307. https://doi.org/10.1021/acs.est.7b03097

DeSantis, T. Z., Hugenholtz, P., Larsen, N., Rojas, M., Brodie, E. L., Keller, K., … Andersen, G. L. (2006). Greengenes, a chimera-checked 16S rRNA gene database and workbench compatible with ARB. *Applied and Environmental Microbiology*, *72*(7), 5069–5072. https://doi.org/10.1128/AEM.03006-05

Dixon, R., & Kahn, D. (2004). Genetic regulation of biological nitrogen fixation. *Nature Reviews Microbiology*, *2*(8), 621–631. https://doi.org/10.1038/nrmicro954

Donlan, R. M. (2001). Biofilm Formation: A Clinically Relevant Microbiological Process. *Clinical Infectious Diseases*, *33*(8), 1387–1392. https://doi.org/10.1086/322972

Dotson, A. D., Rodriguez, C. E., & Linden, K. G. (2012). UV disinfection implementation status in US water treatment plants. *Journal - American Water Works Association*, *104*(5). https://doi.org/10.5942/jawwa.2012.104.0075

Doudrick, K., Yang, T., Hristovski, K., & Westerhoff, P. (2013). Photocatalytic nitrate reduction in water: Managing the hole scavenger and reaction by-product selectivity. *Applied Catalysis B: Environmental*, *136–137*, 40–47. https://doi.org/10.1016/j.apcatb.2013.01.042

Douki, T. (2013). The variety of UV-induced pyrimidine dimeric photoproducts in DNA as shown by chromatographic quantification methods. *Photochemical & Photobiological Sciences*, *12*(8), 1286. https://doi.org/10.1039/c3pp25451h

Drinking-Water. (2018). Retrieved from https://www.who.int/news-room/fact-sheets/detail/drinking-water

Edgar, R. C. (2010). Search and clustering orders of magnitude faster than BLAST. *Bioinformatics (Oxford, England)*, *26*(19), 2460–2461. https://doi.org/10.1093/bioinformatics/btq461

Ehrenkranz, J. (2002). *Patent No. US 2002/0054744 A1*. https://doi.org/10.1037/t24245-000

Eischeid, A. C., & Linden, K. G. (2007). Efficiency of pyrimidine dimer formation in Escherichia coli across UV wavelengths. *Journal of Applied Microbiology*, *103*(5), 1650–1656. https://doi.org/10.1111/j.1365-2672.2007.03424.x

El-Bestawy, E. A., El-Salam, A. Z. A., & Mansy, A. E.-R. H. (2007). Potential use of environmental cyanobacterial species in bioremediation of lindane-contaminated effluents. *International Biodeterioration & Biodegradation*, *59*(3), 180–192. https://doi.org/10.1016/j.ibiod.2006.12.005

Esquivel, K., Arriaga, L. G., Rodríguez, F. J., Martínez, L., & Godínez, L. a. (2009). Development of a TiO2 modified optical fiber electrode and its incorporation into a photoelectrochemical reactor for wastewater treatment. *Water Research*, *43*(14), 3593–3603. https://doi.org/10.1016/j.watres.2009.05.035

Faulwetter, J. L., Gagnon, V., Sundberg, C., Chazarenc, F., Burr, M. D., Brisson, J.,Stein, O. R. (2009). Microbial processes influencing performance of treatment wetlands: A review. *Ecological Engineering*, *35*(6), 987–1004. https://doi.org/10.1016/j.ecoleng.2008.12.030

Fayngold, M. (n.d.). *Interactions Between Evanescent Photons and Environment Moses*. 1–24.

Fierer, N., & Jackson, J. (2005). Assessment of soil microbial community structure by use of taxon-specific quantitative PCR assays. *Applied and Environmental Microbiology*, *71*(7), 4117. https://doi.org/10.1128/AEM.71.7.4117

Filip, D. S., Thomas Peters, V., Dean Adams, E., & Middlebrooks, J. (1979). Residual heavy metal removal by an algae-intermittent sand filtration system. *Water Research*, *13*(3), 305–313. https://doi.org/10.1016/0043-1354(79)90211-2

Fujino, S. (2005). Fabrication of high-purity transparent silica glass by powder sintering method. *New Glass*, *20*(1), 19–24. Retrieved from f

Gagnon, V., Chazarenc, F., Comeau, Y., & Brisson, J. (2007). Influence of macrophyte species on microbial density and activity in constructed wetlands. *Water Science and Technology*, *56*(3), 249–254. https://doi.org/10.2166/wst.2007.510

Garner, E., McLain, J., Bowers, J., Engelthaler, D. M., Edwards, M. A., & Pruden, A. (2018). Microbial Ecology and Water Chemistry Impact Regrowth of Opportunistic Pathogens in Full-Scale Reclaimed Water Distribution Systems [Research-article]. *Environmental Science and Technology*, *52*(16), 9056–9068. https://doi.org/10.1021/acs.est.8b02818

Gayán, E., Mañas, P., Álvarez, I., & Condón, S. (2013). Mechanism of the synergistic inactivation of Escherichia coli by UV-C light at mild temperatures. *Applied and Environmental Microbiology*, *79*(14), 4465–4473. https://doi.org/10.1128/AEM.00623-13

Gehr, R. (2015). Comment on "UV Disinfection Induces a Vbnc State in Escherichia coli and Pseudomonas aeruginosa ." *Environmental Science & Technology*, *49*(12), 7501–7501. https://doi.org/10.1021/acs.est.5b00769

Ghiorse, W. C., & Wilson, J. T. (1988). Microbial Ecology of the Terrestrial Subsurface. *Advances in Applied Microbiology*, *33*(C), 107–172. https://doi.org/10.1016/S0065-2164(08)70206-5

Goldstein, S., & Rabani, J. (2008). The ferrioxalate and iodide-iodate actinometers in the UV region. *Journal of Photochemistry and Photobiology A: Chemistry*, *193*(1), 50–55. https://doi.org/10.1016/j.jphotochem.2007.06.006

Górska, P., Zaleska, A., Kowalska, E., Klimczuk, T., Sobczak, J. W., Skwarek, E., … Hupka, J. (2008). TiO2 photoactivity in vis and UV light: The influence of calcination temperature and surface properties. *Applied Catalysis B: Environmental*, *84*(3–4), 440–447. https://doi.org/10.1016/j.apcatb.2008.04.028

Green, M., Friedler, E., Ruskol, Y., & Safrai, I. (1997). Investigation of alternative method for nitrification in constructed wetlands. *Water Science and Technology*, *35*(5), 63–70. https://doi.org/http://dx.doi.org/10.1016/S0273-1223(97)00053-X

Gries, T., Seide, G., Beckers, M., Bunge, C.-A., & Shluter, T. (2017). Fabrication techniques for polymer optical fibres. In *Polymer Optical Fibers*. Elsevier Ltd.

Guo, M., Hu, H., Bolton, J. R., & El-Din, M. G. (2009). Comparison of low- and medium-pressure ultraviolet lamps: Photoreactivation of Escherichia coli and total coliforms in secondary effluents of municipal wastewater treatment plants. *Water Research*, *43*(3), 815–821. https://doi.org/10.1016/j.watres.2008.11.028

Haas, B. J., Gevers, D., Earl, A. M., Feldgarden, M., Ward, D. V, Giannoukos, G., … Birren, B. W. (2011). Chimeric 16S rRNA sequence formation and detection in Sanger and 454-pyrosequenced PCR amplicons. *Genome Research*, *21*(3), 494–504. https://doi.org/10.1101/gr.112730.110

Harris, G. D., Adams, V. D., Sorensen, D. L., & Curtis, M. S. (1987). Ultraviolet inactivation of selected bacteria and viruses with photoreactivation of the bacteria. *Water Research*, *21*(6), 687–692. https://doi.org/10.1016/0043-1354(87)90080-7

Hassen, A., Mahrouk, M., Ouzari, H., Cherif, M., Boudabous, A., & Damelincourt, J. J. (2000). UV disinfection of treated wastewater in a large-scale pilot plant and inactivation of selected bacteria in a laboratory UV device. *Bioresource Technology*, *74*(2), 141–150. https://doi.org/10.1016/S0960-8524(99)00179-0

Hatchard, C. G., & Parker, C. A. (1956). A New Sensitive Chemical Actinometer. II. Potassium Ferrioxalate as a Standard Chemical Actinometer. *Proceedings of the Royal Society A: Mathematical, Physical and Engineering Sciences*, *235*(1203), 518–536. https://doi.org/10.1098/rspa.1956.0102

Hess, A., Hohener, P., Hunkeler, D., & Zeyer, J. (1996). Bioremediation of a diesel fuel contaminated aquifer: Simulation studies in laboratory aquifer columns. *Journal of Contaminant Hydrology*, *23*(4), 329–345. https://doi.org/10.1016/0169-7722(95)00107-7

Hijnen, W. a M., Beerendonk, E. F., & Medema, G. J. (2006). Inactivation credit of UV radiation for viruses, bacteria and protozoan (oo)cysts in water: A review. *Water Research*, *40*(1), 3–22. https://doi.org/10.1016/j.watres.2005.10.030

Hoffmann, M. R., Martin, S. T., Choi, W., Bahnemann, D. W., & Bahnemannt, D. W. (1995). Environmental Applications of Semiconductor Photocatalysis Environmental Applications of Semiconductor Photocatalysis. *Society*, *95*(1), 69–96. https://doi.org/10.1021/cr00033a004

Hoyer, O. (1998). Testing performance and monitoring of UV systems for drinking water disinfection. *Water Supply*, *16*(1/2), 419–424.

Hu, J. Y., Chu, X. ., Quek, P. H., Feng, Y. ., & Tan, X. L. (2005). Repair and regrowth of Escherichia coli after low- and medium-pressure ultraviolet disinfection. *Water Science and Technology: Water Supply*, *5*(5), 101–108. https://doi.org/10.2166/ws.2005.0044

Hu, Y. (2005). A single TiO2-coated side-glowing optical fiber for photocatalytic wastewater treatment. *Chinese Science Bulletin*, *50*(18), 1979. https://doi.org/10.1360/982005-559

Hudzicki, J. (2009). Kirby-Bauer Disk Diffusion Susceptibility Test Protocol. In *American Society For Microbiology*. Retrieved from https://www.asm.org/Protocols/Kirby-Bauer-Disk-Diffusion-Susceptibility-Test-Pro

Jeanmonod, D. J., Rebecca, Suzuki, K. et al., Hrabovsky, M., Mariana Furio Franco Bernardes, M. P., & Lilian Cristina Pereira and Daniel Junqueira Dorta. (2011). Crystalline Silicon: Properties and Uses. In S. Basu (Ed.), *Intech* (pp. 135–171). https://doi.org/10.5772/32009

Jjemba, P., Johnson, W., Bukhari, Z., & LeChevallier, M. (2014). Review of the leading challenges in maintaining reclaimed water quality during storage and distribution. *Journal of Water Reuse and Desalination*, *4*(4), 209. https://doi.org/10.2166/wrd.2014.001

Jørgensen, B. B., Revsbech, N. P., Blackburn, T. H., & Cohen, Y. (1979). Diurnal cycle of oxygen and sulfide microgradients and microbial photosynthesis in a cyanobacterial mat sediment. *Applied and Environmental Microbiology*, *38*(1), 46–58.

Khan, F. I., Husain, T., & Hejazi, R. (2004). An overview and analysis of site remediation technologies. *Journal of Environmental Management*, *71*(2), 95–122. https://doi.org/10.1016/j.jenvman.2004.02.003

Klubben, W. S., Logunov, S. L., Fewkes, E. J., Mooney, J., Then, P. M., Wigley, P. G., … Ocampo, M. (2016, March 7). *Novel light diffusing fiber for use in medical applications* (I. Gannot, Ed.). https://doi.org/10.1117/12.2218267

Knudson, G. B. (1985). Photoreactivation of UV-irradiated Legionella pneumophila and other Legionella species. *Applied and Environmental Microbiology*, *49*(4), 975–980. Retrieved from http://www.ncbi.nlm.nih.gov/pubmed/4004227

Kooij, E. S., Martijn Brouwer, E. A., Wormeester, H., & Poelsema, B. (2002). Ionic strength mediated self-organization of gold nanocrystals: An AFM study. *Langmuir*, *18*(20), 7677–7682. https://doi.org/10.1021/la0257541

Korda, a., Santas, P., Tenente, a., & Santas, R. (1997). Petroleum hydrobcarbon bioremediation: Sampling and analytical techniques, in situ treatments and commercial microorganisms currently used. *Applied Microbiology and Biotechnology*, *48*(6), 677–686. https://doi.org/10.1007/s002530051115

Kundu, S., & Kelly, T. L. (2018). Improving the moisture stability of perovskite solar cells by using PMMA/P3HT based hole-transport layers. *Materials Chemistry Frontiers*, *2*(1), 81–89. https://doi.org/10.1039/C7QM00396J

Kuo, F.-S., Chien, Y.-H., & Chen, C.-J. (2012). Effects of light sources on growth and carotenoid content of photosynthetic bacteria Rhodopseudomonas palustris. *Bioresource Technology*, *113*, 315–318. https://doi.org/10.1016/j.biortech.2012.01.087

Lanzarini-Lopes, M., Cruz, B., Garcia-Segura, S., Alum, A., Abbaszadegan, M., & Westerhoff, P. (2019). Nanoparticle and Transparent Polymer Coatings Enable UV-C Side-Emission Optical Fibers for Inactivation of Escherichia coli in Water. *Environmental Science & Technology*, *53*(18), 10880–10887. https://doi.org/10.1021/acs.est.9b01958

Lanzarini-Lopes, M., Delgado, A. G., Guo, Y., Dahlen, P., & Westerhoff, P. (2018). Optical fiber-mediated photosynthesis for enhanced subsurface oxygen delivery. *Chemosphere*, *195*, 742–748. https://doi.org/10.1016/j.chemosphere.2017.12.089

Lanzarini-Lopes, M., Garcia-Segura, S., Hristovski, K., Messerly, M., Simon, A. J., & Westerhoff, P. (2019). Particle-modified polymeric cladding on glass optical fibers enhances radial light scattering. *Journal of the Optical Society of America B*, *36*(6), 1623. https://doi.org/10.1364/JOSAB.36.001623

Linden, K. G., Hull, N., & Speight, V. (2019). Thinking outside the treatment plant: UV for water distribution system disinfection: Published as part of the Accounts of Chemical Research special issue “water for Two Worlds: Urban and Rural Communities” [Research-article]. *Accounts of Chemical Research*, *52*, 1226–1233. https://doi.org/10.1021/acs.accounts.9b00060

Linden, K. G., Shin, G.-A., Lee, J.-K., Scheible, K., Shen, C., & Posy, P. (2009). Demonstrating 4-log adenovirus inactivation in a medium-pressure UV disinfection reactor. *Journal - American Water Works Association*, *101*(4), 90–99. https://doi.org/10.1002/j.1551-8833.2009.tb09876.x

Lines, M. E. (1984). The search for very low loss fiber-optic materials. *Science*, *226*(4675), 663–668. https://doi.org/10.1126/science.226.4675.663

Ling, L., Tugaoen, H., Brame, J., Sinha, S., Li, C., Schoepf, J., … Westerhoff, P. (2017). Coupling Light Emitting Diodes with Photocatalyst-Coated Optical Fibers Improves Quantum Yield of Pollutant Oxidation. *Environmental Science and Technology*, *51*(22), 13319–13326. https://doi.org/10.1021/acs.est.7b03454

Lu, J., Struewing, I., Yelton, S., & Ashbolt, N. (2015). Molecular survey of occurrence and quantity of Legionella spp., Mycobacterium spp., Pseudomonas aeruginosa and amoeba hosts in municipal drinking water storage tank sediments. *Journal of Applied Microbiology*, *119*(1), 278–288. https://doi.org/10.1111/jam.12831

Lui, G. Y., Roser, D., Corkish, R., Ashbolt, N. J., & Stuetz, R. (2016). Point-of-use water disinfection using ultraviolet and visible light-emitting diodes. *Science of the Total Environment*, *553*, 626–635. https://doi.org/10.1016/j.scitotenv.2016.02.039

Martín-Sómer, M., Pablos, C., van Grieken, R., & Marugán, J. (2017). Influence of light distribution on the performance of photocatalytic reactors: LED vs mercury lamps. *Applied Catalysis B: Environmental*, *215*, 1–7. https://doi.org/10.1016/j.apcatb.2017.05.048

Matafonova, G., & Batoev, V. (2018). Recent advances in application of UV light-emitting diodes for degrading organic pollutants in water through advanced oxidation processes: A review. *Water Research*, *132*, 177–189. https://doi.org/10.1016/j.watres.2017.12.079

Matthews, R. W. (1990). Purification of water with near-U.V. illuminated suspensions of titanium dioxide. *Water Research*, *24*(5), 653–660. https://doi.org/10.1016/0043-1354(90)90199-G

McEvoy, E., Wright, P. C., & Bustard, M. T. (2004). The effect of high concentration isopropanol on the growth of a solvent-tolerant strain of Chlorella vulgaris. *Enzyme and Microbial Technology*, *35*(2–3), 140–146. https://doi.org/10.1016/j.enzmictec.2004.01.012

McKinney, C. W., & Pruden, A. (2012). Ultraviolet Disinfection of Antibiotic Resistant Bacteria and Their Antibiotic Resistance Genes in Water and Wastewater. *Environmental Science & Technology*, *46*(24), 13393–13400. https://doi.org/10.1021/es303652q

Microbiome analysis laboratory. (n.d.). Retrieved March 5, 2017, from http://krajmalnik.environmentalbiotechnology.org/microbiome-lab.html

Mie Theory Calculator. (n.d.). Retrieved February 3, 2019, from https://nanocomposix.com/pages/mie-theory-calculator

Mitschke, F. (2009). *Fiber Optic: Physics and Technology* (1st ed.). New York: Springer Berlin Heidelberg.

Moné, M. J., Volker, M., Nikaido, O., Mullenders, L. H. F., van Zeeland, A. A., Verschure, P. J., … van Driel, R. (2001). Local UV-induced DNA damage in cell nuclei results in local transcription inhibition. *EMBO Reports*, *2*(11), 1013–1017. https://doi.org/10.1093/embo-reports/kve224

Mori, K., Ohya, H., Matsumoto, K., & Furune, H. (1987). Sunlight supply and gas exchange systems in microalgal bioreactor. *Advances in Space Research*, *7*(4), 47–52. https://doi.org/10.1016/0273-1177(87)90031-7

Mouagip. (n.d.). Pyrimidine dimer. Retrieved from https://commons.wikimedia.org/w/index.php?curid=11367690

Nebot Sanz, E., Salcedo Dávila, I., Andrade Balao, J. A., & Quiroga Alonso, J. M. (2007). Modelling of reactivation after UV disinfection: Effect of UV-C dose on subsequent photoreactivation and dark repair. *Water Research*, *41*(14), 3141–3151. https://doi.org/10.1016/j.watres.2007.04.008

Nieuwenhuijsen, M. J., Toledano, M. B., Eaton, N. E., Fawell, J., & Elliott, P. (2000). Chlorination disinfection byproducts in water and their association with adverse reproductive outcomes: a review. *Occupational and Environmental Medicine*, *57*(2), 73–85. https://doi.org/10.1136/oem.57.2.73

Nivala, J., Wallace, S., Headley, T., Kassa, K., Brix, H., van Afferden, M., & Müller, R. (2013). Oxygen transfer and consumption in subsurface flow treatment wetlands. *Ecological Engineering*, *61*, 544–554. https://doi.org/10.1016/j.ecoleng.2012.08.028

Nobbs, J. H. (1985). Kubelka—Munk Theory and the Prediction of Reflectance. *Review of Progress in Coloration and Related Topics*, *15*(1), 66–75. https://doi.org/10.1111/j.1478-4408.1985.tb03737.x

O’Neal, H., Garcia-segura, S., Hristovski, K., & Westerhoff, P. (2017). Challenges in photocatalytic reduction of nitrate as a water treatment technology. *Science of the Total Environment*, *599–600*, 1524–1551. https://doi.org/10.1016/j.scitotenv.2017.04.238

O’Neal Tugaoen, H., Garcia-Segura, S., Hristovski, K., & Westerhoff, P. (2018). Compact light-emitting diode optical fiber immobilized TiO 2 reactor for photocatalytic water treatment. *Science of The Total Environment*, *613–614*, 1331–1338. https://doi.org/10.1016/j.scitotenv.2017.09.242

Oguma, K., Katayama, H., Mitani, H., Morita, S., Hirata, T., & Ohgaki, S. (2001). Determination of Pyrimidine Dimers in Escherichia coli and Cryptosporidium parvum during UV Light Inactivation, Photoreactivation, and Dark Repair. *Applied and Environmental Microbiology*, *67*(10), 4630–4637. https://doi.org/10.1128/AEM.67.10.4630-4637.2001

Oguma, Kumiko, Katayama, H., & Ohgaki, S. (2004). Photoreactivation of Legionella pneumophila after inactivation by low- or medium-pressure ultraviolet lamp. *Water Research*, *38*(11), 2757–2763. https://doi.org/10.1016/j.watres.2004.03.024

Oguma, Kumiko, Kita, R., Sakai, H., Murakami, M., & Takizawa, S. (2013a). Application of UV light emitting diodes to batch and flow-through water disinfection systems. *Desalination*, *328*, 24–30. https://doi.org/10.1016/j.desal.2013.08.014

Oguma, Kumiko, Kita, R., Sakai, H., Murakami, M., & Takizawa, S. (2013b). Application of UV light emitting diodes to batch and flow-through water disinfection systems. *Desalination*, *328*, 24–30. https://doi.org/10.1016/j.desal.2013.08.014

Oldenburg, S. J. (Rice U. (1999). *Light scattering form gold nanoshells.pdf*.

Otaki, M., Okuda, A., Tajima, K., Iwasaki, T., Kinoshita, S., & Ohgaki, S. (2003). Inactivation differences of microorganisms by low pressure UV and pulsed xenon lamps. *Water Science and Technology : A Journal of the International Association on Water Pollution Research*, *47*(3), 185–190. Retrieved from http://www.ncbi.nlm.nih.gov/pubmed/12639027

Paul, E. a., & Clark, F. E. (1989a). Phosphorus Transformations in Soil. In *Soil Microbiology and Biochemistry*. https://doi.org/10.1016/B978-0-12-546805-3.50015-1

Paul, E. a., & Clark, F. E. (1989b). Soil as habitat for organisms and their reactions. *Soil Microbiology and Biochemistry*, 12–32. https://doi.org/10.1016/B978-0-12-546805-3.50005-9

Paul, E. a., & Clark, F. E. (1989c). Transformation of Nitrogen between the Organic and Inorganic Phase and to Nitrate. *Soil Microbiology and Biochemistry*, 131–146. https://doi.org/10.1016/B978-0-12-546805-3.50011-4

Peill, N J, & Hoffmann, M. (1997). Solar Powered photocatalytic Fiber-Optic Cable Reactor for Waste Stream Remediation. *Journal of Solar Energy Engineering*, *119*, 229–236. https://doi.org/10.1115/1.2888024

Peill, N J, & Hoffmann, M. (2015). *Solar-Powered Photocatalytic Fiber-Optic Cable Reactor for Waste Stream Remediation*. *1*(August 1997).

Peill, Nicola J., & Hoffmann, M. R. (1995). *Development and Optimization of a Ti02-Coated FiberiOptic Cable Photocatalytic Degradation of 4-Chlorophenol*. *29*(12), 2974–2981. https://doi.org/10.1021/es00012a013

Pinto, G., Pollio, A., Previtera, L., & Temussi, F. (2002). Biodegradation of phenols by microalgae. *Biotechnology Letters*, *24*(24), 2047–2051. https://doi.org/10.1023/A:1021367304315

Poepping, C., Beck, S. E., Wright, H., & Linden, K. G. (2014). Evaluation of DNA damage reversal during medium-pressure UV disinfection. *Water Research*, *56*, 181–189. https://doi.org/10.1016/j.watres.2014.02.043

Prieve, D. C., & Walz, J. Y. (2009). Scattering of an evanescent surface wave by a microscopic dielectric sphere. *Applied Optics*, *32*(9), 1629. https://doi.org/10.1364/ao.32.001629

Qiu, X., Sundin, G. W., Chai, B., & Tiedje, J. M. (2004). Survival of Shewanella oneidensis MR-1 after UV radiation exposure. *Applied and Environmental Microbiology*, *70*(11), 6435–6443. https://doi.org/10.1128/AEM.70.11.6435-6443.2004

Quek, P. H., & Hu, J. (2008). Indicators for photoreactivation and dark repair studies following ultraviolet disinfection. *Journal of Industrial Microbiology and Biotechnology*, *35*(6), 533–541. https://doi.org/10.1007/s10295-008-0314-0

Rastogi, R. P., Richa, Kumar, A., Tyagi, M. B., & Sinha, R. P. (2010). Molecular Mechanisms of Ultraviolet Radiation-Induced DNA Damage and Repair. *Journal of Nucleic Acids*, *2010*, 1–32. https://doi.org/10.4061/2010/592980

Rattanakul, S., & Oguma, K. (2018a). Inactivation kinetics and efficiencies of UV-LEDs against Pseudomonas aeruginosa, Legionella pneumophila, and surrogate microorganisms. *Water Research*, *130*, 31–37. https://doi.org/10.1016/j.watres.2017.11.047

Rattanakul, S., & Oguma, K. (2018b). Inactivation kinetics and efficiencies of UV-LEDs against Pseudomonas aeruginosa, Legionella pneumophila, and surrogate microorganisms. *Water Research*, *130*, 31–37. https://doi.org/10.1016/j.watres.2017.11.047

Rattanakul, S., Oguma, K., Sakai, H., & Takizawa, S. (2014). Inactivation of Viruses by Combination Processes of UV and Chlorine. *Journal of Water and Environment Technology*, *12*(6), 511–523. https://doi.org/10.2965/jwet.2014.511

Rawson, E G. (1974). Analysis of scattering from fiber waveguides with irregular core surfaces. *Applied Optics*, *13*(10), 2370–2377. https://doi.org/10.1364/AO.13.002370

Rawson, Eric G. (1972). Measurement of the Angular Distribution of Light Scattered from a Glass Fiber Optical Waveguide. *Appl. Opt.*, *11*(11), 2477–2481. https://doi.org/10.1364/AO.11.002477

Rippka, R., Deruelles, J., Waterbury, J. B., Herdman, M., & Stanier, R. Y. (1979). Generic Assignments, Strain Histories and Properties of Pure Cultures of Cyanobacteria. *Journal of General Microbiology*, *111*(1), 1–61. https://doi.org/10.1099/00221287-111-1-1

Rodríguez, R. A., Bounty, S., & Linden, K. G. (2013). Long-range quantitative PCR for determining inactivation of adenovirus 2 by ultraviolet light. *Journal of Applied Microbiology*, *114*(6), 1854–1865. https://doi.org/10.1111/jam.12169

Roos, a, & Ribbing, C. G. (1988). Interpretation of integrating sphere signals for non-Lambertian samples. *Applied Optics*, *27*(18), 3833–3837.

Santoro, D., Crapulli, F., Turolla, A., & Antonelli, M. (2017). Detailed modeling of oxalic acid degradation by UV-TiO 2 nanoparticles: Importance of light scattering and photoreactor scale-up. *Water Research*, *121*, 361–373. https://doi.org/10.1016/j.watres.2017.05.007

Satoh, S., Susa, K., & Matsuyama, I. (1999). Simple method of measuring scattering losses in optical fibers. *Applied Optics*, *38*(34), 7080–7084. https://doi.org/10.1364/AO.38.007080

Schalk, S., Adam, V., Arnold, E., Brieden, K., Voronov, A., & Witzke, H. (2005). UV-Lamps for Disinfection and Advanced Oxidation - Lamp Types, Technologies and Applications. *IUVA News*, *8*(1), 32–37. Whistler, BC, Canada.

Shin, G.-A., Lee, J.-K., Freeman, R., & Cangelosi, G. A. (2008). Inactivation of Mycobacterium avium Complex by UV Irradiation. *Applied and Environmental Microbiology*, *74*(22), 7067–7069. https://doi.org/10.1128/AEM.00457-08

Sholtes, K. A., Lowe, K., Walters, G. W., Sobsey, M. D., Linden, K. G., & Casanova, L. M. (2016). Comparison of ultraviolet light-emitting diodes and low-pressure mercury-arc lamps for disinfection of water. *Environmental Technology*, *37*(17), 2183–2188. https://doi.org/10.1080/09593330.2016.1144798

Sinha, R. P., & Häder, D.-P. (2002). UV-induced DNA damage and repair: a review. *Photochemical & Photobiological Sciences*, *1*(4), 225–236. https://doi.org/10.1039/b201230h

Sommer, R, Lhotsky, M., Haider, T., & Cabaj, A. (2000). UV inactivation, liquid-holding recovery, and photoreactivation of Escherichia coli O157 and other pathogenic Escherichia coli strains in water. *Journal of Food Protection*, *63*, 202–2030.

Sommer, R, Pribil, W., Appelt, S., Gehringer, P., Eschweiler, H., Leth, H., … Haider, T. (2001). Inactivation of bacteriophages in water by means of non-ionizing (UV-253.7 nm) and ionizing (gamma) radiation: a comparative approach. *Water Research*, *35*(13), 3109–3116. https://doi.org/10.1016/s0043-1354(01)00030-6

Sommer, Regina, Haider, T., Cabaj, A., Pribil, W., & Lhotsky, M. (1998). Time dose reciprocity in UV disinfection of water. *Water Science and Technology*, *38*(12). https://doi.org/10.1016/S0273-1223(98)00816-6

Song, K., Mohseni, M., & Taghipour, F. (2016). Application of ultraviolet light-emitting diodes (UV-LEDs) for water disinfection: A review. *Water Research*, *94*, 341–349. https://doi.org/10.1016/j.watres.2016.03.003

Spigulis, J. (2005). Application prospects of silica core side-glowing optical fibers. *Optical Fibers: Applications*, *5952*(September 2005), 595203. https://doi.org/10.1117/12.622112

Spigulis, J., Pfafrods, D., Stafeckis, M., & Jelinska-Platace, W. (1997). Glowing optical fiber design and parameters. *Optical Inorganic Dielectric Materials and Devices*, *2967*(2), 231–236. https://doi.org/10.1117/12.266542

Stoddart, A. K., & Gagnon, G. A. (2019). *Development of a standard protocol for the treatment of Pseudomonas aeruginosa biofilms with an UVC-LED collimated beam apparatus* .

Tanner, C C, & Kadlec, R. H. (2003). Oxygen flux implications of observed nitrogen removal rates in subsurface-flow treatment wetlands. *Water Science and Technology*, *48*(5), 191 LP – 198. Retrieved from http://wst.iwaponline.com/content/48/5/191.abstract

Tanner, Chris C., D'Eugenio, J., McBride, G. B., Sukias, J. P. S., & Thompson, K. (1999). Effect of water level fluctuation on nitrogen removal from constructed wetland mesocosms. *Ecological Engineering*, *12*(1–2), 67–92. https://doi.org/10.1016/S0925-8574(98)00055-X

Tekelioglu, M., & Wood, B. D. (2009). Solar light transmission of polymer optical fibers. *Solar Energy*, *83*(11), 2039–2049. https://doi.org/10.1016/j.solener.2009.08.002

Templeton, M. R., Oddy, F., Leung, W., & Rogers, M. (2009). Chlorine and UV disinfection of ampicillin-resistant and trimethoprim-resistant Escherichia coli A paper submitted to the Journal of Environmental Engineering and Science. *Canadian Journal of Civil Engineering*, *36*(5), 889–894. https://doi.org/10.1139/L09-040

Terruzy, L., Frigerio, S., & Villani, G. (2012). *Patent No. US 2012/0321265 A1*. https://doi.org/10.1016/j.(73)

Tester, M., & Morris, C. (1987). The penetration of light through soil. *Plant, Cell & Environment*, *10*(4), 281–286. https://doi.org/10.1111/j.1365-3040.1987.tb01607.x

Tosa, K., & Hirata, T. (1999a). Photoreactivation of enterohemorrhagic Escherichia coli following UV disinfection. *Water Research*, *33*(2), 361–366. https://doi.org/10.1016/S0043-1354(98)00226-7

Tosa, K., & Hirata, T. (1999b). Photoreactivation of enterohemorrhagic Escherichia coli following UV disinfection. *Water Research*, *33*(2), 361–366. https://doi.org/10.1016/S0043-1354(98)00226-7

Tugaoen, H. O. N., Herckes, P., Hristovski, K., & Westerhoff, P. (2018). Influence of ultraviolet wavelengths on kinetics and selectivity for N-gases during TiO2 photocatalytic reduction of nitrate. *Applied Catalysis B: Environmental*, *220*(August 2017), 597–606. https://doi.org/10.1016/j.apcatb.2017.08.078

Umar, M., & Abdul, H. (2013). Photocatalytic Degradation of Organic Pollutants in Water. In *Organic Pollutants - Monitoring, Risk and Treatment*. https://doi.org/10.5772/53699

USEPA. (2002). Summary for Policymakers. In Intergovernmental Panel on Climate Change (Ed.), *Climate Change 2013 - The Physical Science Basis* (pp. 1–30). https://doi.org/10.1017/CBO9781107415324.004

Valderrama, L. T., Del Campo, C. M., Rodriguez, C. M., de- Bashan, L. E., & Bashan, Y. (2002). Treatment of recalcitrant wastewater from ethanol and citric acid production using the microalga Chlorella vulgaris and the macrophyte Lemna minuscula. *Water Research*, *36*(17), 4185–4192. https://doi.org/10.1016/S0043-1354(02)00143-4

Van De Hulst, H. C. (1957). *Light Scattering by Small Particles* (First). John Wiley & Sons, Inc, N.Y.

Vanysacker, L., Denis, C., Declerck, P., Piasecka, A., & Vankelecom, I. F. J. (2013). Microbial adhesion and biofilm formation on microfiltration membranes: A detailed characterization using model organisms with increasing complexity. *BioMed Research International*, *2013*. https://doi.org/10.1155/2013/470867

Wang, F., Shimazaki, A., Yang, F., Kanahashi, K., Matsuki, K., Miyauchi, Y., … Matsuda, K. (2017). Highly efficient and stable perovskite solar cells by interfacial engineering using solution-processed polymer layer. *Journal of Physical Chemistry C*, *121*(3), 1562–1568. https://doi.org/10.1021/acs.jpcc.6b12137

Water Quality Factors Reference Unit. (n.d.). *Percentage Saturation of Dissolved Oxygen*. Retrieved from http://www.hach.com/hc/view.file.invoker/2687600/View=FILCAT_WATER_WATER_EVERYWHERE_SERIES

Wilson, B. (1992). Coliphage MS-2 as a UV Water Disinfection Efficacy Test Surrogate for Bacterial and Viral Pathogens. *AWWA Water Quality Technology Conference*, 219–235. https://doi.org/10013116305

Wilson, B. R., Roessler, P. F., Van Dellen, E., Abbaszadegan, M., & Gerba, C. P. (1992). Coliphage MS2 as a UV water disinfection efficacy test surrogate for bacterial and viral pathogens. *American Water Works Association*. Toronto.

Wo, A., Fewkes, E. J., & Lvovich, S. (2017). *Patent No. WO2014121172A2*.

Wu, D., You, H., Zhang, R., Chen, C., & Lee, D.-J. (2011). Ballast waters treatment using UV/Ag–TiO2+O3 advanced oxidation process with Escherichia coli and Vibrio alginolyticus as indicator microorganisms. *Chemical Engineering Journal*, *174*(2–3), 714–718. https://doi.org/10.1016/j.cej.2011.09.087

Wu, M. J., Bak, T., Doherty, P. J. O., Moffitt, M. C., Nowotny, J., Bailey, T. D., & Kersaitis, C. (2014). Photocatalysis of Titanium Dioxide for Water Disinfection : Challenges and Future Perspectives. *International Journal of Photochemistry*, *2014*.

Wu, S., Jeschke, C., Dong, R., Paschke, H., Kuschk, P., & Knöller, K. (2011). Sulfur transformations in pilot-scale constructed wetland treating high sulfate-containing contaminated groundwater: A stable isotope assessment. *Water Research*, *45*(20), 6688–6698. https://doi.org/10.1016/j.watres.2011.10.008

Wu, Y., Clevenger, T., & Deng, B. (2005). Impacts of Goethite Particles on UV Disinfection of Drinking Water. *Applied and Environmental Microbiology*, *71*(7), 4140–4143. https://doi.org/10.1128/AEM.71.7.4140-4143.2005

Xu, J., Ao, Y., Fu, D., Lin, J., Lin, Y., Shen, X., … Yin, Z. (2008a). Photocatalytic activity on TiO2-coated side-glowing optical fiber reactor under solar light. *Journal of Photochemistry and Photobiology A: Chemistry*, *199*(2–3), 165–169. https://doi.org/10.1016/j.jphotochem.2008.05.019

Xu, J., Ao, Y., Fu, D., Lin, J., Lin, Y., Shen, X., … Yin, Z. (2008b). Photocatalytic activity on TiO2-coated side-glowing optical fiber reactor under solar light. *Journal of Photochemistry and Photobiology A: Chemistry*, *199*(2–3), 165–169. https://doi.org/10.1016/j.jphotochem.2008.05.019

Xue, S., Zhang, Q., Wu, X., Yan, C., & Cong, W. (2013). A novel photobioreactor structure using optical fibers as inner light source to fulfill flashing light effects of microalgae. *Bioresource Technology*, *138*, 141–147. https://doi.org/10.1016/j.biortech.2013.03.156

Yang, T., Doudrick, K., & Westerhoff, P. (2013). Photocatalytic reduction of nitrate using titanium dioxide for regeneration of ion exchange brine. *Water Research*, *47*(3), 1299–1307. https://doi.org/10.1016/j.watres.2012.11.047

Yang, Y., Xiang, Y., Xia, C., Wu, W. M., Sun, G., & Xu, M. (2014). Physiological and electrochemical effects of different electron acceptors on bacterial anode respiration in bioelectrochemical systems. *Bioresource Technology*, *164*, 270–275. https://doi.org/10.1016/j.biortech.2014.04.098

Yaun, B. R., Sumner, S. S., Eifert, J. D., & Marcy, J. E. (2003). Response of Salmonella and Escherichia coli O157:H7 to UV Energy. *Journal of Food Protection*, *66*(6), 1071–1073. https://doi.org/10.4315/0362-028X-66.6.1071

Zhao, C., Ye, L., Ge, J., Zou, J., & Yu, X. (2013). Novel light-leaking optical fiber liquid-level sensor for aircraft fuel gauging. *Optical Engineering*, *52*(1), 014402. https://doi.org/10.1117/1.oe.52.1.014402

Zhao, C., Ye, L., Yu, X., & Ge, J. (2012). Continuous Fuel Level Sensor Based on Spiral Side-Emitting Optical Fiber. *Journal of Control Science and Engineering*, *2012*, 1–8. https://doi.org/10.1155/2012/267519

Zhi, W., Guobin, R., Shuqin, L., & Shuisheng, J. (2003). Loss properties due to Rayleigh scattering in different types of fiber. *Optics Express*, *11*(1), 39–47. https://doi.org/10.1364/OE.11.000039

Zhu, T., & Sikora, F. J. (1995). Ammonium and nitrate removal in vegetated and unvegetated gravel bed microcosm wetlands. *Water Science and Technology*, *32*(3), 219–228. https://doi.org/http://dx.doi.org/10.1016/0273-1223(95)00623-0

Zimmer, J. L., & Slawson, R. M. (2002). Potential repair of Escherichia coli DNA following exposure to UV radiation from both medium- and low-pressure UV sources used in drinking water treatment. *Applied and Environmental Microbiology*, *68*(7), 3293–3299. https://doi.org/10.1128/aem.68.7.3293-3299.2002

Zonyl ^{TM} MP 1200. (2015).

Zubia, J., & Arrue, J. (2001). Plastic Optical Fibers: An Introduction to Their Technological Processes and Applications. *Optical Fiber Technology 7*, 101–140.

APPENDIX A

ELECTRICAL ENERGY PER ORDER AND CURRENT EFFICIENCY FOR ELECTROCHEMICAL OXIDATION OF P-CHLOROBENZOIC ACID WITH BORON-DOPED DIAMOND ANODE.

Text from: Lanzarini-Lopes, M., Garcia-Segura, S., Hristovski, K., Westerhoff, P. Electrical energy per order and current efficiency for electrochemical oxidation of p-chlorobenzoic acid with boron-doped diamond anode. *Chemosphere*, 2017 188:304-311.Figures included at the end of the chapter.

Abstract

Electrochemical oxidation (EO) is an advanced oxidation process for water treatment to mineralize organic contaminants. While proven to degrade a range of emerging pollutants in water, less attention has been given to quantify the effect of operational variables such applied current density and pollutant concentration on efficiency and energy requirements. Particular figures of merit were mineralization current efficiency (MCE) and electrical energy per order (E_{EO}). Linear increases of applied current exponentially decreased the MCE due to the enhancement of undesired parasitic reactions that consumed generated hydroxyl radical. E_{EO} values ranged from 39.3 to 331.8 kWh m^{-3} $order^{-1}$. Increasing the applied current also enhanced the E_{EO} due to the transition from kinetics limited by current to kinetics limited by mass transfer. Further increases in current did not influence the removal rate, but it raised the E_{EO} requirement. The E_{EO} requirement diminished when decreasing initial pollutant loading with the increase of the apparent kinetic rate because of the relative availability of oxidant per pollutant molecule in solution at a defined current. Oxidation by-products released were identified, and a plausible degradative pathway has been suggested.

Introduction

Contaminants of emerging concern (CECs) such pharmaceuticals and pesticides are detected at concentrations ranging from ng L^{-1} up to mg L^{-1} in water sources (Baalbaki et al., 2017; Glassmeyer et al., 2017). Even though these concentrations appear to be low, the chemicals present features that induce water quality changes (Naidu et al., 2016). Recent reports demonstrate that even low CEC concentrations could cause toxicity, carcinogenicity and mutagenicity among other hazardous undesired effects on humans and ecosystems (Bolong et al., 2009; Akoto et al., 2015; Benson et al., 2017). Conventional water treatment technologies show low removal efficiencies for polar CECs, with exception of advanced oxidation processes (AOPs) (Klancar et al., 2016). In this frame, electrochemical advanced oxidation processes (EAOPs) have received great attention because they completely mineralize organic compounds (Brillas and Martínez-Huitle, 2015; Garcia-Segura and Brillas, 2017). Electrochemical oxidation (EO) is an effective EAOP for remediating wastewaters polluted by organic CECs (Martínez-Huitle et al. 2015). In EO, hydroxyl radical ($^{\bullet}OH$) is electrogenerated *in-situ* from water via reaction (1) by using high oxygen evolution overpotential anodes (Panizza and Cerisola, 2009).

$$H_2O + e^- \rightarrow {}^{\bullet}OH + H^+ \qquad (1)$$

The $^{\bullet}OH$ radical is a highly oxidative species ($E^o({}^{\bullet}OH/H_2O)$ = 2.80 V/SHE) that non-selectively reacts with organic pollutants until their complete mineralization to CO_2, H_2O and inorganic ions. This heterogeneous reaction occurs at the surface of the anode. Boron-doped diamond (BDD) thin-film electrodes are the most promising anodes for EO water treatment applications (Garcia-Segura et al., 2011; Garcia-Segura et al., 2015a) due to their greater oxidation power when compared to other conventional non-active anode materials such as Pt, PbO_2 or SnO_2 (Pereira et al., 2015; Fajardo et al., 2017). Even though research is increasing on the fundamental understanding of EAOPs to treat pharmaceuticals (Antonin et al., 2015; García-Montoya et al., 2015), pesticides (Madsen et al., 2014; Souza et al., 2016), dyes (Solano et al., 2015; Isarain-Chávez et al., 2017) and wastewater effluents (Moreira et al., 2017), there is still a lack of knowledge on the correlation between EO performance and the cost-effective application of electrochemical technologies.

This research studied the correlation between electrical energy per order (E_{EO}), mineralization current efficiency (MCE) and EO process performance under different operational conditions, including applied current density and initial pollutant concentration. These parameters could demonstrate the feasibility of implementing electrochemical technologies into market and become a tool for comparing performance between different EAOPs. The highly persistent pollutant *para*-chlorobenzoic acid (pCBA) was selected as a representative polar organic model of highly carcinogenic chlorinated organic pollutants, similar to several pesticides used worldwide (Kim et al., 2017). The EO performance was analyzed in terms of dissolved organic carbon (DOC) abatement and degradation kinetics followed by liquid chromatography. The formation of aromatic by-products, carboxylic acids and chlorine ionic species was also analyzed, and a plausible degradative pathway has been suggested.

Experimental methods

Chemicals

Pure *p*-chlorobenzoic acid (99%) was purchased from Sigma-Aldrich. Analytical-grade sodium sulfate (from Sigma-Aldrich) was used as the supporting electrolyte. Hydroquinone, benzoquinone, 4-chlorophenol, 4-hydroxybenzoic acid and other carboxylic acids used as standards were also purchased from Sigma-Aldrich. Inorganic sodium salts of chloride, chlorate and perchlorate purchased from Fisher Chemicals and Sigma-Aldrich were used as ionic chromatography standards. All solutions and mobile phases were prepared with nano-pure water obtained from a Millipore Milli-Q system with resistivity >18.2 MΩ cm at 25 ºC. Acetonitrile used in the preparation of mobile phases was of HPLC grade purchased from Sigma-Aldrich. Solutions were adjusted to pH 6.0 with analytical grade sulfuric acid and/or sodium hydroxide from Fisher Chemicals.

Electrochemical System

100 mL aliquots of 0.3–2.4 mM of pCBA solutions (corresponding to 25–200 mg L^{-1} of DOC) were treated by EO at pH 6.0 with 0.05 M of Na_2SO_4 as the supporting electrolyte. The EO experiments were carried out in an open, undivided cylindrical glass cell at 25 ºC. Experiments were conducted under magnetic stirring at 700 rpm to ensure homogenization and reactant transport towards/from the electrode surfaces. The cell was equipped with a 3 cm^2 BDD thin film anode from NeoCoat (La Chaux-de-Fonds, Switzerland) and a 3 cm^2 Pt sheet as cathode. The interelectrode gap was 1 cm. The applied current density ranged between 16.6 mA cm^{-2} and 100.0 mA cm^{-2}.

Analytical Procedures

The pH of the solutions was measured using a Thermo Scientific Orion Star A221 pH-meter. Aliquots were withdrawn during electrolysis and analyzed. The mineralization of the solution was monitored for DOC abatement with a Shimadzu VCSN TOC analyzer, which obtained reproducible values with an accuracy of 1%. Assuming overall pCBA mineralization yielding CO_2 and Cl^- as final products via reaction (2), the MCE was estimated from Eq. (3) (Brillas and Martínez-Huitle, 2015; Ridruejo et al., 2017):

$$C_7O_2H_5Cl + 12\ H_2O \rightarrow 7\ CO_2 + 29\ H^+ + Cl^- + 28\ e^- \tag{2}$$

$$\%\ \mathrm{MCE} = \frac{nFVs\ \Delta(\mathrm{DOC})_{exp}}{4.32\ X\ 10^7 mIt} \tag{3}$$

where *n* is the number of electrons consumed per pCBA molecule (28 mol), *F* is the Faraday constant (96487 C mol^{-1}), V_s is the solution volume (L), $\Delta(\mathrm{DOC})_{\mathrm{exp}}$ is the experimental solution DOC decay (mg L^{-1}), 4.32 x 10^7 is a conversion factor for units (3600 s h^{-1} x 12,000 mg mol^{-1}), *m* is the number of carbon atoms of pCBA, *I* is the applied current (A) and *t* is the electrolysis time (h). The energy consumption per unit of DOC mass required to reduce organic load was estimated from Eq. (4) (Cruz-Rizo et al., 2017; Garcia-Segura and Brillas, 2016):

$$\mathrm{EC\ (kWh\ g^{-1})\ DOC} = \frac{E_{cell}It}{Vs\Delta(\mathrm{DOC})_{exp}} \tag{4}$$

where E_{cell} is the average cell potential (V). Note that both MCE and EC can be estimated for the organic load reduction in one order of magnitude in DOC.

Reversed-phase chromatography allowed measuring pCBA degradation and its transformation to aromatic by-products. Sample aliquots of 20 µL were injected in a Waters 2695 HPLC with a Waters 2996 Photodiode Array detector, fitted with a Waters

LiChrosorb® 10 µm RP18 (100 mm x 4.6 mm) column at 25 ºC and a LiChroCART® 4-4 guard column. A 35:65 (v/v) acetonitrile/water mixture at 0.6 ml min^{-1} was used as mobile phase. The pCBA decay followed pseudo-first order reaction kinetics with rate constants (k_1) determined in s^{-1}. The E_{EO} was used as a figure of merit to determine the electric energy required by EO required to reduce pCBA concentration by one order of magnitude in a unit volume calculated from Eq. (5) for batch operation mode (Bolton et al., 2001; Hurwitz et al., 2014):

$$\mathrm{EEO}\ (\mathrm{kWh\ m^{-3} order^{-1}}) = \frac{E_{cell} I t}{Vs \log(C0/Cf)} \quad (5)$$

where c_0 and c_f correspond to the initial and final concentration after one order of magnitude reduction. However, this expression can be simplified assuming first-order kinetics according to Eq. (6) because $\log(c_0/c_f) = 0.4343\ k_1 t$.

$$\mathrm{EEO}\ (\mathrm{kWh\ m^{-3} order^{-1}}) = \frac{6.39\ X\ 10^{-4}\ E_{cell} I}{Vs\ \mathrm{k}_1} \quad 6)$$

where 6.39 is a conversion factor (1 h / 3600 s / 0.4343) and k_1 is the pseudo-first order rate constant (s^{-1}).

Carboxylic acids, yielded from the aromatic ring cleavage during pCBA degradation, were identified and quantified by ion-exclusion chromatography using the above HPLC fitted with a Bio-Rad Amnex HPX87H (300 mm x 7.8 mm) column at 35 ºC with a 4.0 mM H_2SO_4 mobile phase at 0.6 mL min^{-1}. Inorganic ions released during the mineralization process were quantified by ionic chromatography using a Thermo Dionex ICS-5000DC coupled to a conductivity detector AERS 500 fitted with a high capacity hydroxide-selective anion-exchange column Dionex Ionpac AS18 (2 mm x 250 mm) flowing 30 mM KOH solution as mobile phase at 0.25 mL min^{-1}.

Results and discussion

Influence Of Applied Current Density On Treatment Efficiency

Applied current density (*j*) is the operational variable that controls the EO electrokinetics because it defines the amount of $^{\bullet}OH$ electrogenerated *in situ* according to reaction (1). Figure A-1 shows the influence of *j* on the EO treatment of pCBA solutions. DOC removal increased gradually as *j* increased (Figure A-1a); 79.8%, 87.0%, 96.5% and 98.4% of DOC was removed from solution after 360 min of EO treatment at 16.6 mA cm^{-2}, 33.3 mA cm^{-2}, 66.6 mA cm^{-2} and 100.0 mA cm^{-2}, respectively. This trend can be explained by the increase in $^{\bullet}OH$ production, which accelerates the mineralization rate. However, opposite behavior was observed for the calculated MCE from equation (3) (cf. inset panel Figure A-1a). The current efficiency dropped from 30.8% for 16.6 mA cm^{-2} down to 4.8% for 100.0 mA cm^{-2}. At higher *j*, oxygen evolution reaction from water oxidation (equation 7) is enhanced, which competitively consumes the excess electrons. Even though higher *j* electrogenerates more $^{\bullet}OH$, unreacted $^{\bullet}OH$ radicals tend to dimerize as hydrogen peroxide (equation 8), which can be further oxidized to hydroperoxil radical ($HO_2^{\bullet}$) acording to reaction (9) (Brillas and Martínez-Huitle, 2015; Malpass et al., 2017). The efficiency loss can be explained according to the acceleration of former parasitic reactions (7)–(9) that consume the provided electrons in non-oxidizing reactions, which reduces the ratio of organic events per charge circulated.

$$2\ H_2O \rightarrow O_2 + 4\ H^+ + 4\ e^- \tag{7}$$

$$2\ ^{\bullet}OH \rightarrow H_2O_2 \tag{8}$$

$$H_2O_2 + {}^{\bullet}OH \rightarrow HO_2^{\bullet} + H_2O \tag{9}$$

Even though some of the products yielded from these parasitic reactions are also reactive oxygen species (ROS) such H_2O_2 ($E^o(H_2O_2/H_2O) = 1.76$ V/SHE) or $HO_2^{\bullet}$ ($E^o(HO_2^{\bullet}/H_2O) = 1.65$ V/SHE), these species have lower oxidative power compared to $^{\bullet}OH$ radical ($E^o(^{\bullet}OH/H_2O) = 2.80$ V/SHE) (Moreira et al., 2017). Therefore, the enhanced electrogeneration of such ROS not only consumes $^{\bullet}OH$ but also diminishes the relative oxidative power of the electrochemical treatment reducing the MCE. The decrease in MCE during the electrolysis time was observed regardless of the applied *j*. This tendency can be ascribed to the formation of recalcitrant intermediates that are less susceptible to oxidation by $^{\bullet}OH$.

An interesting insight is the correlation between applied *j*, MCE and the EC (cf. Eq. 3 and 4). As shown in Figure A-2a, the energy consumption, and ultimately the expected overall cost of EO treatment, increased with the exponential decay of MCE when *j* increased. It is highly relevant to consider these parameters during scaling-up to optimize between treatment time, efficiency and cost (Ureña de Vivanco et al., 2013; Frangos et al., 2016).

The reverse-phase HPLC chromatograms exhibited characteristic peaks related to pCBA at a retention time (t_r) of 1.6 min. Figure A-1b depicts the faster abatement of pCBA attained by increasing *j*, which was completely removed after 280 min, 330 min and 360 min for 100.0, 66.6 and 33.3 mA cm^{-2}, respectively. Only 91% of pCBA was degraded by EO after 360 min at 16.6 mA cm^{-2}. The kinetic analysis demonstrated good equation fittings and estimated k_1 corresponding to pseudo-first order kinetics for pCBA removal (Figure A-1b inset). The k_1 values increased with *j* (Figure A-2b): 7.64 x 10^{-5} s^{-1} (R^2= 0.997) at 16.6 mA cm^{-2}, 9.16 x 10^{-5} s^{-1} (R^2= 0.999) at 33.3 mA cm^{-2}, 1.07 x 10^{-4} s^{-1}

(R^2= 0.999) at 66.6 mA cm^{-2} and 1.15 x 10^{-4} s^{-1} (R^2= 0.998) at 100.0 mA cm^{-2}. This result suggests a constant production of $^{\bullet}$OH radical by reaction (1) attaining a pseudo-constant concentration of oxidant on the BDD surface for each *j*. Figure A-2b highlights that k_1 does not vary linearly with applied *j*, attaining a plateau at 100 mA cm^{-2}. This plateau denotes a change of regime where the kinetics become limited by mass transfer of the pollutant towards the electrode surface rather than the applied *j*. Above certain *j*, only parasitic reactions such as (7)–(9) are enhanced, thereby diminishing the treatment efficiency and increasing the E_{EO}. In this frame, Figure A-2b shows an exponential increase of E_{EO} from 39.3 kWh m^{-3} $order^{-1}$ at 16.6 mA cm^{-2} to 331.8 kWh m^{-3} $order^{-1}$ at 100 mA cm^{-2}, which corresponds to a one order of magnitude of difference after a 6-fold increase in *j*. E_{EO} values agree with E_{EO} requirements reported previously for different anodic materials, which range from 10 kWh to 2300 kWh m^{-3} $order^{-1}$ (Malpass et al., 2008; Vahid and Khataee, 2013; Escudero et al., 2017). These results demonstrated that selecting an adequate *j* can modify the treatment time requirement to achieve complete removal. In addition, the results show the overall efficiency and relative operational cost of the treatment are competitive at low E_{EO} with other AOPs with E_{EO} above 30 kWh m^{-3} $order^{-1}$ such as UV/H_2O_2 or photocatalysis (Behnajady and Modirshahla, 2006; Ureña de Vivanco et al., 2013; Escudero et al., 2017). For our system, the optimal condition was 66.6 mA cm^{-2} because it completely eliminated pCBA and DOC with shorter operational times, higher MCE and lower E_{EO}.

Effect Of Initial Concentration On Treatment Efficiency

The initial pollutant concentration can affect water treatment technology performance, so defining the optimal treatable contaminant range for each technology is of interest. Initial concentrations from 0.3 mM to 2.4 mM of pCBA (equivalent to 25 to 200 mg L^{-1} of DOC) were treated by EO with BDD anode at 66.6 mA cm^{-2} (cf. Figure A-3a). Complete DOC removal was observed after 360 min of electrolysis for concentrations up to 100 mg L^{-1} of DOC (2.4 mM of pCBA). At higher pollutant concentrations (200 mg L^{-1} of DOC), only 88% was removed after 360 min of electrolysis. However, the MCE change depicted on the inset panel of Figure A-3a highlights an increase in MCE when raising pCBA concentration from 4.9% for 25 mg L^{-1} of DOC up to 27% for 200 mg L^{-1} of DOC. The highest efficiency observed is explained by the high concentration of organic substrates that react with the same amount of $^{\bullet}$OH radical generated at defined *j*, which increases the extent of mineralization events and minimizes the rate of parasitic reactions (7)–(9). As shown in Figure A-4a, the increse in MCE reduced exponentially the cost to mineralize a mass of DOC by EC. The efficiency increase was limited by the amount of electrogenerated $^{\bullet}$OH radical, suggesting that the associated energy consumption can be only slighlty reduced when increasing pCBA above 200 mg L^{-1} of DOC. MCE decreased with the elecrolysis time as discussed above, and higher concentrations presented a more dramatic decay (inset of Figure A-3a). This phenomenon was less significant with decreasing initial organic substrate content. This behavior suggests that producing more recalcitrant by-products at higher organic loads diminishes the overall efficiency at longer electrolysis times (El-Ghenymy et al., 2013).

Figure A-3b shows that as initial pCBA concentration increased, longer electrolytic times were needed for complete abatement: 260 min for 0.3 mM, 300 min for 0.6 mM, 330 min for 1.2 mM and 420 min for 2.4 mM. The kinetic analysis shown in the inset panel of Figure A-3b allowed calculating k_1 for each condition tested. Conversely to MCE, k_1 declined for higher pCBA loadings with values of 1.51 x 10^{-4} s^{-1} (R^2= 0.999) at 0.3 mM, 1.23 x 10^{-4} s^{-1} (R^2= 0.999) at 0.6 mM, 1.07 x 10^{-4} s^{-1} (R^2= 0.998) at 1.2 mM and 9.53 x 10^{-5} s^{-1} (R^2= 0.998) at 2.4 mM (Figure A-4b). The exponential decay of k_1 with linear increase of concentration (cf. Figure A-4b) suggests that more electrogenerated $^{\bullet}$OH radical was available to react with the smaller amount of intermediates formed, thus raising the apparent constant k_1; this agrees with the concurrent MCE increase discused previously. E_{EO} depicts a logarithmic increase when plotted versus initial pCBA concentration (Figure A-4b). The amount of $^{\bullet}$OH produced was defined by the applied j. Because $^{\bullet}$OH is a non-selective oxidant, the reaction rate with the desired pollutant is compromised when the organic load in solution increases because of the competitive consumption of oxidants by the intermediates generated. As shown in Figure A-4, there is a compromise between DOC abatement efficiency and targeted pollutant removal rate that affects the energy consumption associated to each response (EC and E_{EO}, respectively). Pollutant concentration below 1.2 mM improved the hydroxyl radical selectivity towards targeted pollutant removal, minimizing the associated E_{EO}. Conversely, organic loads greater than 100 mg L^{-1} of DOC reduced the mineralizaton EC.

Release Of By-Products

Oxidation by-products were studied under the EO optimal conditions (66.6 mA cm^{-2} and 1.2 mM of pCBA)—i.e., the conditions that ensured complete removal with minimal E_{EO} and maximum MCE response. Stable aromatic by-products that formed during EO treatment were identified by reverse-phase HPLC analysis of aliquots collected at different electrolysis times. Hydroxybenzoic acid was the first aromatic by-product released as result of pCBA dechlorination with concentrations below the quantification limit at t_r = 1.5 min. Figure A-5a shows the hydroquinone that exhibited a characteristic peak at t_r = 2.7 min. Hydroquinone was quickly released and removed, reaching maximum concentrations in solution of 0.05 mM and being completely removed after 240 min of EO treatment. The characteristic hydroquinone redox couple, benzoquinone, was below the limit of quantification at t_r = 3.2. The low accumulation of aromatic by-products in solution suggests their faster oxidation by $^{\bullet}$OH, yielding more recalcitrant by-products such as carboxylic acids of low molecular weight.

Further analysis by ion-exclusion HPLC showed well-defined peaks related to short-linear carboxylic acids. The chromatograms displayed peaks associated to malonic acid at t_r = 9.7 min, succinic acid at t_r = 11.9 min, oxalic acid at t_r = 6.3 min, acetic acid at t_r = 14.7 min and formic acid at t_r = 13.6 min. Malonic and succinic acid can be formed from the benzene aromatic moiety cleavage, and they are further oxidized to oxalic, formic and acetic acids. Malonic acid reached maximum concentrations of 0.06 mM at 180 min of electrolysis and was then slowly oxidized (see Figure A-5b). A similar trend was observed for oxalic acid, which reached higher accumulation up to 0.12 mM at 180 min. These highly recalcitrant acids are generally considered the ultimate products of EO prior to complete mineralization to CO_2 (Guinea et al., 2009; Queiroz et al., 2017).

A complete mass balance on DOC was conducted and highlighted pCBA as the main species in solution (Figure A-6). This suggests that the pCBA by-products formed near to the electrode surface were quickly mineralized and had low accumulation, maybe due to the high accumulation of $^{\bullet}$OH physisorbed on the BDD surface. The mass balance at the end of the electrolysis after complete pCBA removal indicated that the remaining

DOC was mainly oxalic acid (57.1%), malonic acid (20.8%) and unidentified recalcitrant by-products (22.1%), which can be associated to unknown carboxylic acids due to the absence of peaks in reverse-phase chromatography. The remaining carboxylic compounds at the end of the electrolysis, although being hardly oxidized by $^{\bullet}OH$, are biodegradable (Guinea et al., 2009; Queiroz et al., 2017) and considered innocuous species.

The dechlorination of pCBA during mineralization by EO releases chlorine heteroatom as inorganic ion in solution. Ionic chromatography quantified chloride ion as an inorganic by-product of EO treatment. Chloride accumulated, reaching a maximum concentration of 0.19 mM at 240 min (Figure A-5c) followed by a slight decrease to 0.16 mM at 360 min. This is only a small fraction of the theoretical expected concentration of 1.2 mM assuming complete release of chlorine atom present in 1.2 mM solution of pCBA as chloride. The decrease in Cl^- ion suggests its oxidation releases other chlorine species. Indeed, the oxidation of Cl^- can yield chlorine (Cl_2) from reaction (10). Afterwards, Cl_2 can be displaced from solution by O_2 formed via reaction (7), or hydrolyzed to hypochlorous acid (HClO) and Cl- according to reaction (11). HClO and hypochlorite anion (ClO^-) are in acid base equilibrium (Eq. 12) with pKa = 7.55 (Deborde and von Gunten, 2008).

$$2\ Cl^- \rightarrow Cl_2 + 2e^- \tag{10}$$

$$Cl_{2(aq)} + H_2O \rightarrow HClO + Cl^- + H^+ \tag{11}$$

$$HClO \leftrightharpoons ClO^- + H^+ \tag{12}$$

These species, also known as active chlorine species, contribute to the mineralization of organics as expected from their high standard reduction potentials of 1.36 V/SHE for Cl_2, 1.49 V/SHE for HClO and 0.89 V/SHE for ClO^- (Deborde and von Gunten, 2008; Pereira et al., 2015; Brillas and Martínez-Huitle, 2015). Even though active chlorine species are weaker oxidants in comparison to $^{\bullet}OH$ radical (2.80 V/SHE), they are not limited by mass transfer due to their homogeneous character in solution, which could enhance mineralization performance (Llanos et al., 2014; Fajardo et al., 2017).

In a highly oxidative media, ClO^- can be further oxidized yielding other chlorinated oxyanions such chlorite (ClO_2^-), chlorate (ClO_3^-) and perchlorate (ClO_4^-) from reactions (13)–(15). Chlorine oxyanions are undesired ionic species that have adverse effects on living organisms (van Wijk et al., 1998; Bergmann et al., 2008).

$$ClO^- + H_2O \rightarrow ClO_2^- + 2\,H^+ + 2e^- \qquad (13)$$

$$ClO_2^- + H_2O \rightarrow ClO_3^- + 2\,H^+ + 2e^- \qquad (14)$$

$$ClO_3^- + H_2O \rightarrow ClO_4^- + 2\,H^+ + 2e^- \qquad (15)$$

ClO^- and ClO_2^- were not detected in this study, whereas perchlorate peak was observed in the ionic chromatograms under limit of quantification at the beginning of the treatment. The high oxidative power of $^{\bullet}OH$ radical generated on BDD anodes can generate considerable amounts of ClO_4^- (Garcia-Segura et al., 2015b; Jasper et al., 2017); however, by the careful selection of adequate cathode materials such as platinum based electrodes (Rusanova et al., 2006), this undesired by-product can be minimized and avoided due to the electrocatalytic reduction of ClO_4^-. In this frame, the use of a platinum cathode can explain non-accumulation of perchlorate. Figure A-5c depicts the chlorate ion reaching maximum concentration of 0.068 mM at the end of the EO treatment (360 min). A chlorine mass balance determined 19% (0.23 mM) of the initial chlorine atom in pCBA remained in solution in ionic form as Cl^- and ClO_3^-. Considering that BDD anodes completely mineralize organics and avoid the formation of organochlorinated compounds (Jasper et al., 2017), we can infer that the missing chlorine in solution (81%) is lost in the form of volatile chlorine (Cl_2) displaced from oxygen side-reaction by Eq. (7).

Proposed Reaction Pathway For Para-Chlorobenzoic Acid Mineralization

Based on the identified intermediates during pCBA treatment by EO with BDD anodes under optimal E_{EO} and MCE, Figure A-7 presents the proposed reaction sequence for pCBA mineralization. The mechanism considers the organic compounds reaction with $^{\bullet}OH$ radical as the main oxidant for sake of simplicity, although direct charge transfer reactions on the electrode surface and the participation of secondary oxidant species (H_2O_2 and $HO_2^{\bullet}$) are also feasible. The degradative pathway is initiated by the hydroxylation of pCBA [1] leading preferentially to chloride anion release and *p*-hydroxybenzoic acid [2] formation . Otherwise the decarboxylation of pCBA [1] can produce *p*-chlorophenol [3] (suggested by-product). Further oxidation of p-hydroxybenzoic acid [2] and *p*-chlorophenol [3] results in the quinonic by-products hydroquinone [4] and benzoquinone [5]. Note that attack of $^{\bullet}OH$ radical on C-4 of *p*-chlorophenol [3] may result in the release of chloride anion. The cleavage of the benzenic ring leads to a mixture of low molecular weight dicarboxylic acids, malonic acid [6] and succinic acid [7], which are finally converted into oxalic acid [8], acetic acid [9] and formic acid [10]. These ultimate acids [8-10] are highly recalcitrant but can be slowly oxidized to CO_2 by $^{\bullet}OH$ electrogenerated on BDD surface.

Conclusions

The effect of operational variables on EO efficiency and energy requirements have been analyzed from figures of merit (MCE and E_{EO}). A linear increase in *j* exponentially decreased the MCE from 22.0% at 16.6 mA cm^{-2} to 5.3% at 100.0 mA cm^{-2}. The pCBA abatement by EO was limited by current at low applied *j*, whereas it was limited by mass transfer at high *j*. Therefore, increasing *j* above the regime transition unnecessarily increased E_{EO} by one order of magnitude from 39.3 kWh m^{-3} $order^{-1}$ at 16.6 mA cm^{-2} to 331.8 kWh m^{-3} $order^{-1}$ at 100.0 mA cm^{-2}.

When increasing the pollutant loading, MCE improved from 1.6% up to 13.1% during EO treatment at 66.6 mA cm^{-2}, which was associated with greater availability of organic matter that minimized parasitic reactions. Lower E_{EO} was demonstrated for lower pCBA concentrations due to the selectivity of hydroxyl radical towards targeted pollutants versus by-products competing for $^{\bullet}OH$.

A degradative pathway for pCBA degradation involving these compounds is proposed for EO. The quantification of by-products allowed conducting complete mass balances that suggested: (i) fast mineralization of by-products by $^{\bullet}OH$ led to low accumulation in solution, (ii) biodegradable carboxylic acids accounted for the remaining DOC in solution at final treatment, (iii) chlorine heteroatom of pCBA formed as volatile chlorine was displaced by oxygen evolution.

Even though EO capabilities on pollutants and DOC abatement were demonstrated, high E_{EO} values have been estimated. The treatment of a real water matrix would diminish treatment selectivity and consequently increase E_{EO}. Further development of these technologies should aim to reduce E_{EO} by at least one order of magnitude to become a cost competitive technology.

Acknowledgments

This work was partially funded by the National Science Foundation (NSF) through the Nanotechnology-Enabled Water Treatment Nanosystems Engineering Research Center (EEC-1449500). M. Lanzarini-Lopes acknowledges the Interdisciplinary Graduate Educational Research Traineeship – Solar Utilization Network fellowship funded by the NSF.

A-6. Figures

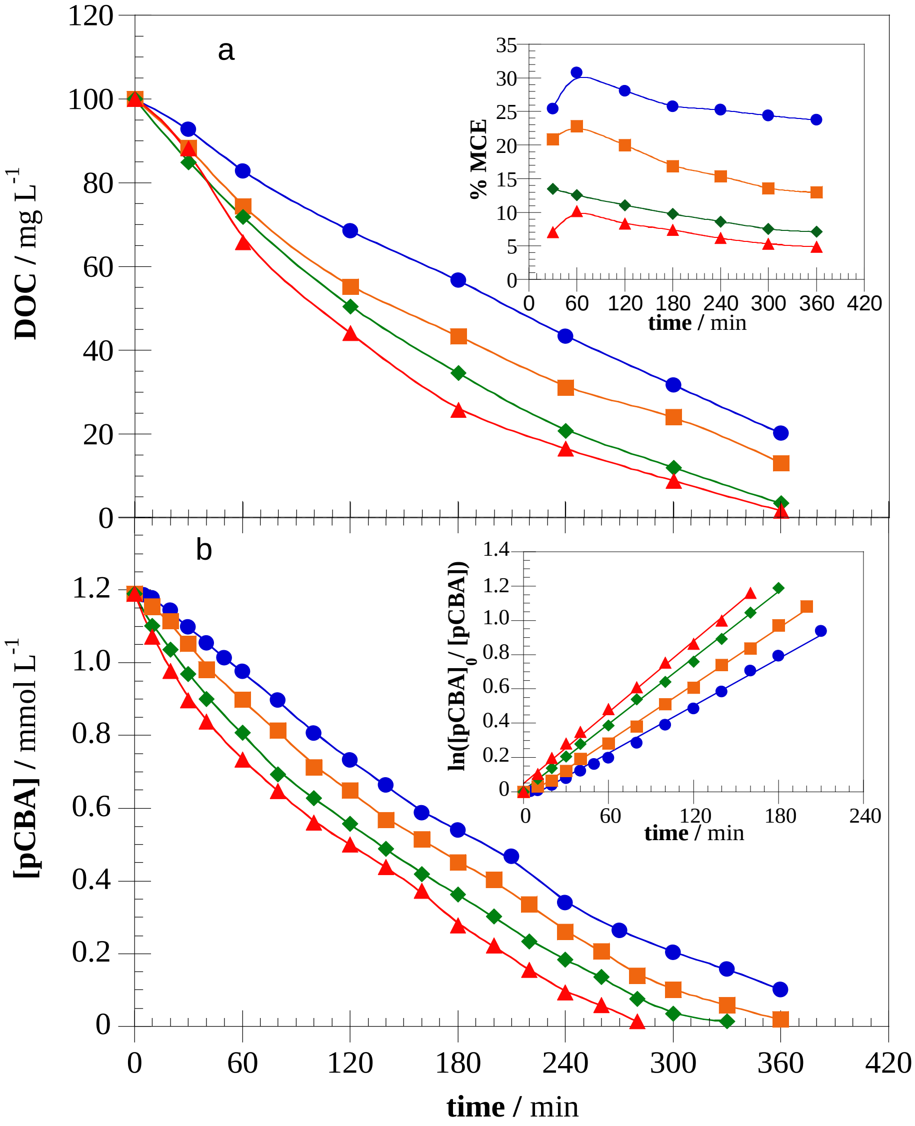

Figure A-1. Abatement of (a) DOC and (b) pCBA with electrolysis time for the electrochemical oxidation treatment with boron-doped diamond anode of 100 mL of 1.2 mM of pCBA in 0.05 M Na_2SO_4 at pH 6.0 under different applied current densities: (●)16.6 mA cm^{-2}, (🟩) 33.3 mA cm^{-2}, (◆) 66.6 mA cm^{-2} and (▲) 100.0 mA cm^{-2}. The inset panels present the corresponding (a) mineralization current efficiency estimated from eq. (3) and (b) the kinetic analysis assuming pseudo-first-order reaction kinetics

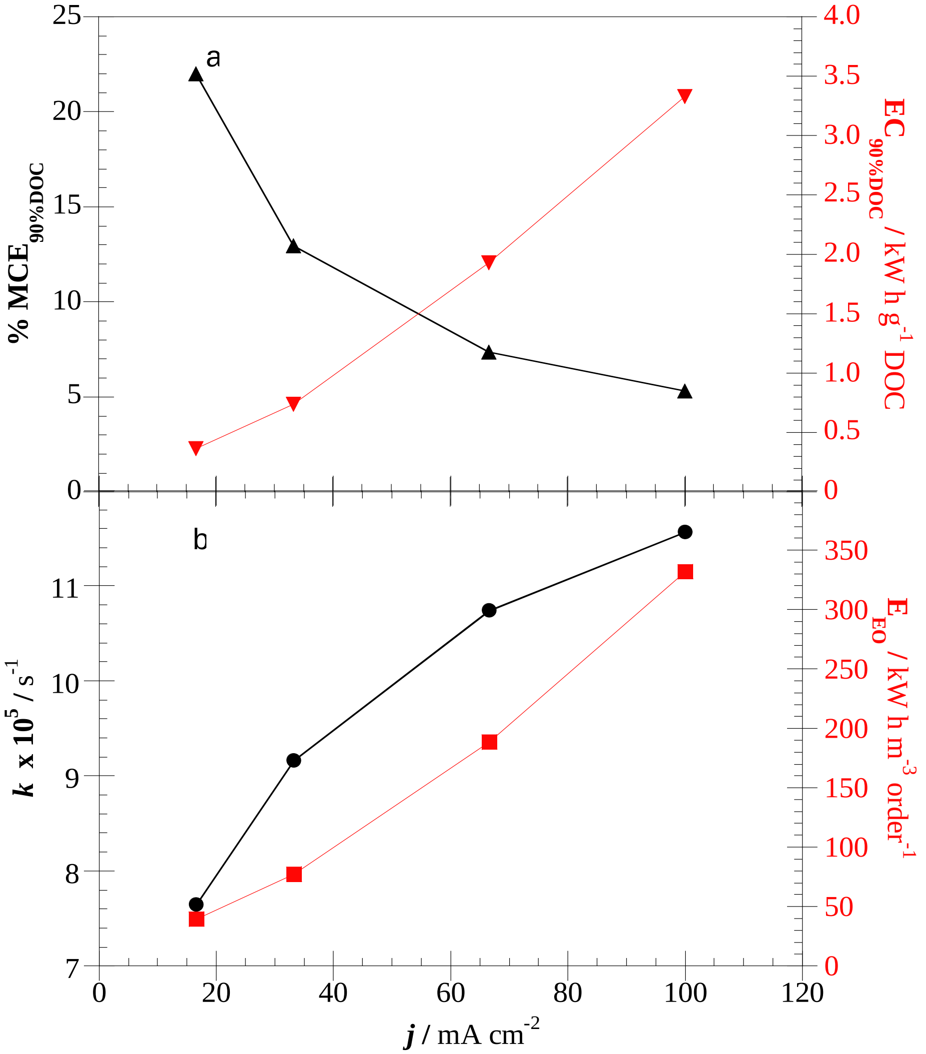

Figure A-2. (a) Influence of applied current density on (▲) mineralization current efficiency and (▼) the corresponding energy consumption after 90% of DOC abatement. (b) Variation of (●) kinetic rate constant of pCBA decay and (■) electrical energy per order with the applied current density.

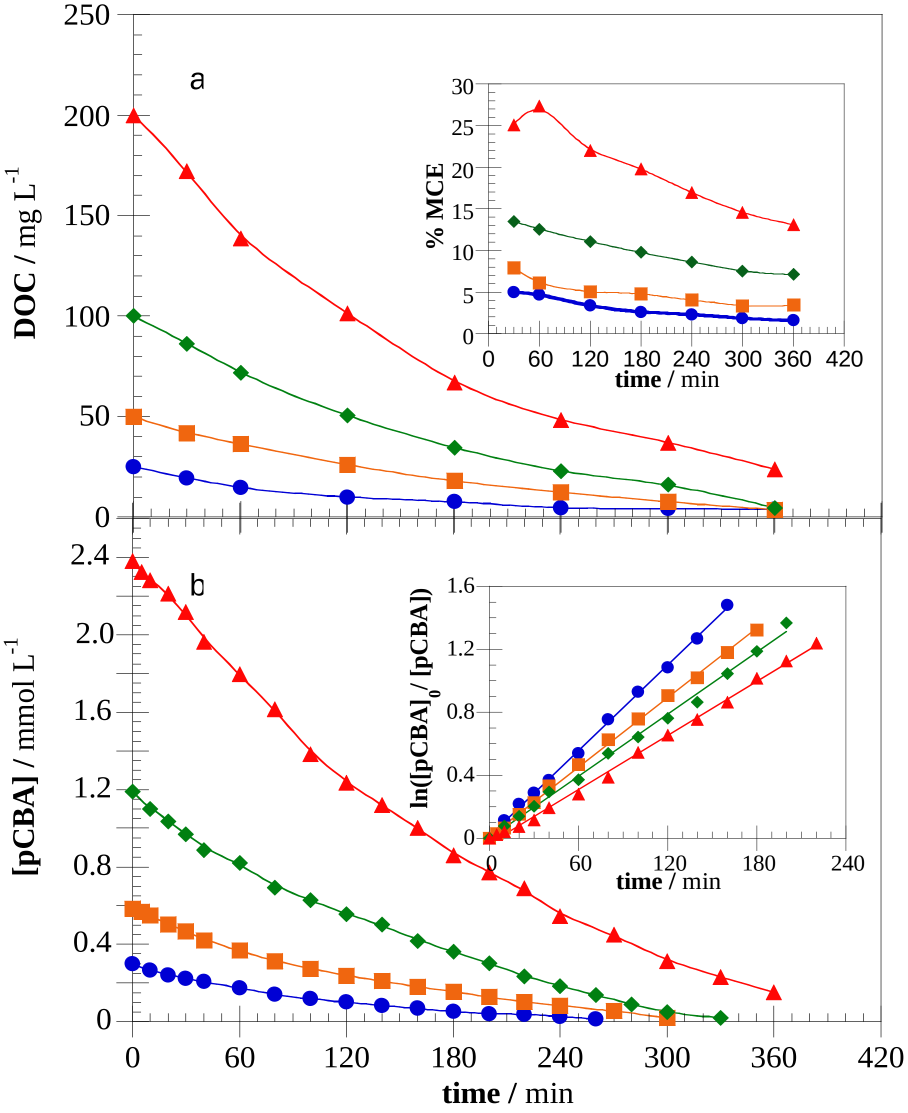

Figure A-3. Abatement of (a) DOC and (b) pCBA concentration with electrolysis time for the electrochemical oxidation treatment with boron-doped diamond anode of 100 mL of pCBA solutions in 0.05 M Na_2SO_4 at pH 6.0 and 66.6 mA cm^{-2}. Initial pCBA concentration: (●) 0.3 mM, (■) 0.6 mM, (◆) 1.2 mM, (▲) 2.4 mM. The inset panels present the corresponding (a) mineralization current efficiency estimated from eq. (3) and (b) the kinetic analysis assuming pseudo-first-order reaction kinetics.

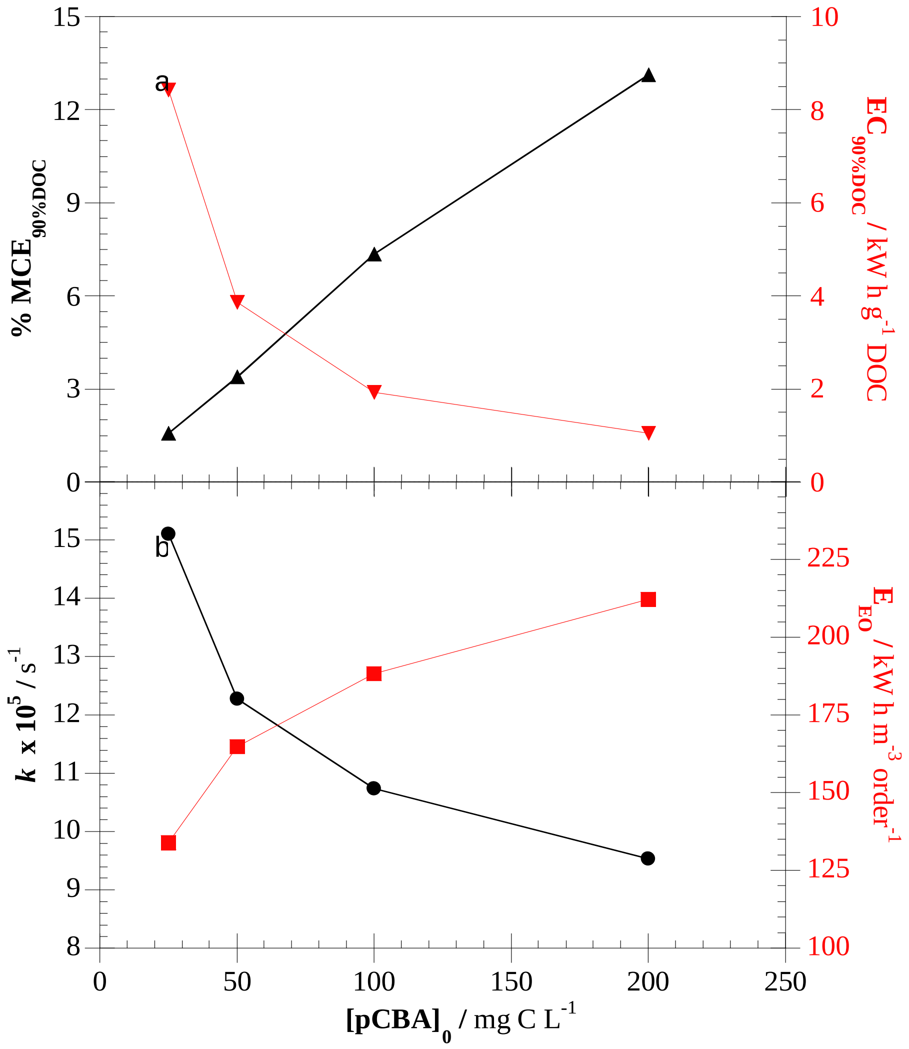

Figure A-4. (a) Influence of initial pCBA concentration on (▲) mineralization current efficiency and (▼) the corresponding energy consumption after 90% of DOC abatement. (b) Variation of (▲) kinetic rate constant of pCBA decay and (▼) electrical energy per order with the initial pollutant concentration treated.

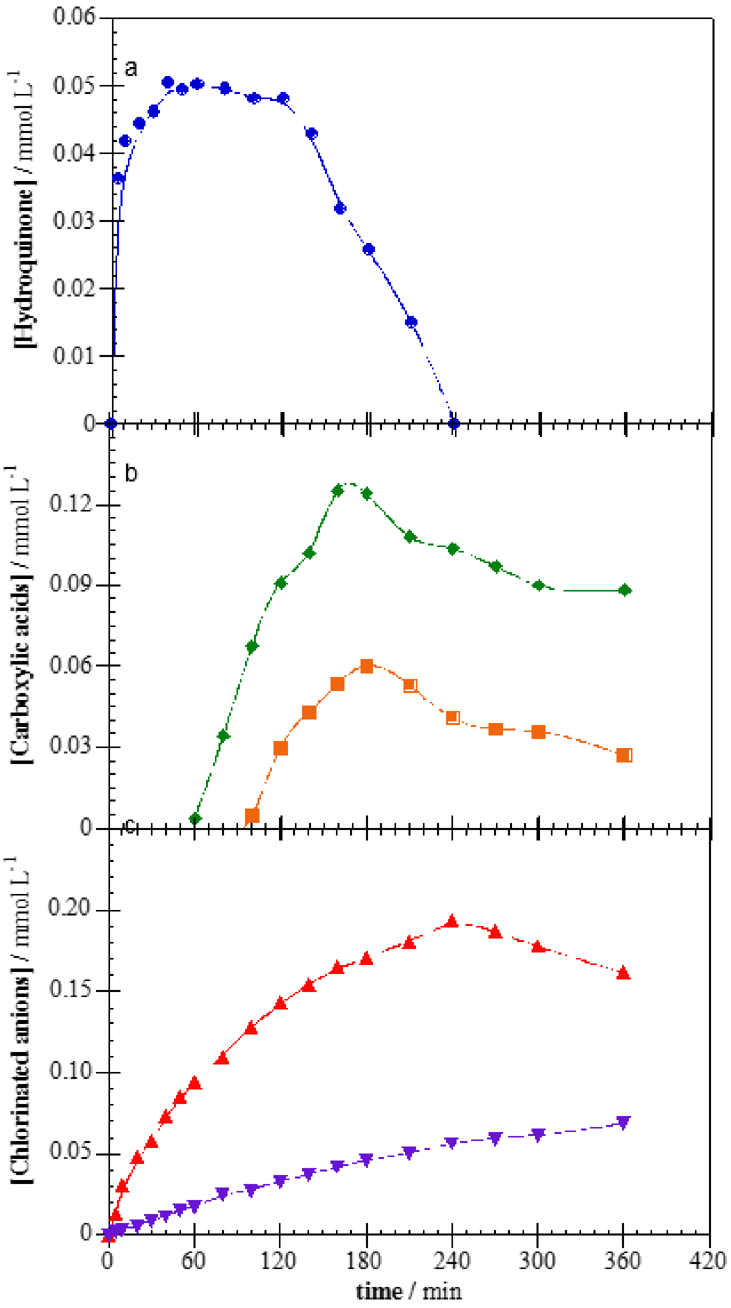

Figure A-5. By-products concentration during the EO treatment of 100 mL of 1.2 mM of pCBA at 66.6 mA cm^{-2}. (a) Aromatic by-product (●) hydroquinone. (b) Generated carboxylic acids (◆) oxalic and (■) malonic. (c) Inorganic ions (▲) chloride and (▼) chlorate.

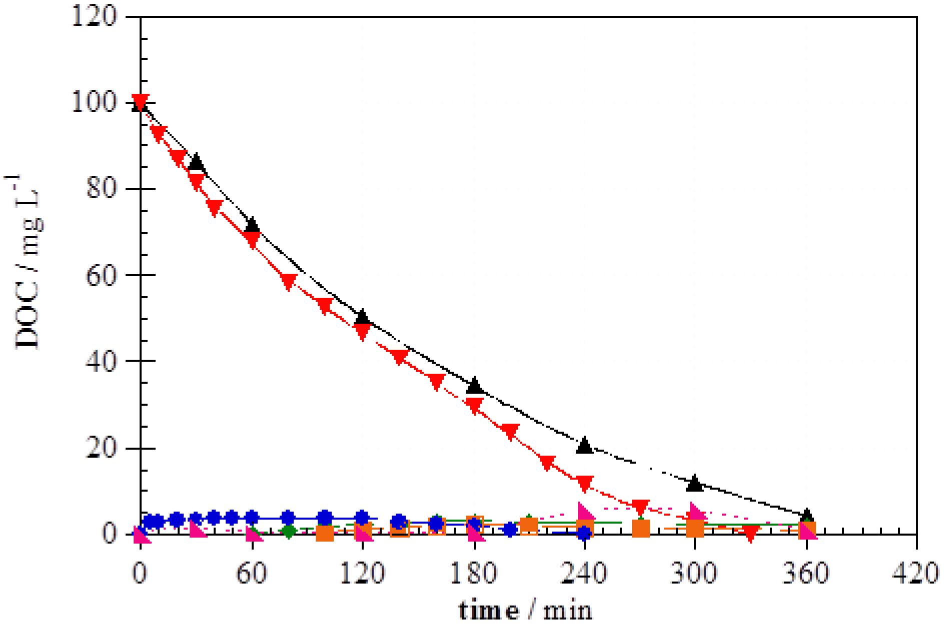

Figure A-6. Mass balance of organic species in solution released during the EO treatment of 1.2 mM pCBA solutions at 66.6 mA cm^{-2}. Organic compounds: (▼) pCBA, (●) hydroquinone, (◆) oxalic acid, (■) malonic acid, (◣) unidentified species and (▲) dissolved organic carbon.

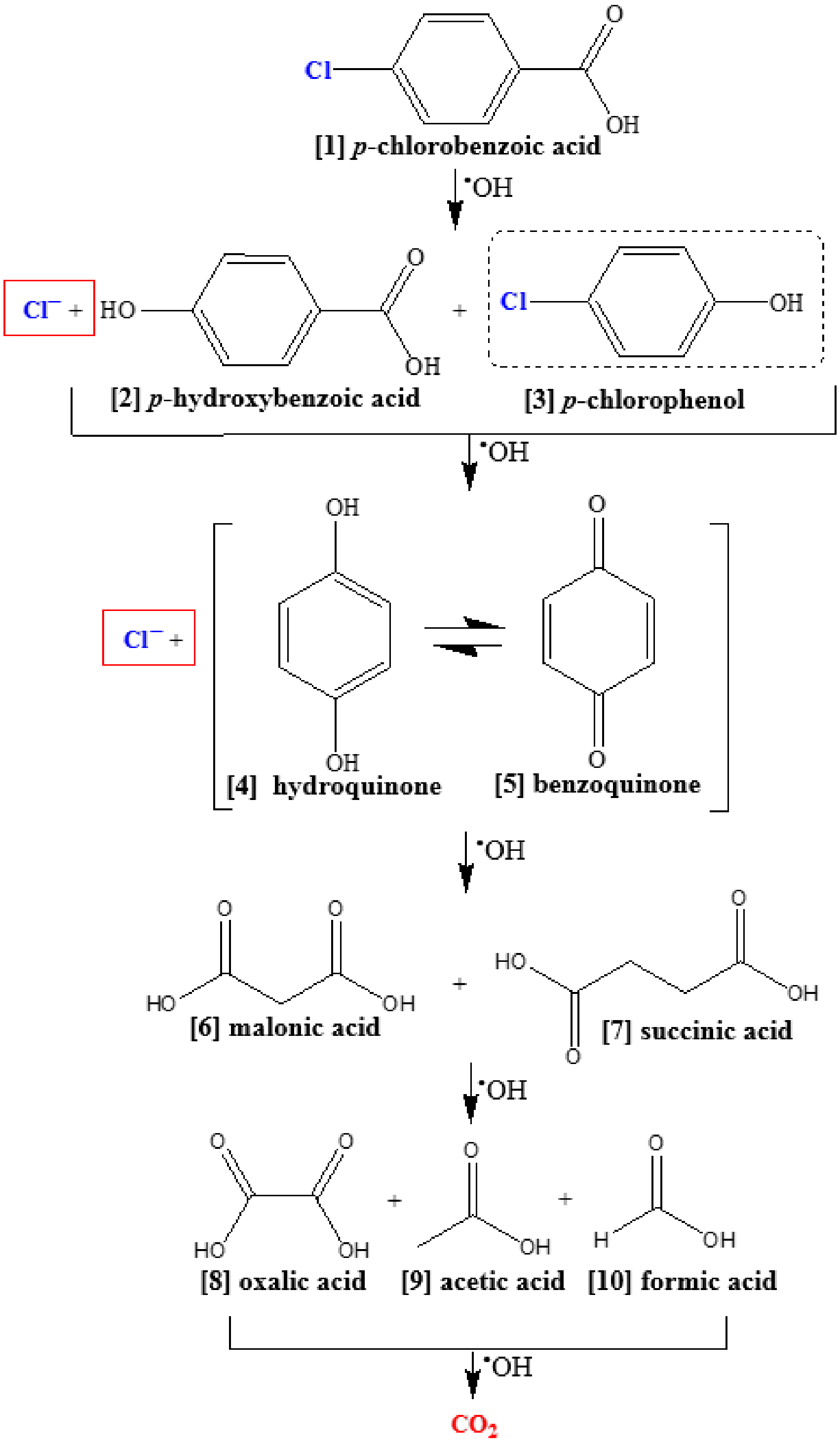

Figure A-7. Proposed reaction sequence for the mineralization of pCBA by EO with a boron-doped diamond anode.

APPENDIX B

HIGH IONIC STRENGTH TREATMENT INCREASES THE DISTRIBUTION OF NANOPARTICLE DISTANCE TO A WAVEGUIDE

Introduction

The ability to make glow sticks out of light guides is gaining interest for applications in aesthetics, medicine, and environmental remediation (Klubben et al., 2016; Lui et al., 2016; Xu et al., 2008).Various methods are reported to obtain side emission (glow) from an optical fibers that focus on adding extrinsic scattering mechanisms through the fiber. These include (i) micro bending of the fiber axis, (ii) fabricating or manufacturing asymmetries in the fibers core (Arie et al., 1986; Rawson, 1974; Rawson, 1972), (iii) applying cladding material with higher refractive index than the core (Rawson, 1972; Spigulis et al., 1997), and (iv) adding scattering centers to the cladding material (Biyarin et al., 2017; Xu et al., 2008). Until recently these SEOFs could only side emit visible and UV-A light (O'Neal Tugaoen et al., 2018). By attaching silica nanoparticles on a silica core with a UV transparent polymer, the first UV-C SEOF was fabricated. In this process, it was discovered that treating the nanoparticle enabled optical fiber with a solution of high ionic strength significantly (>6 X) increased the scattering flux (I_s) of UV-C radiation (Lanzarini-Lopes et al., 2019). The mechanism of increased scattering can be explained by combining (1) the electric double layer (EDL) theory with (2) understanding of the evanescent wave.

When a charged solid surface is submersed in an electrolyte solution, the ions in the electrolyte rearrange forming an EDL. The ions that are in immediate contact with the surface are called the stern layer. Matthew A. Brown et al. illustrated that increasing the ionic strength of solution from 0.0 – 0.12 M L-1 decreases the thickness of the stern layer by ~1 nm due to the increase in osmotic pressure of the solution (Brown et al., 2016). Here the same phenomena is occurring with aminated silica spheres, because they are electrostatically attached, the decrease in stern layer is decreasing the distance between the particle and the waveguide. Kooij et al. illustrated that by increasing the ionic strength of a solution by 4.7 mM, the separation distance between gold nanoparticles deposited on silica decreased by 7 nm, and the particle density increases by >2 X (Kooij et al., 2002).

The effect of scattering due to separation distance of a particle from the waveguide has been demonstrated both experimentally and theoretically (Chew et al., 2008; Prieve & Walz, 2009). During internal reflection through waveguide, a portion of the wave that hits the boundary, called the evanescence wave, exits the waveguide before returning to the core. This is because electromagnetic fields cannot be discontinued at a boundary. The intensity of the evanescent wave is exponentially higher closer to the optical fiber core. Chew et al. explain that the scattering intensity from a scattering center on a waveguide follow the same exponential decay as the evanescent wave (Chew et al., 2008) such that:

$$I_h = I_0 \exp\left(-2k_2\beta h\right) \tag{8.1}$$

Where $I_0$the intensity of scattering at the closest proximity between the scattering center and the waveguide, $k_2\beta$ are properties of the material and angle of incidence, h is the distance between the scattering center and the waveguide and I_h is the intensity of scattering at that distance. Therefore, a decrease in h would result in an exponential increase in the observed scattering.

The objective of this chapter is to understand if there is a decrease in distance between the silica spheres and optical fiber core in the ionic strength treated UV-C SEOF. This knowledge allows us to better predict, design and manage light side emission from waveguides used in light delivery.

Sample Preparation

Quartz substrates (Ted Pella Inc, 26012) where prepared similar to the SEOF. The substrates where cut with a ceramic blade in to 15 X 15 cm squares and sonicated in acetone (99.5%) for 10 min. The clean quartz was then dipped in a solution of 400 nm aminated silica spheres (nanoComposix, San Diego, Ca, 10 mg/L, SIANd-25M) suspended in ethanol for 10 seconds to obtain an even coat. Half of the samples (treated) where dipped in 0.2 M solution of Na_2SO_4 (Sigma-Aldrich, 244511) (ionic strength = 0.45 M) for 10 seconds. The samples where airdried vertically in between each step. A total of 4 samples were prepared (2 treated and 2 untreated).

Height measurements by atomic force microscopy

All height measurements where performed at ambient conditions with the SPM Bruke Multimode atomic force microscope (AFM). The tapping/non-contact mode was used with a 0.01-0.025 Ohm -cm antimony (n) doped Si cantilever and resonance frequencies of 320 kHz and spring constant of 42 N/m (Bruker, NCHV-A). In order to measure the height between the top of the particle and substrate, only dispersed particle images where used. The topographical images of dispersed silica nanoparticles obtained by atomic force microscopy are illustrated in Figure B-1.

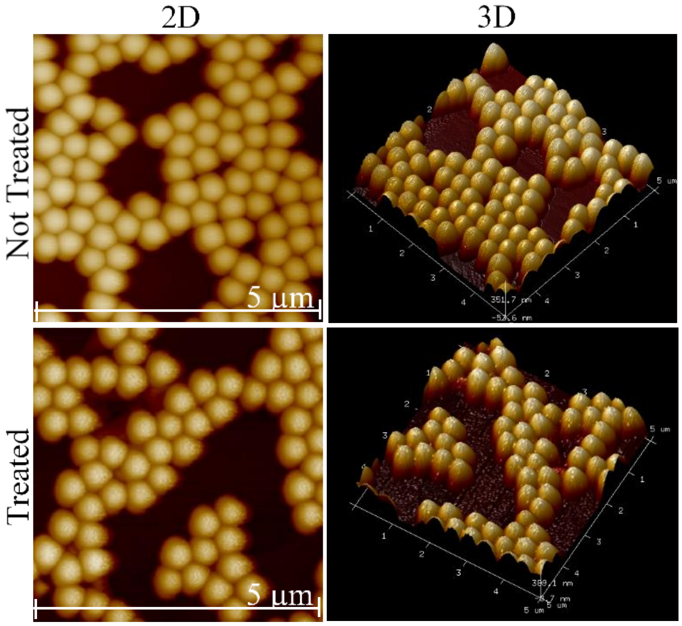

Figure B-1. Atomic Force Microscopy for both treated and not treated samples, represented in 2D and 3D.

These images where analyzed by using Bruker NanoScope Analysis software. The height of each particle in the image was measured by section analysis which indicates the topography of a straight line. Two sections where drawn intersecting at the particles highest point as verified by a < 2 nm difference in *h* in each section.

Increased variation of nanoparticle heigh with ionic strengh treatment.

In this study the relative proximity between nanoparticle and substrate is indicated from measured height difference by atomic force microscopy. The diameter of the nanoparticle is 400 nm therefore, any additional height should be due to separation between nanoparticle and substrate or nanoparticle and cantilever.

Two substrates where prepared for each analysis. Multiple (2-3) images where taken and the height of all edge nanoparticle in each figure was measured until fifty measurements where obtained per substrate (100 per treatment type). Both the raw and standardized distributions are used to analyze the significance of these results.

A histogram of both treated and untreated height measurements is illustrated in Figure 2. The means and ranges of each data set are depicted in Figure 2 inset. The means of the untreated and treated nanoparticles are equivalent at 456 (± 0.01%) nm. However, the distribution of heights is much greater after treatment with ionic strength. The height of the untreated samples are between 425 nm and 486 nm (SD = 14), while the measured height of the treated nanoparticles are within 411 nm to 509 nm (SD = 27). The graph indicates that there is an increase in variation of particle heights after treatment along with the occurrence of particles that are within 411 nm distance to the substrate.

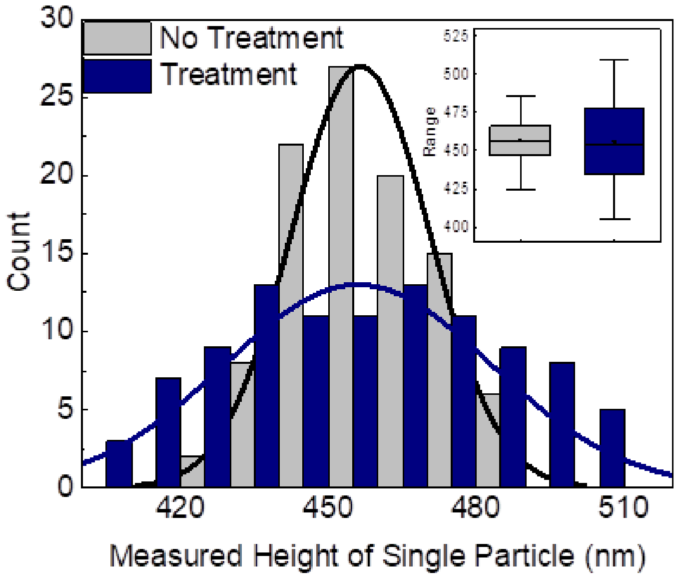

Figure B-2. Histogram of treated (blue) and untreated (grey) measured height of silica nanoparticles. Inset illustrates the mean and range of the data obtained for each condition.

The standardization of each histogram was used to analyze the standard deviation (SD) of a specific particle height in comparison to its bulk (see S.I.). Both samples contained particle heights <430 nm. However, particle heights below 430 are > 2 SD away from its mean in the untreated sample, and < 1 SD away from its mean for the treated samples respectively. These results indicate that there is >68% and < 5% that the measured height of the particle will be <430 nm for the treated and untreated samples respectively. As previously explained, the measured height of the particle corresponds to the proximity of the particle to its substrate. Thus, we conclude that treating the nano-enabled surface with a solution of 0.2 M sodium sulfate increased the occurrence of particles that are closer to the substrate.

Figure 3 conceptually illustrates the arrangement of the nanoparticles on the silica surface. Before treatment there is a higher frequency of nanoparticles within the mean distance from the substrate. After treatment, the nanoparticles are re-arranged so that some particles are farther away from the surface and others are closer. The presence of closer particles contributes to the increased scattering witnessed in chapter 5.

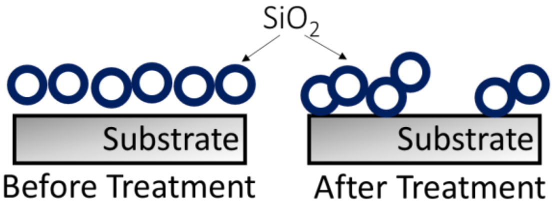

Figure B-3. Conceptual illustration of nanoparticle arrangement before (left) and after (right) ionic strength treatment.

Limitations and Future Work

These results cannot be used to model scattering coefficient of a waveguide. The height measured are not exact distances between the silica spheres and substrate, rather a relative distribution analysis. There are errors and artifacts introduce through sample preparation, instrumentation that can add artifactual height to the samples. Small variations (nm) can significantly influence the theoretical scattering results. Additionally, electric double layer theory explains that aggregation of nanoparticles are significantly increased with increased ionic strength of the environment. The nanoparticles distances between each other will reduce similarly to the distance between nanoparticle and substrate. This results in high density areas followed by low density nanoparticle areas where nanoparticles previously existed. Future work should study the difference in both particle aggregation and roughness of a surface as a result of high ionic strength.

Supplemental information

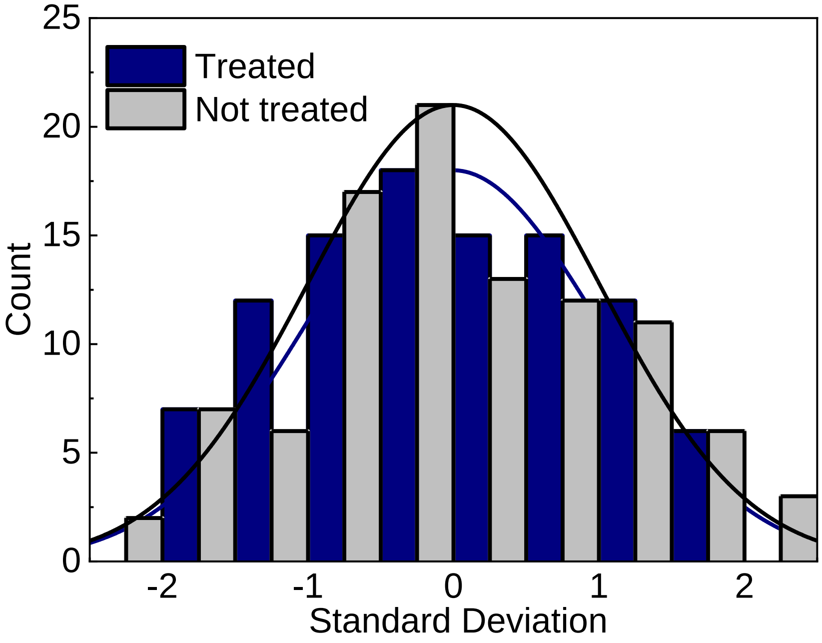

S.I. Figure. 1. Standardized histogram of height distribution of the silica nanoparticle covered substrate not treated (grey bars) and treated (blue bars) with high ionic strength solution.